UNIVERSITY OF OKLAHOMA

GRADUATE COLLEGE

PROCESS SEDIMENTOLOGY OF THE GUADALUPIAN RADER LIMESTONE,

DELAWARE BASIN

A THESIS

SUBMITTED TO THE GRADUATE FACULTY

in partial fulfillment of the requirements for the

Degree of

MASTER OF SCIENCE

By

JOHN SPENCE HORNBUCKLE III
Norman, Oklahoma
2017

PROCESS SEDIMENTOLOGY OF THE GUADALUPIAN RADER LIMESTONE,
DELAWARE BASIN

A THESIS APPROVED FOR THE
CONOCOPHILLIPS SCHOOL OF GEOLOGY AND GEOPHYSICS

BY

_____

Dr. John D. Pigott, Chair

_____

Dr. Roger M. Slatt

_____

Dr. Kulwadee Pigott

This thesis is dedicated to the memory of my father. Without his love and support none of this would be possible.

Acknowledgements

Table of Contents

List of Tables

List of Figures

Abstract

An integrated LiDAR, XRF, Spectral Gamma Ray, and outcrop investigation was performed on the upper Guadalupian Rader Formation in the Delaware Basin of West Texas. The Rader Formation, is an upper slope carbonate submarine fan deposit that is divided into three units: the lower, middle and upper Rader intervals. The lower and upper Rader intervals are characterized by thin to thick, ungraded and graded skeletal and non-skeletal allochthonous deposits interpreted to be highstand carbonate apron deposits. These intervals are interpreted to have been deposited by grain flows and high density turbidite flows. The middle Rader unit has an erosive base and consists of ungraded matrix supported mega conglomerates and megabreccias as well as intervals of clast supported megabreccias representing a lowstand period which resulted in a catastrophic platform failure due to increasing stress of platform sediments as water level fell. The mega conglomerate and mega breccia of the middle Rader were deposited as debris flows. Lack of oiids, pisolites and fenestral fabrics within the Rader Formation indicate that more distant restricted back reef environments were not affected by the catastrophic platform failure, however, submarine cement coated grains and fusulinids observed in the middle Rader deposits indicate that the reef crest is the most proximal environment affected by the catastrophic slope failure. Of particular consequence is the presence of hummocky cross stratification observed within the Bull Head Turbidite which directly overlies the mega conglomerate deposits. The hummocky cross stratification is interpreted to be evidence of a tsunamiite generated by massive subaqueous debris flows caused by the platform failure responsible for the deposition of the mega conglomerate and mega breccia deposits.

Chapter 1: Introduction

Though the Permian Basin, made up of the Delaware and Midland sub-basins (Figure 1) has been studied for nearly 130 years, there is still much to be learned about what controls the depositional and stratigraphic development of the constituent rock units in the Delaware Basin (Lew et al., 2013). The Delaware Basin is home to world class outcrop exposures, and outcrops expose the most complete record of Permian deposits. These hold the key to unlocking the process sedimentology of the Rader Formation. The Rader is one of five carbonate tongues hosted in the Bell Canyon Sandstone (Figure 2). The Rader is most commonly observed along a road cut along US HWY 62 where large carbonate boulders are rafted in a fine sandstone matrix.
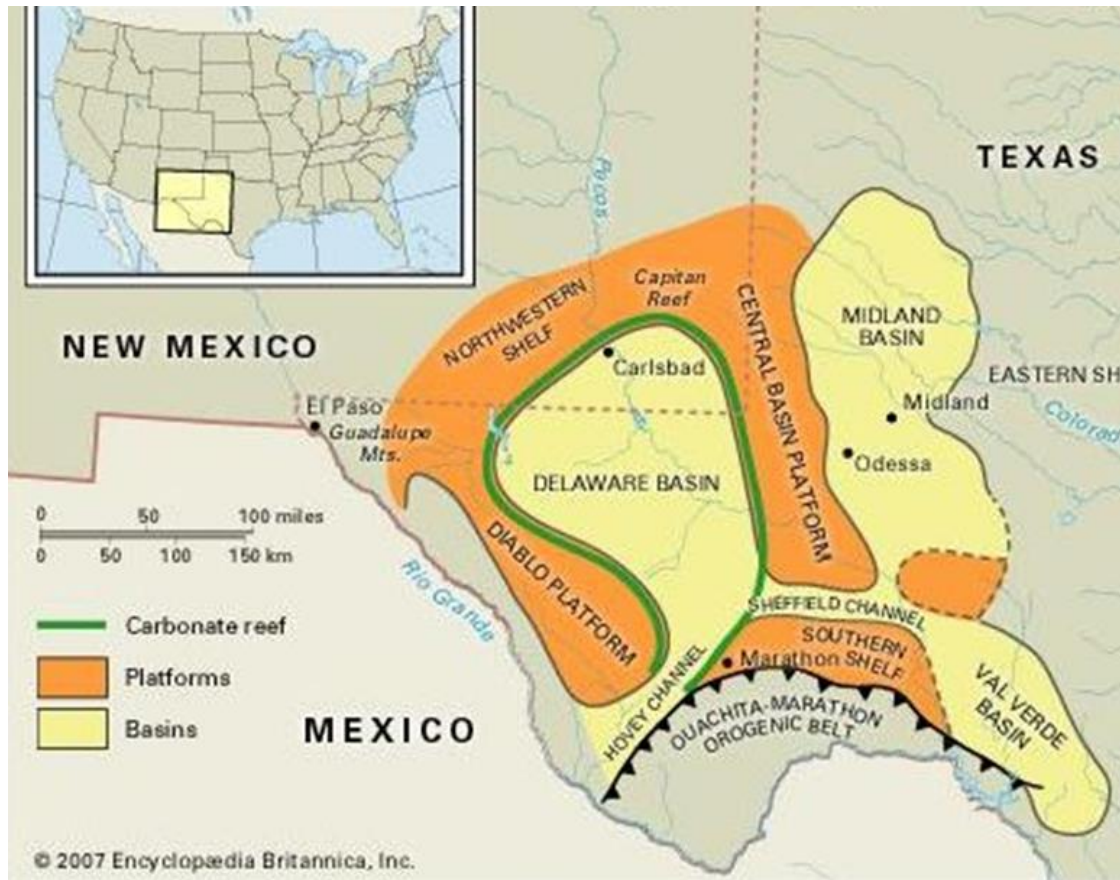
Figure 1: Simplified Map of Geologic Provinces within the greater Permian Basin. Modified from Murchinson Oil & Gas, Inc. (2014).

1.1 Problem Statement

This study attempts to relate outcrop observations of the Rader Formation with LiDAR data, XRF data, spectral gamma ray data and thin section analysis to a process interpretation of the middle Guadalupian catastrophic event in the northwestern shelf margin of the Delaware Basin. Limited published work on the Rader presents a surprising paucity of information on a commonly viewed deposit. The most extensive study was conducted in a master's thesis by Lawson (1989), who relied exclusively on classical field methods and thin section analysis. The present study presents alternative interpretations and new insights into previously unrecognized sedimentation processes.

1.2 Previous Work

P.B. King was one of the first geologists to fully map and describe the Permian age rocks of the Permian Basin in great detail. He points out the challenges in subdividing the Permian strata into satisfactory and useful units noting that the obvious units in any local area are lithologic, but such units change laterally (King, 1942). He goes on to elaborate that a large number of lithologic names have been used to subdivide the West Texas Permian, however, such practices are a hindrance rather than a help in expressing broader relations and correlating beds in different depositional environments (King, 1942).   In response, King went on to subdivide the basin into chronologic units based on the existence of certain fossils, unconformities, and changes in sedimentation (Figure 2). From this effort broad subdivisions of chronologic significance evolved in 1939, and from oldest to youngest are: Wolfcamp, Leonard, Guadalupe, and Ochoa series (King, 1942). However, aside from the large series, smaller scale formations which make up the Wolfcamp, Leonard, Guadalupe, and Ochoa series are to this day based on lithostratigraphic subdivisions leaving chronologic ambiguities between formations observed on the shelf, shelf margin, and basin for most of the Permian Basin strata.
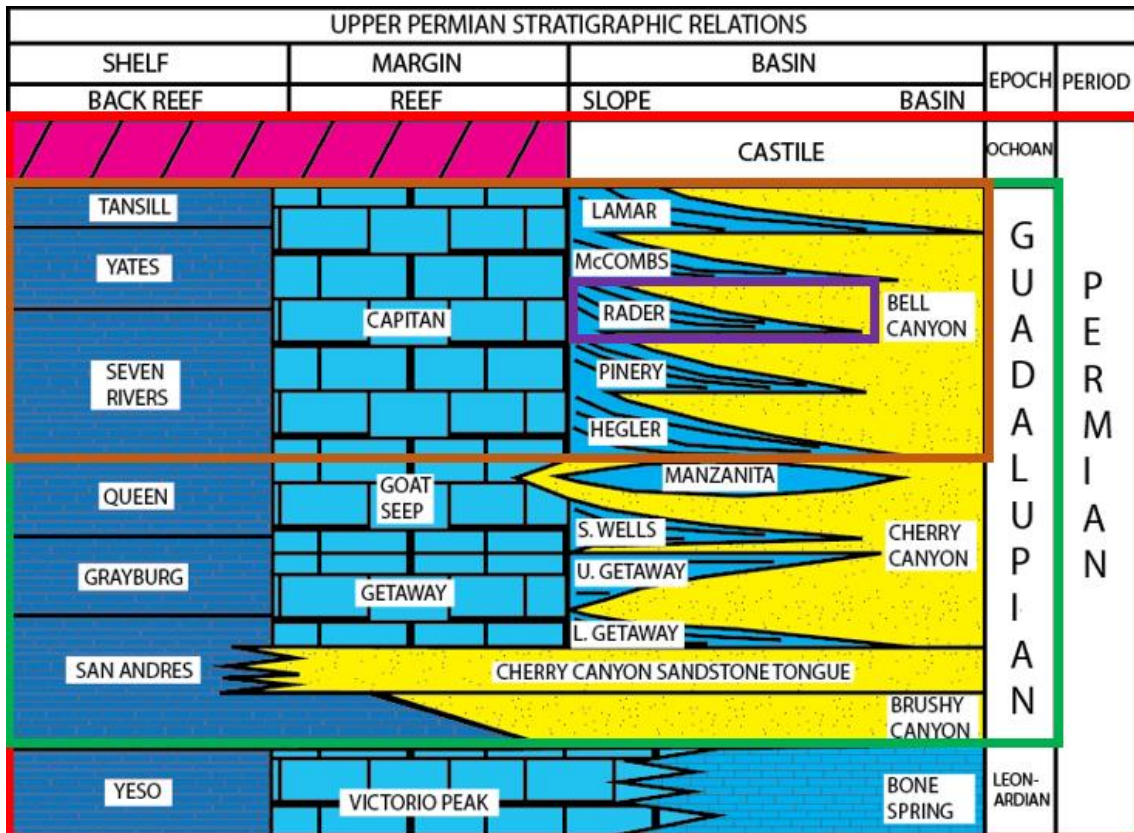
Figure 2: Detailed Upper Permian rock-stratigraphic relations of the Delaware Mountain Group. The stratigraphy is divided out into shelf, shelf margin (margin), and basin facies. Across the facie divisions, coarse time equivalent correlations of individual facie lithostratigraphy is observed. Modified from King, 1948.

Though not directly focusing on the Rader member of the Bell Canyon Formation, Osleger and Tinker (1999) conducted a high resolution sequence stratigraphic study of back reef facies of the Capitan Reef. The current study combined two independent studies previously conducted by Tinker (1998) and Osleger (1998). Tinker (1998) developed a high frequency stratigraphic framework for the Seven Rivers and Yates formations in McKittrick Canyon, while Olseger (1998) identified four high frequency sequences in the Yates formation observed in Slaughter Canyon. Both Tinker and Osleger observed a correlation between the sequence-stratigraphic frameworks in McKittrick and Slaughter Canyons, and correlated these cycles from the

4

shelf into the basin. They propose a time equivalent correlation between the Y3 (3rd Yates cycle observed) shelf member and Y4 (4th Yates cycle observed) shelf member and the lower Rader Limestone and upper Rader Limestone respectively.

Adding to the work of Tinker and Osleger, Nicklen (2011) used teprochonologic dating techniques to provide absolute ages to the Rader Formation and Yates Formation. Bentonite samples taken from within the Rader Formation was the focus of U-Pb ID-TIMS zircon dating (Nicklen, 2011). Nicklen (2011) confirms the correlation between the Rader Formation and Yates Formation put forth by Osleger and Tinker (1999). Nicklen (2011) goes further to date the Rader Limestone at 262.5 Ma. According to this date, the Rader Formation was deposited during a time of falling global sea level/lowstand period (Figure 3)
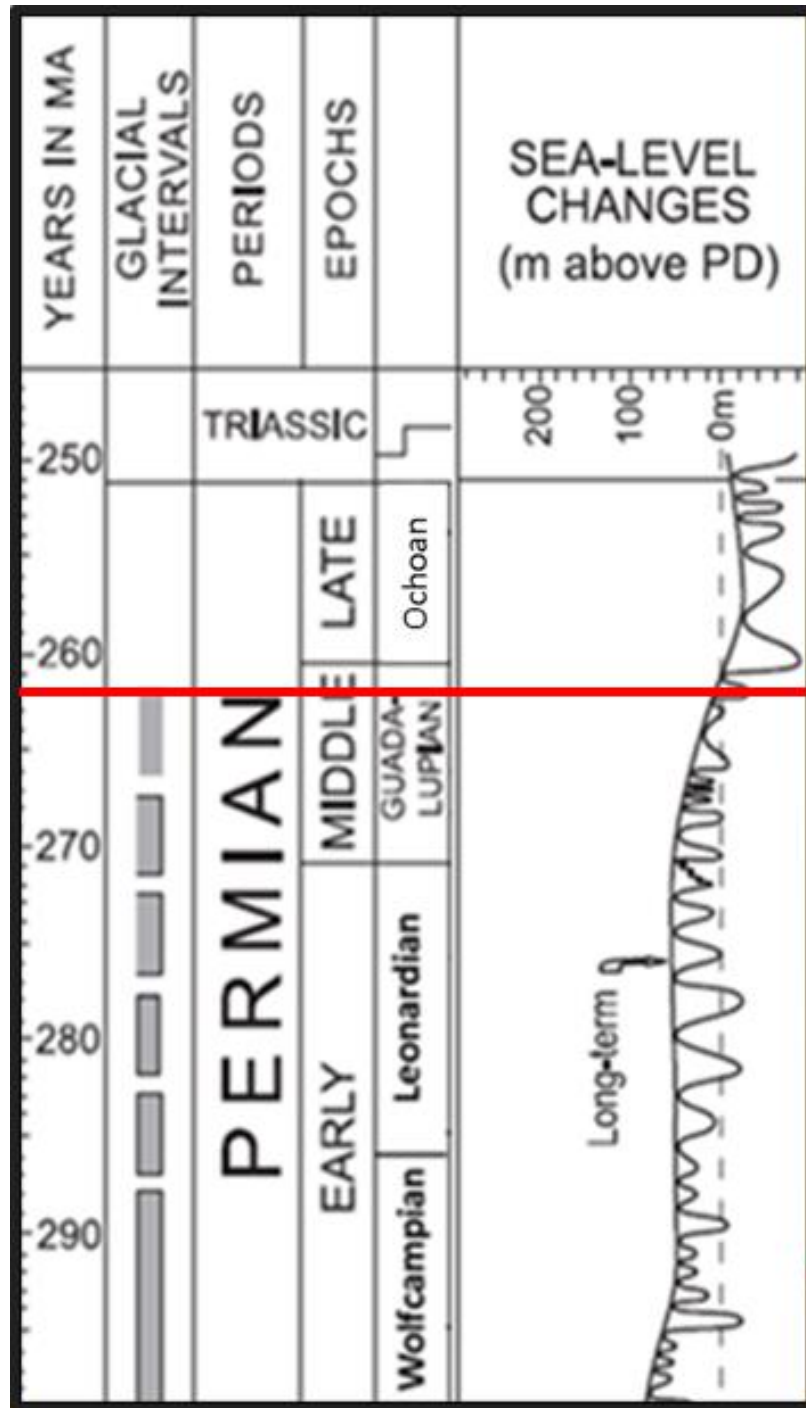
Figure 3: Global sea level curve during the Permian. Highlighted with the horizontal red line is the age of Rader deposition according to U-Pb ID-TIMS zircon dating performed in Nicklen (2011). Sea level curve modified from Haq and Schutter (2008).

Despite being a prominent limestone wedge in the petroliferous Bell Canyon Formation, little work has been done on the Rader Formation. Outside of the classical works of King (1942), Newell et al. (1953), and Rigby (1958), little has been published on the Rader Limestone despite being frequently observed in a road cut along US HWY 62 just south of the entrance to McKittrick Canyon.

In his work, King (1942) briefly describes the Rader formation as a 100 feet thick limestone unit, made up of massive, light gray limestone, very similar to the Capitan Limestone. King (1942) also noted sparse layers of thinner, darker limestone. Away from Rader Ridge, King (1942) noted that Rader Limestone thins to roughly 15 ft, massive beds disappear, and thinner, darker beds predominate.

Newell et al., (1953) described the Rader Limestone as impressive as any submarine slides known from the stratigraphic record. He went on to describe its composition as mainly ungraded and unsorted sub angular fragments of limestone the size of cobbles and small boulders, however, he noted that fragments range from a fraction of an inch across to great rafted blocks, observing one rafted block 14 feet in its greatest dimension (Newell et al., 1953). He interpreted the limestone to be sourced from the Capitan Reef front, and observed that the debris was held in a matrix of fine-grained limestone containing fusulinids (Newell et al., 1953).

Rigby (1958) described the Rader Formation along with other examples of sub-aqueous deposits of the Permian Basin. He acknowledged a syn-depositional relationship between a mega breccia, deposited in more proximal locations on Rader Ridge, with a mega conglomerate, deposited in more distal locations, commonly observed along US HWY 62 south of McKittrick Canyon. Rigby (1958) first suggested

that the Rader Formation was deposited during a period of instability in the Capitan Reef front, as evidenced by the catastrophic Rader deposits. However, he interpreted the Rader Formation to be a slump deposit (Rigby, 1958), an interpretation not shared in this study.

The Rader Formation was also studied by Lawson, (1989) in her masters thesis. She described in great detail the lithology of the formation as well as sedimentary structures. She reported that clast lithologies are mixed skeletal and non-skeletal lime grainstones. Further, she interpreted the most shelf ward contributions to the allochthonous debris is from the outer shelf. She stated that the Rader Formation exhibits features which suggest deposition from various types of mass movement such as debris flows, turbidity currents, and possibly density-modified grain flows. Lawson (1989) concurred with Rigby's earlier work that the Rader Limestone was deposited during a time of shelf instability. Nevertheless, her work does little to identify mechanisms responsible for the deposition of the Rader Limestone.

In 2006, Nestell et al. conducted a limited biostratigraphic study of the Rader Formation. The research is limited not in quality of work, but in scope as samples were only collected from the road cut along US HWY 62. In the publication, the authors state that the study is intended as a basis for establishing the distribution of the bio-stratigraphically most useful microfossils.

1.3 Study Location

The research conducted in this study takes place in the Delaware basin, which is the western sub basin of the greater Permian basin. The Delaware Basin is located in west Texas and south eastern New Mexico. It is an asymmetric basin containing 25,000

ft (7,600 m) of mostly Paleozoic sedimentary rocks (Payne, 1976) and covers an area of approximately 33,500 square kilometers (Hill, 1996). Of the 25,000 ft of Paleozoic rocks, roughly 12,000 ft are carbonate and siliciclastic rocks of Permian age (King, 1948). The basin is bound by the Diablo Platform to the west, the Northwestern Platform to the North, the Marathon-Ouachita Fold Belt to the South, and is separated from the Midland Basin by the Central Basin Platform to the East, Figure 1.

The present study focuses on four main areas of Rader outcrops as seen in Figure 4. The first outcrop represents the most proximal location in this study. It characterizes the most prominent of the mesas constituting Rader Ridge, which is located on the northeastern edge of the Guadalupe National Park. This outcrop is measured in two sections and are referred to as "Rader Ridge Proximal" and "Rader Ridge Distal" for the entirety of the study. The Rader outcrop observed here is the largest and most complete outcrop, as it is the only outcrop containing all units of the Rader Formation.

The second outcrop examined in this study is located on Ligon Ranch on a more distal and less prominent portion of Rader Ridge. It has been previously observed in studies (Payne, 1976), and was designated as the "Reverse Waterfall" based upon its unique geometry. The same terminology is utilized, as this outcrop is referred to as the "Reverse Waterfall" throughout this study.

The third outcrop is an exceptional creek bed located approximately 0.25 miles to the north of the Road Cut outcrop described below. The Creek Bed outcrop shows extraordinary bedding features that are not seen at the Road Cut outcrop. The Creek Bed outcrop is not observed regularly and is only described in one other study (Lawson,

9

1989) because it is located on private property. This outcrop is referred to as the "Creek Bed" for the remainder of this report.

The fourth and most easily accessible/well known is the Rader outcrop along U.S. Highway 62/180 just southwest of the entrance to McKittrick Canyon in the Guadalupe Mountains. The outcrop along HWY 62 is the most commonly observed Rader outcrop as it is a popular stop on most geology field trips to the area. The outcrop exhibits large carbonate boulders that are evidence of a catastrophic debris flow and subsequent carbonate flows that the Rader is famous for. Throughout the remainder of this thesis, this outcrop is referred to as the "Road Cut". The Road Cut and Creek Bed outcrops are the most basinward outcrops studied in this investigation and will be shown to represent medial slope margin deposits.
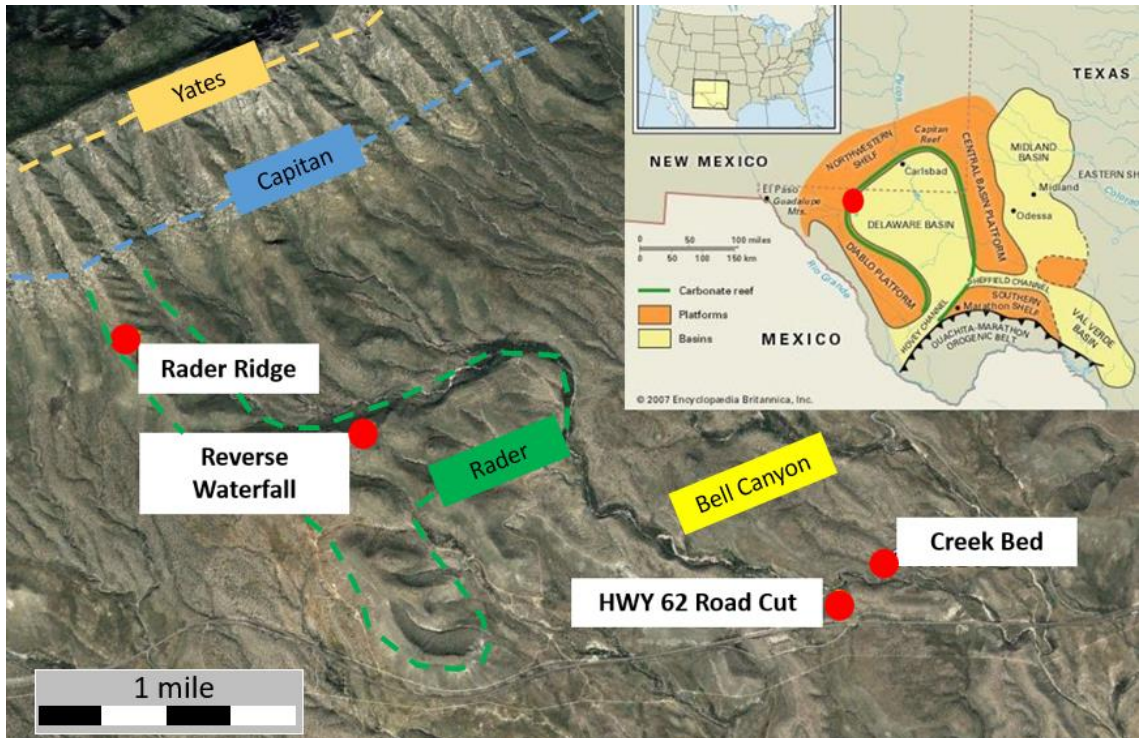
Figure 4: Location map of outcrops used in study. Approximate geologic units outlined in dashed lines. Image taken from Google Earth. Basin map included for reference. Basin map Modified from Murchinson Oil & Gas, Inc. (2014).

Chapter 2: Geologic Setting

2.1 Stratigraphy

A generalized stratigraphic column of the Delaware Basin is shown in Figure 5 below (Yalcin, 2014). Highlighted in red is the Permian section of the stratigraphic column. The Guadalupian series, also referred to as the Delaware Mountain Group, contained within the Permian, is highlighted in green. The Bell Canyon of the Delaware Mountain group is highlighted in yellow. The Guadalupian series has a lower contact with the Leonardian series and an upper contact with the Ochoan series. Within the Guadalupian, the Bell Canyon Formation has an upper contact with the Castile formation of the Ochoan series and a lower contact of the Cherry Canyon Formation for the Guadalupian series.

System	Series	Stratigraphy	
Quaternary	Holocene	Holocene Sand	
Tertiary	Pliocene	Ogallala	
Cretaceous	Gulfian/Comanchean	Limestone	
Jurassic	Absent		
Triassic		Dockum	
Permian	Ochoan	Dewey Lake	
		Rustler	
		Salado	
		Castile	
	Guadalupian	Bell Canyon	Delaware Mountain Group
		Cherry Canyon	
		Brushy Canyon	
	Leonardian	Bone Spring	
	Wolcampian	Wolfcamp	
Pennsylvanian	Virgil-Missouri	Cisco-Canyon	
	Desmoinesian	Strawn	
	Atokan	Atokan	
	Morrowan	Morrow	
Mississippian	Chesterian	Barnett	
	Meramec-Osage.	Mississippi Limestone	
	Kinderhookian		
Devonian	Upper	Woodford	
	Middle	Thirty-one	
Silurian	Upper	Wristen	
	Middle	Fusselman	
Ordovician	Upper	Montoya	
	Middle	Simpson	
	Lower	Ellenburger	
Cambrian	Upper	Cambrian	
Precambrian	Precambrian		

Figure 5: General Stratigraphic Column of the Delaware Basin. The Permian system is highlighted in red, with the Guadalupian series highlighted in green. Lithostratigraphic names associated with basin deposits are provided in the column labeled stratigraphy, and general lithology is provided in the far right column. Image is modified from Yalcin, 2014.

The basin can be divided and described in three discrete, but related areas, the shelf, the shelf margin, and the basin (Figure 2). Figure 2 represents an enhanced litho-stratigraphic section focusing on the Delaware Mountain Group. In Figure 2, the Delaware Basin's carbonate shelf margin evolved over time from a carbonate ramp during deposition of the Brushy Canyon Formation, to a carbonate rimmed shoals of the Goat Seep during deposition of the Cherry Canyon Formation, and the Capitan Reef during deposition of the Bell Canyon Formation.

2.2 Paleogeography

The formation of the Permian basin started towards the end of the Pennsylvanian, and concluded at the end of the Permian (Yalcin, 2017). Evolution of the Permian basin is seen in Figure 6, Figure 7, and Figure 8. The Tobosa Basin, which predated the greater Permian Basin complex, had formed during the Late Precambrian to the Pennsylvanian (Galey, 1958). The collision of Laurasia and Gondwana, during the formation of Pangea, caused movements along lines of Proterozoic weakness (Hills 1984) and generated foreland arc basins and highs resulting in the Delaware and Midland Basins (Figure 7). The two basins were located on the western Edge of Pangea during the early Permian (Figure 7) (Sinclair 2007, Blakey 2013). Throughout the formation of the greater Permian Basin, a progressive aridity in the climate was recorded (Osleger and Tinker, 1999). In the Late Permian, peak-greenhouse conditions during transitioned into peak-icehouse conditions observed in during the Ochoan (Osleger and Tinker, 1999).

Figure 6: Paleogeography of the Middle Pennsylvanian ~308 Ma. Highlighted with a red dashed line just south of the equator is the Tabosa Basin, which preceded the greater Permian Basin. Note that during this dime the Tabosa basin has unrestricted access to the Panthalassa Ocean. Also, during this time Gondwana and Laurasia are colliding in the formation of Pangea. Gondwana is the land mass to in the southwest corner, and Laurasia is in the northern halve of the image. Image modified from Blakey, 2013.

Figure 7: Paleogeography of the Middle Permian ~260 Ma. Highlighted in the orange dashed line is the approximate border of the Delaware Basin and highlighted in the green dashed line is the approximate border of the Midland Basin. Access of the Delaware Basin during this time to the Panthalassa Ocean during this time is increasingly restricted. Laurasia and Gondwana are colliding in the formation of Pangea. Gondwana is the land mass in the southwest corner and Laurasia is in the northern half of the image. Image modified from Blakey, 2013.

Figure 8: Paleogeography during the Early Triassic ~245 Ma Highlighted in the orange dashed line is the approximate border of the Delaware Basin and highlighted in the green dashed line is the approximate border of the Midland Basin. The Delaware and Midland Basins are no longer epeiric seas. Image modified from Blakey, 2013.

The Permian Basin is divided into four main stages of deposition: the Wolfcampian, Leonardian, Guadalupian, and Ochoan. During the Wolfcampian, near the beginning of the Permian, the Permian Basin was an unrestricted sea with consistent communication with the Panthalassa Ocean, as seen in Figure 6 (Blakey, 2013). Towards the end of the Wolfcampian rapid subsidence occurred in the Delaware Basin (Sinclair 2007, Yalcin 2014). During Leonardian time, global sea level began to drop and the Delaware Basin became more isolated. The Midland and Delaware sub basins became more distinct and developed while the greater Permian Basin became more restricted from the Panthalassa Ocean (Blakey, 2013). During this time, subsidence in

17

the Delaware Basin slows (Yalcin, 2014). During the Guadalupian, the Delaware Basin experienced rapid subsidence as sea level continued to drop while the Permian Basin continued to become more and more restricted from the Panthalassa Ocean (Figure 7) (Blakey, 2013). Access to the Panthalassa Ocean or lack thereof was controlled by the Hovey Channel, theorized to be located in the South of the basin by Hill (2000). However, the Hovey channel is conversely theorized to be located in the West of the basin by Pigott (Personal Communication of 2017). As the Hovey Channel closed permanently during the Ochoan, the basin became completely cut off from the Panthalassa Ocean, resulting in the deposition of thick Deepwater evaporate units which mark the end of the Permian (Figure 8).

2.3 Tectonic Evolution

The Delaware Basin originated in the Proterozoic along the edge of the North American Craton as the Tobosa Basin (Hills, 1984; Yalcin, 2014). Early in the Ordovician, sediments were being deposited into a basin caused by the cooling and shrinking of underlying crust and mantle associated with the sagging of a peninsular arch which extended southeastward across southeastern New Mexico and adjacent parts of western Texas (Adams, 1965). While this did not create a structural basin, its subsidence did create a flattened coastal plain across which the Early Ordovician Sea transgressed (Adams, 1965). The passive margin tectonism mentioned above is described as the initial phase of tectonic development by Crosby (2015).

Crustal warping towards the middle of the Ordovician created a 350-mile-wide sag, in the above described negative basin (Adams, 1965). Galley (1958) first defined the 350-mile-wide sag feature as the Tobosa Basin (Figure 9). The ancestral Tobosa

Basin which was bounded on the east by the Texas arch and the west by the Diablo arch

(Adams, 1965), as mentioned in the paleogeography section, was the precursor of the

greater Permian Basin (Figure 9). From this time until the Mississippian, the Tobosa

Basin continued to subside and deepen with deposits keeping pace with subsidence

(Adams, 1965). During the Mississippian, compressional forces caused significant

uplift along the median ridge of the Tobosa basin, creating separation between the

Delaware and Midland Basin observed today as the Central Basin Platform (Hills,

1984). Observed uplift occurred along pre-existing planes of Proterozoic weakness,

causing the Delaware basin to tilt to the east (Hills, 1984).
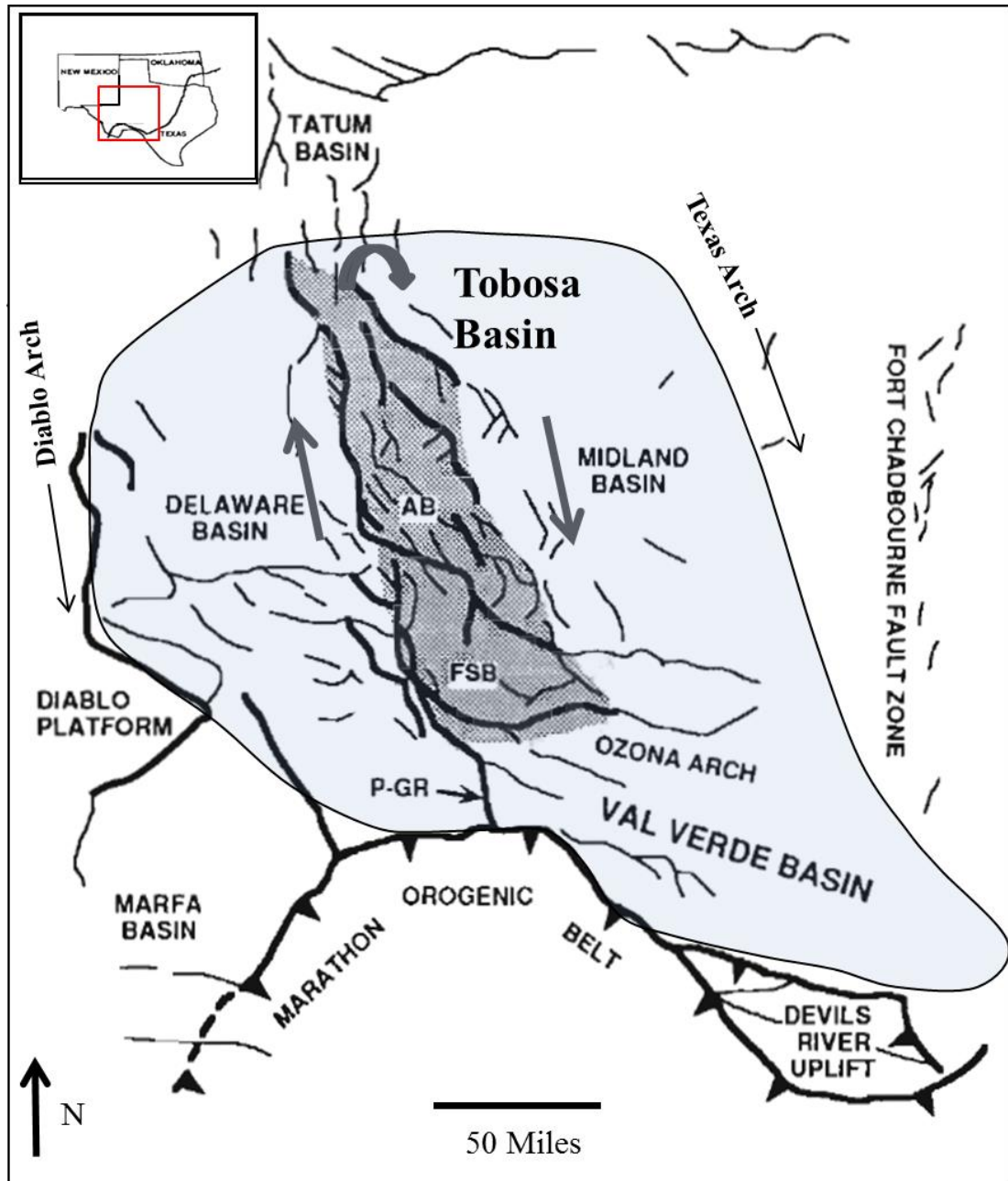
Figure 9: Generalized tectonic map of the Permian Basin. The lighter shaded region outlines the extent of the ancient Tobosa Basin. In darker gray is the outline of the Central Basin Platform. Within the Central Basin Platform, its two constituent fault blocks, the Abdector Block (AB) and the Fort Stockton Block (FSB). Taken from Crosby (2015), modified from Yang and Dorobek (1995).

The Late Pennsylvanian observed rapid subsidence of the Delaware basin in juxtaposition to only mild uplift exhibited by the Central Basin Platform (Adams, 1965). This created a sediment starved basin during this time. In the middle and Late Pennsylvanian, tectonic activity increased throughout the region as a result of Variscan Orogeny (Hills, 1984; Yang and Dorobek, 1995). The compressional forces associated with the increased tectonic activity dramatically uplifted the Central Basin Platform. The observed uplift from compressional forces was exacerbated by increased subsidence of the Delaware Basin interpreted to be caused by flexural loading associated with a flux in sediment sourced from the uplifted Central Basin Platform (Yang and Dorobek, 1995; Yalcin, 2014).

In the Early Permian, the final throws of the Marathon orogeny led to sporadic tectonic activity (Hills, 1984). Slight, frequent movements along ancient zones of weakness on the east of the Delaware Basin allowed the basin floor to subside 1,000 feet below the surrounding carbonate shelves (Hills, 1984). Observed subsidence was accelerated by rapid sediment accumulations during the Wolfcampian, as the previously starved basin during the Pennsylvanian (Adams, 1965) became inundated with sediment. During the Leonardian, the Delaware basin continued to subside, though at a slower rate than previously observed in the Wolfcampian (Adams, 1965). Consequently, throughout the upper Permian, the Delaware basin was tectonically stable during deposition of Guadalupian sediment. The entire basin continued to slowly subside, but at a slower rate than during the lower Permian (Adams, 1965). This relative tectonic stability was maintained throughout the Ochoan.

2.4 Deposition

The development of carbonate ramps began in the Wolfcampian in the north of the basin. Shallow seas and less clastic input contributed to prolific carbonate deposition relative to other areas of the basin (Hills, 1984). During Leonardian times, carbonate ramp development continued in greater portions of the basin margin (Hills, 1984). Through the growth and evolution of the carbonate shelf platform, increasing restriction occurred in the Delaware Basin (Hills, 1984). At the beginning of the Guadalupian, the carbonate shelf continues to evolve, but a significant lithologic shift occurs with basin: Siliciclastic sedimentation was more dominant during this time as opposed to dominantly carbonate deposition during the Wolfcampian and Leonardian (Silver and Todd, 1969). During the Guadalupian, a shift from carbonate ramp to a more rimmed shelf margin was recognized (Adams, 1965).

During the Guadalupian, the Delaware Mountain Group was deposited as a 1,000 – 1,600m thick section of limestone, siltstone and sandstone. This deposit can be divided into the Brushy Canyon Formation, the Cherry Canyon Formation, and the Bell Canyon formation from oldest to youngest respectively (Figure 5 and Figure 2). The basin can be separated into three discrete areas: the shelf, the shelf margin, and the basin (Figure 2). The shelfal deposits were composed of thinly bedded alternations of carbonates and sandstones within a basal back reef environment (Payne, 1976). This back reef environment grades into a very thick, massive reef. The basin deposits are mostly siliciclastic sands and silts pinching out upslope to the shelf margin carbonate rocks (Payne, 1976). These margin carbonate rocks can be observed more distally as carbonate tongues extending as far as 17km into the basin (Lawson, 1989).

Towards the end of the Guadalupian, the Permian Basin is rimmed on all sides by the Capitan Ref Complex which was time equivalent to the Bell Canyon formation in the more distal portions of the basin (Figure 2). While several models for reef geomorphology of the Capitan Reef (shoal rim, reef rim, ect), Garrett (2015) has proposed a shoal rimmed shelf margin model. In a study conducted in Slaughter Canyon, she observed that the shelf margin was predominantly made up of sponges and biomicrite. She observed that the sponges and micritic mud were not compatible for high energy environments, proposing that the sponge and micrite dominated shelf margin was located below wave base.

Within the Delaware Basin, the Bell Canyon contains five inter-tonguing carbonate deposits: the Hegler, Pinery, Rader, McCombs, and Lamar members from oldest to youngest respectively (Figure 2). The Rader Limestone was observed as a detrital carbonate member of the Upper Guadalupian aged Bell Canyon Formation containing coarse, allochthonous carbonate debris with clasts reaching up to 10 m across, deposited in several subaqueous gravity flows (Lawson, 1989). The Bell Canyon is coeval with the Capitan Reef as well as the Queen, Seven Rivers, Yates, and the Tansill Formations of the Artesia Group (Figure *2*). The Rader member of the Bell Canyon Formation is believed to derive from carbonate deposits of the upper Guadalupian Capitan Reef Complex (Lawson, 1989).

The Guadalupian is followed by the Ochoan (Figure 5) which is made up of extensive evaporite deposits. These deposits formed as a result of increasing basin restriction from the Panthalassa Ocean. Following the deposition of the extensive

evaporite deposits, the late Permian regression was completed with the progradation of

terrestrial red beds into the basin (Adams, 1965).

Chapter 3: Methods

3.1 Field Methods

Field observations were taken at four different outcrop locations. The four outcrop locations are identified as Rader Ridge, Reverse Waterfall, Creek Bed, and Road Cut outcrops (Figure 4). The outcrop locations are in order of most proximal to most distal in relation to Guadalupe Mountain slope (Figure 4).

Each measured section described lithology type and bed geometries at one foot intervals. For Measured sections a Jacob Staff was used that measured five feet in length. At the base of each Jacob Staff measurement a GPS measurement was taken. GPS measurements were taken with a Garmin Montana 650t. GPS measurements are accurate to within three meters of the measurement location. While this is a coarser resolution than the ~1.5 meter length of the Jacob Staff used, the GPS measurements are very useful for visualizing the general locations of each measurement as well as tracking lateral movement in the measured section when necessary.

3.2 Spectral Gamma Ray

The Spectral Gamma Ray (SGR) machine was used to measure the natural radiation through the detection of potassium (K), Thorium (Th), and Uranium (U) in counts per second (CPS) and is reported in parts per million (ppm) and weight percent (wt. %). The run time for this analysis is 30 seconds per sample. This data is used to calculate the total gamma ray reading and converted to API units using the equation: $Y\,API\,=\,4\,Th\,+\,8\,U\,+\,16\,K$. Thorium and uranium are measured in ppm and potassium is measured in wt. % (Ellis and Singer 1987).

SGR measurements were taken in a grid system along the Road Cut outcrop. At the road cut, SGR measurements were taken every foot vertically until samples measurements could not be safely taken. A total of 22 vertical sections were taken, covering all distinct lithologic groups. Each vertical section has a 10 meter spacing. Lack of field assistants during some field work allowed SGR measurements to only be taken along the road cut outcrop. This lack of data was supplemented with K, Th, and U readings from XRF measurements.

3.3 X-Ray Fluorescence

In order to maintain cohesive data density between recorded field measurements and XRF and SGR data, XRF measurements were taken every foot at the two measured sections on Rader Ridge and the Measured Section on the Revers Waterfall outcrops. XRF and SGR measurements were taken in a grid system along the Road Cut outcrop. At the road cut, XRF and SGR measurements were taken in the grid system described above in the SGR methods section.

Each XRF measurement was not taken in the field, but rather a hand sample was retrieved from the field every foot as described above. Each sample was cut to provide a flat surface for accurate measurements. The samples were washed in warm soapy water and then thoroughly rinsed to remove all soap and other debris that might contaminate the sample. After washing and rinsing, all samples were placed on gridded and labeled cardboard for 48 hours to dry.

XRF measurements were taken using a Thermo Fisher Scientific Niton XL3t Analyzer. Each cut sample was measured inside of the portable test stand with the XRF remotely controlled from a laptop to reduce radiation exposure to the operator.

Internationally accepted SARM-41 standard provided by Thermo Scientific was employed to assure the accuracy of the XRF measurements. All results are reported in parts per million (PPM).

Before using the XRF, a system check was preformed which calibrates the detector and verifies that the XRF is operating to specifications (Thermo Fisher Scientific, 2010). The Thermo Scientific XL3t analyzer are equipped with excitation filters that optimize the analyzers' sensitivity to various elements (Thermo Fisher Scientific, 2010). Each sample was measured on the TEST ALL GEO mode for 210 seconds. The 210 second run time was used to allow the XRF to pick up both major and light elements and to ensure the accuracy of each scan. The "High Range" filter is used to optimize Barium (Ba) through silver (Ag), the "Main Range" filter provides optimum sensitivity for the elements manganese (Mn) through bismuth (Bi), and the "Low Range" filter is used to optimize the sensitivity for the elements from titanium (Ti) through chromium (Cr) (Thermo Fisher Scientific, 2010). Major elements are detected using the "High Range", "Main Range", and "Low Range" filters which each have a run time of 60 seconds. The "Light Range" filter is used to detect light elements and has a run time of 90 seconds. The results were used to create elemental profiles to use as geochemical proxies for paleo-environments, lithologic composition, and provenance.

Lithologic composition where generated using a script written in Microsoft Excel by Dr. John D. Pigott which incorporated elemental concentrations of iron (Fe), sulfur (S), magnesium (Mg), calcium (Ca), aluminum (Al), silicon (Si), and strontium (Sr) taken from pure mineral samples taken from the University of Oklahoma's mineral

collection. These measured standards were used to calculate the amount of pyrite,

gypsum, calcite, dolomite, quartz, potassium feldspar, and clay.

3.3.1 XRF Pseudo GR

Mentioned above, a lack of field assistants did not allow SGR measurements to

be taken at the Rader Ridge outcrops or the Reverse Waterfall outcrop. Instead pseudo

total gamma ray curves were generated from XRF measurements. XRF readings of U,

Th, and K were converted to API using the equation:

$$\Upsilon \, API = 4\,Th + 8\,U + 16\,K$$

Where thorium and uranium are measured in ppm and potassium is measured in wt. %

(Ellis and Singer 1987). To check the viability of such a practice I compared the SGR

and XRF pseudo GR curves to one another from the Road Cut outcrop where both sets

of data where available. The results showed a strong linear relationship between the

API curves generated from SGR measurements and converted XRF measurements API

curve, seen below in Figure 10.
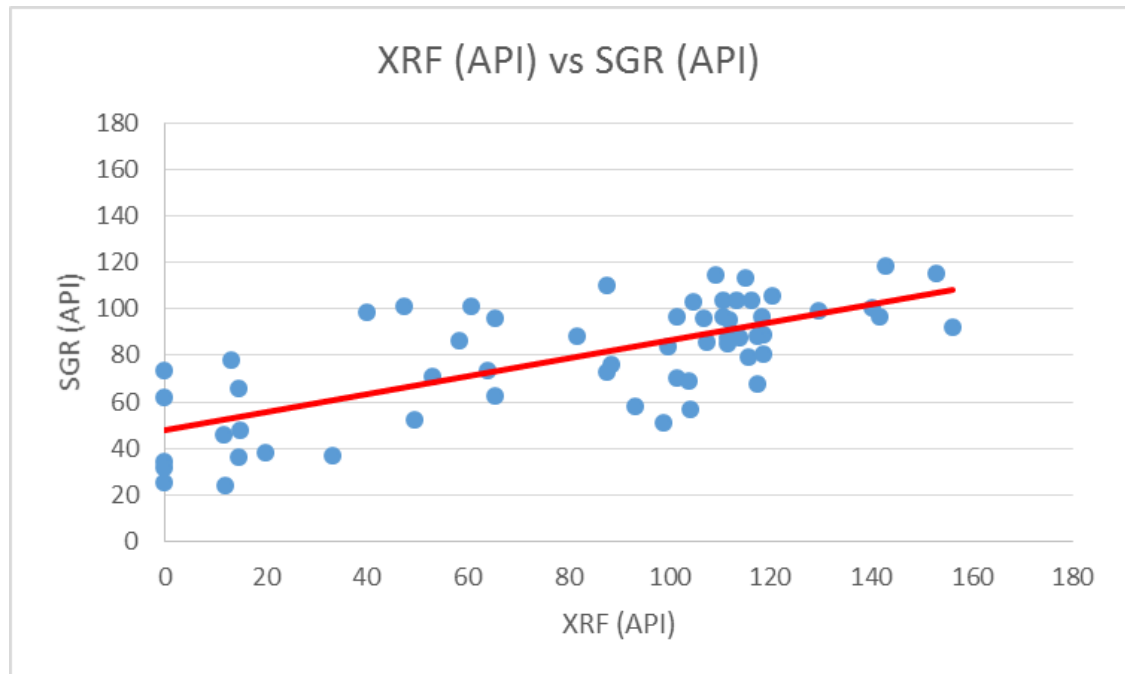
Figure 10: Cross plot of SGR (API) values and XRF (API) values. There is a strong positive correlation between the two measurements. While not a perfect match, this is expected as the sampling size of the two measurements is different with SGR having a measuring surface of 38.5cm², and the XRF having a measurement surface of a few mm². Additionally differences are expected due to the difference in measurement technique with the SGR being a passive measurement and the XRF being an active measurement.

In addition to the XRF (API) and SGR (API) data having a strong, positive correlation (Figure 10), the XRF (API) data matched the trend of the SGR (API) data very closely when plotted as vertical curves seen below in Figure 11. The matching of the trends makes XRF (API) a reasonable substitute where SGR measurements are not available (personal communication with Dr. John D. Pigott).
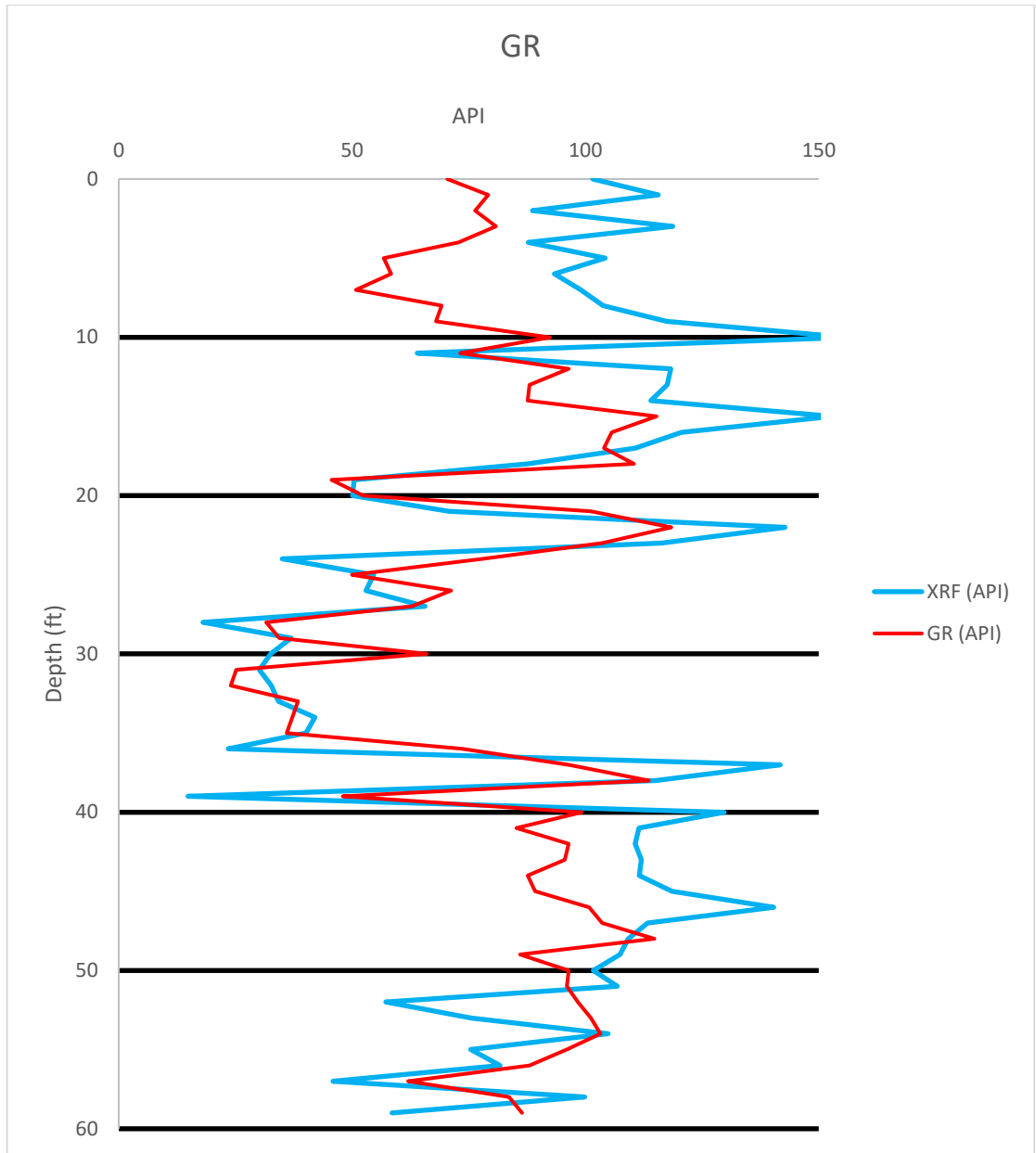
Figure 11: GR (API) seen in red, overlain with XRF (API) seen in blue. While the values of the two curves do not match perfectly, general trends correlate very well. Because of this, it is concluded that XRF measurements of U, TH, and K are an appropriate substitute for SGR values when not available.

3.4 Light Detection and Range Device (LiDAR)

3.4.1 Field Collection

LiDAR data was acquired at the Road Cut and Creek Bed outcrops. The amount of hostile terrain needed to traverse to get to the Rader Ridge and Reverse Waterfall outcrops would have created an unsafe environment due to the weight and bulk of equipment required to perform LiDAR data acquisition. A RIEGL VZ-400i 3D terrestrial laser scanner with an attached Nikon D810 with a Nikor 20mm lens was utilized in this study. The LiDAR has a range of up to 800m with an accuracy of 5mm and precision of 3mm. 5cm flat reflectors were placed on flat vertical surfaces, tree branches, and any feature that could hold the reflector where the LiDAR could record its position. 10 cm cylinder reflectors where placed on top of outcrops where possible in positions where the LiDAR could record their positions.

Using LiDAR allows the operator to scan from various locations along an outcrop and compile scans together in order to create a high resolution 3D model of the outcrop. The reflectors mentioned above are used as common points within each discrete scan and are used to tie multiple discrete scans together. At least three common reflector points are needed between each scan position in order for the discrete scans to be accurately combined (RIEGL, 2013). Scan positions are determined based on the geometry of the outcrop to minimize the area of shadow zones, and maximize the number of reflectors shared between each discrete scan.

After reflectors are placed and scan positions are determined the Lidar, with camera attached, is set up on a tripod and connected directly to a laptop via an ethernet cord for data to be transferred in real time from the LiDAR to the laptop. All data

recorded is stored in RiScan Pro v2.3.2. At each scan position a 360° panorama scan is taken with a resolution of 0.02 degrees and a laser pulse repetition rate (PRR) of 300 kHz. The pose estimation, which is the LiDAR internal GPS positioning, is set to FAST. Each scan has a run time of 15 minutes. During each scan six photos are taken with the mounted camera in a 360° manner, each containing 20% of overlap. Longitude and latitude of each scan position is recoded internally by the GPS located on top of the LiDAR during the pose estimation, and an additional 3 GPS measurements are recorded with a hand held GPS as back up. After the conclusion of each 360° panorama scan, all visible reflectors are identified within the scan and designated as either a 5cm flat reflector or 10cm cylinder and are registered as a tie point.

After all visible reflectors are registered as tie points, portions of the outcrop are selected and fine scans with a resolution of 0.005 degrees are performed. These scans vary in duration depending on the size of the selected area. In all but the first scan, after all visible reflectors have been identified, their type designated, and a FineScan preformed, the operator must find corresponding tie points with all previous scan positions in RiScan Pro. After these steps are completed, the Lidar is moved to the next scan position. This process allows the operator to deliberately integrate LiDAR data to form a detailed, cohesive image of the outcrop.

A total of sixteen scans were taken over the course of three days. Eleven scan positions were utilized in the scanning of the Road Cut outcrop, six for the north side of the road cut and 5 for the south side of the road cut, and five scan positions were exploited in the scanning of the Creek Bed outcrop. Scans one through three imaged the north side of the Road Cut and were taken on October 28, 2016. Temperatures

ranged from 70°F to 79°F, with wind speeds averaging 11mph (SW). Visibility was excellent with little to no overcast throughout the day. The camera settings were:

- Shutter speed: 1/250 seconds
- Aperture: f/22
- ISO: 250

Scans four through eight imaged the south side of the Road Cut, and scans nine through eleven imaged the remainder of the north side of the Road Cut. These scans were taken on October 29, 2016. Temperatures ranged from 67°F to 82°F, with wind speeds averaging 11mph (WSW). Visibility was excellent with little to no overcast throughout the day. The camera settings were:

- Shutter speed: 1/250 seconds
- Aperture: f/22
- ISO: 250

Scans twelve through sixteen imaged the Creek Bed outcrop. These scans were taken on October 30, 2016. Temperatures ranged from 70°F to 82°F, with wind speeds averaging 10 mph. Visibility was excellent with little to no overcast, however, lighting did vary significantly (more so than at the Road Cut) with the first scan being very dark and the last scan being brighter due to the position of the sun relative to Creek Bed Outcrop. The camera settings were:

- Shutter speed: 1/250 seconds
- Aperture: f/22
- ISO: 250

3.4.2 Processing

After all LiDAR data is collected, it is processed using RiScan Pro v2.3.2. Raw scans are visualized as point cloud data. Depending on the size and resolution of the scans each can contain hundreds of millions of individual data points. A point cloud is defined as, "a set of points with coordinate values in a well-defined coordinate system" (RIEGL Glossary, 2012). Each point can be defined on a global coordinate system or within the scanner's own coordinate system (SOCS) (RIEGL Glossary, 2012). Poly data, or copies, of all the scans are created in order to protect the integrity of the original data from mistakes that occur during processing. These poly data are brought in one scan at a time and are cropped individually or as a composite, depending on the size scans, to where only the outcrop of interest is left in order to reduce loading and processing times. The cropped poly data are then run through an octree filter which thins the point cloud by removing and merging points based on the desired cubic structure of the filter. After the octree filter has run, one cube will contain one point which is the center of gravity of the averaged points which generally represents a larger number of points (RIEGL, 2013). This allows for zones of heavy clustering to be thinned without losing resolution, and allows for further filtering to be done (RIEGL, 2013).

Besides coordinates, each point in a point cloud contains additional attributes, such as amplitude and reflectance. Amplitude refers to the amplitude of the echo signal reaching the laser scanner. The amplitude attribute is related to a number of parameters, including the emitted laser pulse peak power and the receive aperture, but also including target parameters like the target's reflectance and range (RIEGLE Glossary, 2012).

Thus, for every detected echo signal an amplitude reading which reflects the amplitude of the optical echo signal is generated and presented in the units of decibel (dB) (RIEGL Glossary, 2012). Reflectance, on the other hand, is solely a target property and refers to the fraction of incident optical power that is reflected by that target at a certain wavelength (RIEGL Glossary, 2012). The reflectance is a ratio of the actual amplitude of that target to the amplitude of a white flat target at the same range, oriented orthonormal to the beam axis with a size in excess of the laser footprint (RIEGL Glossary 2012). Reflectance values are also given in decibels (dB).

Both amplitude and reflectance have drawbacks as amplitude is dependent on the range of the target, while reflectance is highly affected by the angle of the target, the range and angle at which scans are taken have significant implications that must be considered when determining how to best analyze the data. After reviewing the data acquired in this study it was determined that processing the data using reflectance provided superior imaging of the outcrop and also provided qualitative insights into the lithologies present in the outcrop. Additionally, previous studies (Giddens 2016; Garrett 2015) showed that reflectance provided a greater ability to analyze the lithology and even minerology of outcrops. All of the analysis and interpretation is done using reflectance.

3.4.3 Post Processing

The most valuable aspect of using LiDAR data is its ability to combine different

data together in a cohesive format (Figure 12).
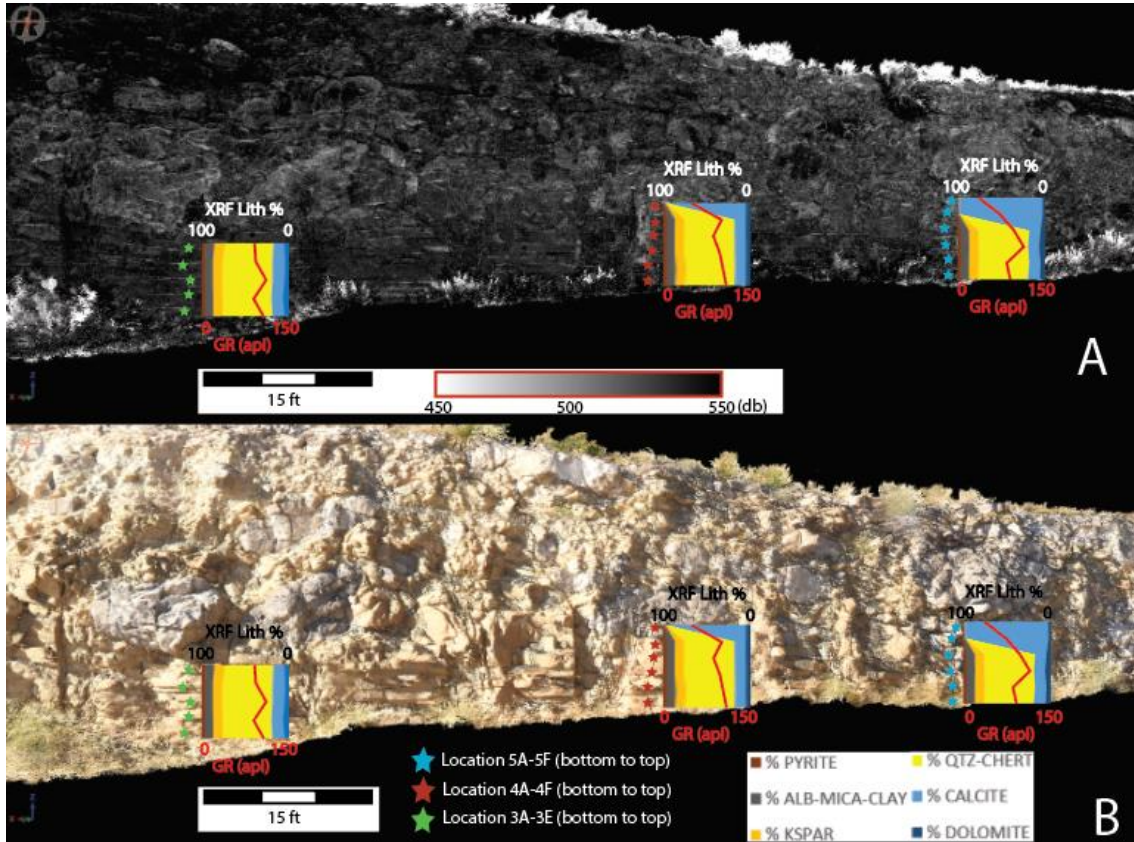
Figure 12: Images showing scans of the same section of outcrop at the Road Cut locality. Both images have XRF lithology and GR curves laid on top of corresponding vertical sections of outcrop. Observe the change in lithologies moving from homogeneous sandstones of the Bell Canyon Formation at the base of the section into the Mega Conglomerate Unit which contains sandstone and large carbonate boulders. (A) Scan displaying reflectance range of 450 to 550 dB in a black and white color bar. (B) Scan displaying true color.

Using LiDAR to integrate different data types is useful for visualization purposes as well as to check the data. In Figure 12, the lithology logs change as expected when moving from a clean sandstone unit in location 3 into a Mega Conglomerate Unit which contains large carbonate boulders at the top of location 4 and 5. Using LiDAR in this way also gives perspective to lateral heterogeneities that are not observed in one dimensional measurements such as vertical transects seen in locations 3 through 5 (Figure 12). Additionally, consequences of measurement intervals can also be identified. For example at the top of the location 5 vertical transect (Figure 12), the base of the Mega Conglomerate Unit has a sandstone matrix surrounding smaller limestone cobbles beneath a large carbonate boulder. The 1 ft measurement interval applied to the XRF and GR measurements only measured carbonate cobbles and not the sandstone matrix in between (Figure 12). Having this insight allows for a more complete and comprehensive interpretation of data that would not be possible if only looking at lithology curves generated from XRF measurements.

Figure 12 also exhibits how LiDAR data, when used in conjunction with other data types, can be used to create an accurate vertical compilation of measurements. Accumulating data from along the outcrop was accomplished by translating measurements from individual vertical sections up dip along discrete bedding planes to create an accurate vertical log with no repeating or missing measurements. Using this technique at the Road Cut locality of this study, allowed for XRF and GR measurements taken in a grid fashion to be transformed into a vertical composite of the Rader formation for correlation purposes.

Chapter 4: Observation

This section will discuss all observations and results of different methods used in the study of the Rader Formation individually at each outcrop location. Following the description of the Rader Formation of, the Rader is broken into three main sub groups, the lower Rader, the middle Rader, and the Upper Rader unit (Lawson, 1989).

The lower Rader Unit is only observed in the more proximal, toe of slope type locations of Rader Ridge and the Reverse Waterfall outcrops. At the more distal medial slope localities the lower Rader interval is not observed because it has been completely eroded (Table 1). Where observed, the lower Rader unit is made up of thin to thickly bedded limestone which exhibit massive and graded bedding. There is limited siliciclastics observed as the unit is dominated by carbonate rocks, but this observation could be affected by large sections of outcrop which are covered by vegetation.

The middle Rader is made up of a clast and matrix supported mega breccia in more proximal, toe of slope localities of Rader Ridge and the Reverse Waterfall. In more distal, basin margin setting observed at the Creek Bed and Road Cut outcrops, the middle Rader unit is observed as a matrix supported mega conglomerate in which large carbonate boulders are entrained in a fine grained sandstone matrix.

The upper Rader unit exhibits characteristics similar to the lower Rader unit, with the only difference between the two is that the upper Rader Unit is observed in both the proximal, toe of slope setting, as well as more distal, medial slope margin setting. Besides the Rader Formation and its sub units, the Pinery Formation and Bell Canyon Sandstone are also observed in both the proximal and distal outcrop locations beneath the Rader Formation.

The more distal outcrops observed at the Creek Bed and Road Cut locations are able to be further subdivided because of the exceptional quality of the outcrops in comparison to those observed in the more proximal settings. Here, outcrops are subdivided into nine distinct lithologic groups (Table 1). Some of the names used are taken from previous studies. From stratigraphically lowest to highest they are the Pinery Formation, Bell Canyon Sandstone Unit One, mega conglomerate, Bull Head Turbidite (Koss, 1977; Lawson, 1989; Nestell et al., 2006), thin interbedded limestone and sandstone one, Debrite One (Nestell et al., 2006), thin Interbedded Limestone and Sandstone Unit Two, Debrite Two (Nestell et al., 2006), and Bell Canyon Sandstone Unit Two. Table 1 below summarizes the different terminology used at the proximal and distal outcrop locations and shows which units are stratigraphically equivalent.

Formal Name	Unit Subdivisions Observed in Proximal Outcrops	Unit Subdivisions Observed in Distal Outcrops
Bell Canyon Formation	Covered	Bell Canyon Sandstone Unit 2
Rader Formation	Upper Rader Unit	Debrite 2
		Interbedded Limestone and Sandstone Unit 2*
		Debrite 1
		Interbedded Limestone and Sandstone Unit 1*
	Middle Rader Unit	Bull Head Turbidite
		Mega Conglomerate Unit*
	Lower Rader Unit	Eroded
Bell Canyon Formation	Bell Canyon Formation	Bell Canyon Sandstone Unit 1
Pinery Formation	Pinery Formation	Pinery Formation

* Name given in this study

Table 1: Summary of subunits observed at proximal and distal outcrop localities. Units within the same rows are equivalent stratigraphically to one another. The colors filling the individual cell represents the dominant lithology observed in each unit with light blue representing carbonates, yellow representing sandstone, and red indicating that the unit was not observed. The green boundary highlight the sub units which comprise the Rader formation as a whole. The Pinery Formation represents the lowest stratigraphic unit, while the Bell Canyon Sandstone Unit Two represents the highest stratigraphic unit.

Moving forward, results and observations will be presented by outcrop location moving from the most proximal locations to the most distal locations. This will allow for the coherent presentation of data for the entire study, as different outcrop locations contain different data sets. Additionally by organizing the observations and results in this fashion, comparison of results and observations between locations is facilitated.

4.1 Rader Ridge Observations

The Rader Ridge outcrop is the most proximal Locality to the Capitan Reef slope (Figure 4). At this location two sections were measured, Rader Ridge Proximal and Rader Ridge Distal, with each described in 1 foot intervals. Additionally, XRF measurements were taken every foot and used to generate geochemical proxy suites as well as a total pseudo total gamma ray curves. The Proximal and Distal Rader Ridge measured sections are 0.25 mi away from each other. The Rader Ridge Proximal measured section is a total of 52 ft and contains the middle Rader unit and the upper

Rader Unit. The Rader Ridge Distal measured section is a total of 209 ft and contains

the lower Rader unit, middle Rader unit, and upper Rader Unit (Lawson, 1989).

4.1.1 Rader Ridge Pseudo Total Gamma Ray and Lithology Log

Pseudo total gamma ray logs and lithology logs (Unpublished software from

Pigott) are presented below for both the Rader Ridge Proximal and Rader Ridge Distal

measured sections. The proximity of the measured sections provides insights into the

variability or lack thereof in the Rader Formation from proximal to distal measured

sections.

4.1.1.1 Rader Ridge Proximal Observations

Figure 13 below displays the pseudo total gamma ray log and the lithology log

generated from XRF measurements for the Rader Ridge Proximal measured section.

The entire Rader Ridge Proximal measured section is dominated by calcite. Dolomite

remains a steady presence throughout the measured section reaching the highest

concentration of 10% of the total lithology immediately above the top of the middle

Rader unit. Quartz and kspar are negligible through the middle Rader interval,

however, the kspar content does increase towards the top of the middle Rader unit. In

the upper Rader unit there is an increase in quartz observed with a large spike occurring

above ten ft.

The total pseudo gamma ray curve has a large spike observed at 48 ft, but there

is no corresponding spike observed in the lithology log. Moving up the measured

section from the large spike, the pseudo total gamma ray curve has an overall decrease

throughout the entire middle Rader unit. The upper Rader unit displays an overall

increasing trend.

The total pseudo gamma ray representing the Rader Ridge Proximal measured section shows a clean gamma ray profile. The middle Rader Unit containing the mega breccia has a more variable total pseudo gamma ray than the overlying upper Rader interval. In the upper Rader unit, the interval from seventeen ft to nine ft displays the cleanest total pseudo gamma ray. This correlates to a normally graded limestone unit which has coarser grains and is interpreted to have higher process energy than the overlying beds made up of thin bedded, very fine grained laminated limestone and interbedded very fine grained sandstone and limestone. The total pseudo gamma ray profile seen below in Figure 13 correlates well to the total pseudo gamma ray profile observed in the Rader Ridge Distal measured section from 62 ft to thirteen ft (Figure 14).
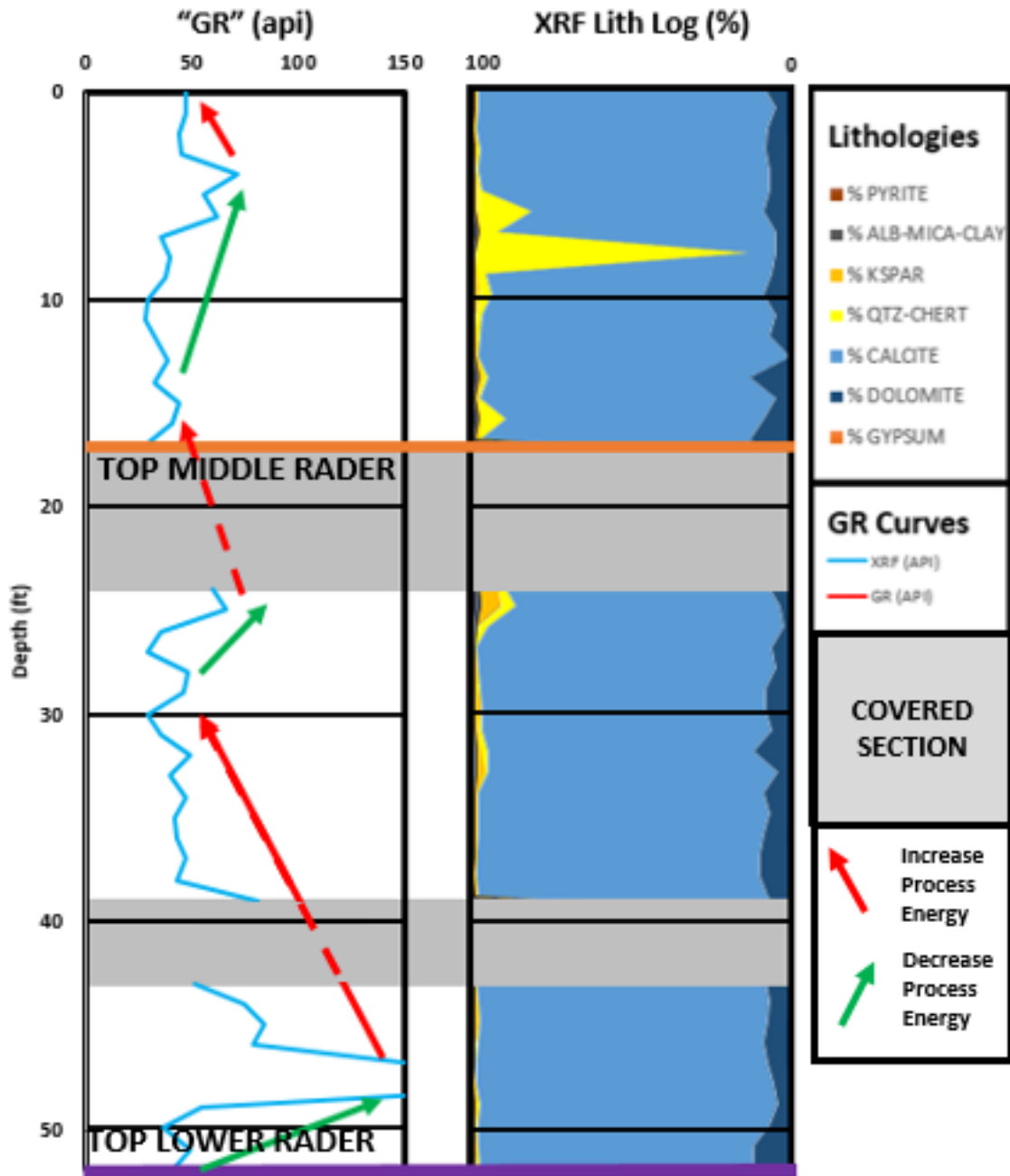
Figure 13: Total gamma ray generated from XRF measurements (blue curve) shown in API units. Base of the Rader Ridge proximal measured section is seen at 52 ft and the top of the outcrop is measured at 0 ft. Lithology curve and legend seen on the right including lithology log coloring, GR curve coloring, and process energy trends.

4.1.1.2 Rader Ridge Distal Observations

Figure 14 below displays the total pseudo gamma ray log and the lithology log for the entire Rader Ridge Distal measured section. The highest levels of pyrite, quartz, clay and kspar are observed at the base of the lower Rader unit in the Rader Ridge Distal measured section. Clay, quartz, kspar, and pyrite content decrease moving up section from the base of the lower Rader unit, however, large, isolated spikes in quartz continue to be observed, though with less frequency. This matches field observations at the Rader Ridge Distal measured section, with the highest concentration of thin, interbedded limestone and sandstone beds observed at the base of the lower Rader interval. Calcite is the dominant constituent throughout the lower Rader unit, with dolomite maintaining low concentrations. The highest total pseudo gamma ray values are observed at the base of the lower Rader unit where the highest siliciclastic content is observed. Spikes observed in total pseudo gamma ray in the lower Rader unit match well with observed increases in clay and kspar in the lithology log.

The total psuedo gamma ray shows an overall decreasing trend moving upwards from the base of the lower Rader unit to the top of the unit. Within this overall decreasing trend are three cycles of increasing and decreasing trends. The intervals with the cleanest total pseudo gamma ray curves in the lower Rader unit correlate well to field observations of intervals of graded limestone beds. These intervals are from 205 ft to 200ft, 172 ft to 165 ft, 160 ft to 165 ft and 141 ft to 132 ft (Figure 14). Total pseudo gamma ray values are more variable, representing thinner, finer grained limestone beds as well as thin interbedded limestone and sandstone intervals.

The middle Rader unit has an increase in dolomite observed, with isolated spikes in dolomite content becoming more frequent in the middle of the middle Rader unit. Dolomite content in the middle Rader interval is higher, and more sproadic than observed in the middle Rader unit of the Rader Ridge Proximal measured section. Calcite remains the dominant lithology throughout the middle Rader interval. Frequency and magnitude of quartz content decreases in the middle Rader unit relative to the lower Rader unit. Total pseudo gamma ray exhibits an overall decreasing trend for the entire middle Rader unit. Within this trend are two cycles of increasing then decreasing total pseudo gamma ray. The decreasing trends correlate with increases in calcite content while the increasing trends correlate to increases in clay, kspar, and quartz content. As mentioned above, the total pseudo gamma ray curve from 62 ft to the top of the middle Rader unit correlates well with the total pseudo gamma ray curve from the Proximal Rader Ridge measured section. However, higher concentrations of dolomite and quartz are observed in the Distal Rader Ridge measured section than in the proximal Rader ridge in this interval.

The upper Rader unit has a constant lithology profile that is dominated by calcite. A single spike containing elevated concentrations of quartz, kspar, and clay is observed at16 ft. Dolomite content is slightly decreased compared to the middle Rader unit and is less sporadic than observed in the middle Rader unit. Total pseudo gamma ray reveals an overall slight increasing trend from the base of the upper Rader unit to the top of the measured section with a spike observed in connection to the spike of clay, kspar, and quartz observed at sixteen ft. The lowest total pseudo gamma ray values observed at the base of the upper Rader interval and matches field measurements which

observe coarse grained graded limestone beds at the base of the upper Rader, with finer laminated and massive limestone beds observed moving upwards to the top of the upper Rader interval.
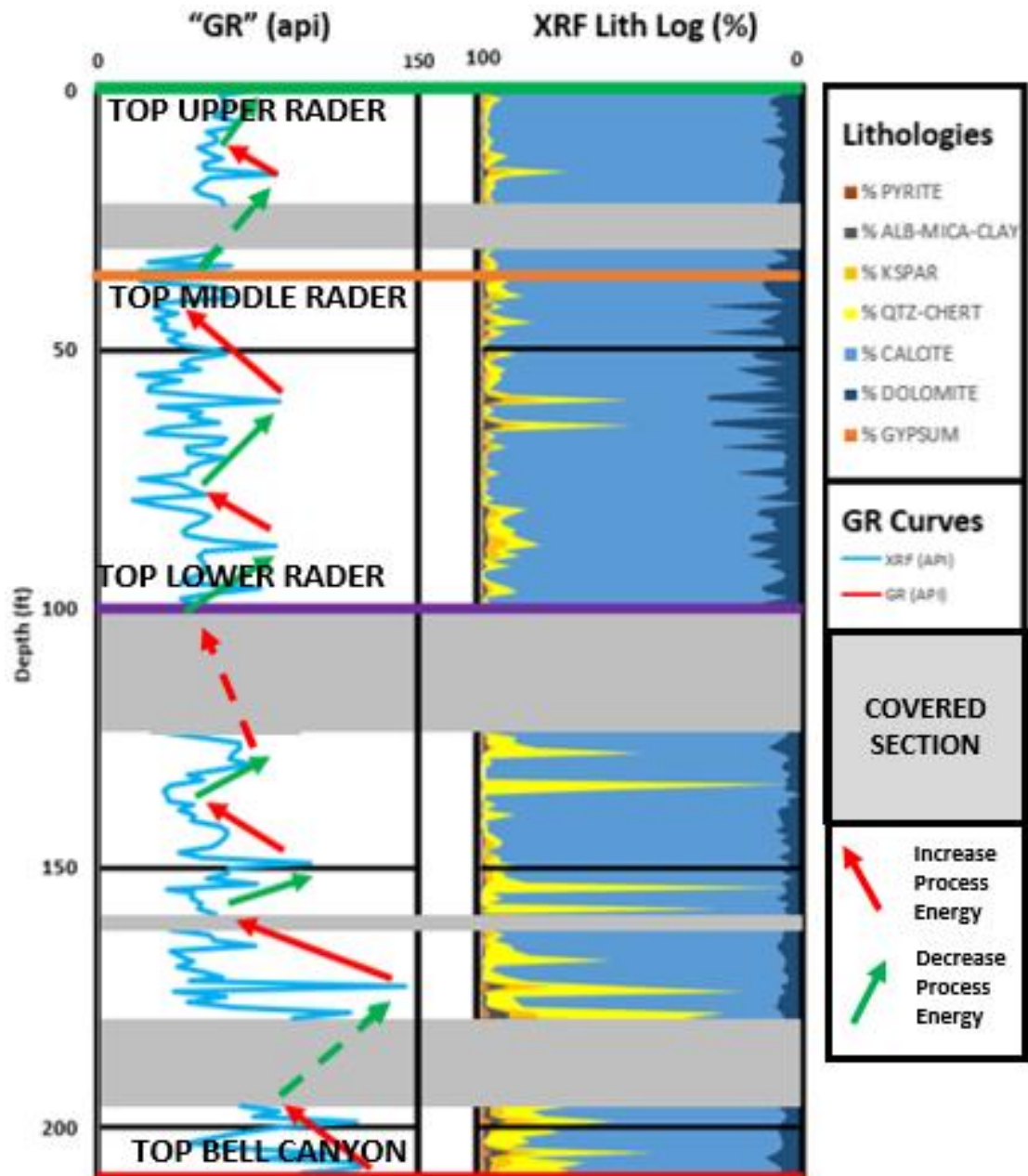
Figure 14: Total gamma ray generated from XRF measurements (blue curve) shown in API units. Base of the Rader Ridge distal measured section is seen at 210 ft and the top of the outcrop is measured at 0 ft. Lithology curve and legend seen on the right including lithology log coloring, GR curve coloring, and process energy trends.

4.1.2 Rader Ridge Lithofacies Observations

The lithologies observed on Rader Ridge are dominantly carbonate with sandstones and siltstones making up a small portion of the lithology (Figure 13 & Figure 14). The carbonate rocks observed are divided into five distinct lithofacies. These lithofacies are fine grained massively bedded limestones, very fine grained laminated limestones, normally graded limestone, bioturbated limestones, and a matrix-supported and clast-supported mega breccia. Additionally, a mixed carbonate-siliciclastic lithofacies is observed. The mixed carbonate-siliciclastic lithofacies is thin interbedded very fine grained sandstone and limestone.

Fine grained, massively bedded limestone is common in the upper and lower Rader members on Rader Ridge, occurring between the thicker intervals of graded limestone beds described below (Figure 15(2)). These beds are thin to medium bedded ranging from 6 inches to 3 ft in thickness and are light to medium gray. These fine grained limestones consist of non-skeletal and skeletal allochthonous grains.

Very fine grained, laminated limestone is also found throughout the upper and lower Rader units on Rader Ridge (Figure 15(1)). These units, like the massively bedded limestones, occur between the thicker graded limestone units observed in the upper and lower Rader units on Rader Ridge. These units are thin bedded with unit thicknesses ranging from 2 inches to 1 ft. The individual laminations range from 0.25 inches to 1 inch in thickness. This lithofacies is observed as repeating intervals of light and dark gray very fine grained limestones (Figure 15(1)).

Graded limestone beds are observed in both the lower and upper Rader units on Rader Ridge. These units are the best preserved at the outcrop. At the Rader Ridge

48

distal measured section, four distinct graded deposits are observed in the lower Rader unit, while only one graded limestone bed is observed in the upper Rader interval. At Rader Ridge Distal, graded limestones are measured in the lower Rader unit from 205 ft to 200 ft, 172 ft to 165 ft, 160 ft to 165 ft and 141 ft to 132 ft; in the upper Rader unit of Rader Ridge Distal a graded limestone is measured from 22 ft to 16 ft. In the Rader Ridge Proximal measured section a graded limestone bed is observed in the upper Rader unit from 17 ft to 9 ft. The graded limestone intervals observed in the upper Rader unit at both the Rader Ridge Proximal and Rader Ridge Distal measured sections are correlative, with both lying directly on top of the middle Rader unit.

The graded limestone beds are medium to thick bedded, ranging in thickness from 1 ft to 5 feet thick. The graded beds are usually fossiliferous, but also contain carbonate angular to sub angular non-skeletal grains (Figure 15 (6)). Common macro fossils observed in the field are crinoid fragments, sponges, and rugose corals. Distinct grain size separations of these beds is commonly observed and interpreted to represent turbidite deposits. A full Bouma A through Bouma E sequence is never observed, but incomplete Bouma sequences are frequently observed (Figure 15(6)).

Bioturbated limestone deposits are only found in the lower Rader unit at the Rader Ridge outcrop. The bioturbated beds are thinly bedded, very fine grained, alternating dark and light gray limestone units (Figure 15(4)). Though the basin was believed to be anoxic during the deposition of the Rader Formation (Lawson, 1989), these isolated bioturbated beds indicate that some oxygenated waters were present, however, the isolated nature of the bioturbation indicates that the presence of oxygen

was possibly short lived. This interpretation might indicate that oxygenated waters were brought down into the basin by some of the subaqueous sediment gravity flows.

Oxidized chert nodules are commonly found in all of the above described beds, with no apparent preference for any specific lithofacies. The chert nodules vary in size from less than 1 inch to greater than 6 inches in their longest exposed dimension (Figure 15(2)). Curiously, the chert nodules are most often observed in stratigraphically equivalent positions within the beds which they are found in (Figure 15(2)). The equivalent stratigraphic position of these nodules indicates they are time equivalent. The final distinct carbonate lithofacies observed at the Rader Ridge outcrop is clast-supported and matrix-supported mega breccia (Figure 15(5)). This lithofacies constitutes the middle Rader unit and contains ungraded intraclasts ranging from gravel sized to greater than 2 ft in their longest exposed dimension. This lithofacies has an erosive contact with the underlying lower Rader strata at both the Rader Ridge Proximal and Rader Ridge Distal measured sections. The thickness of this interval varies between the two measured sections. The mega breccia interval is 30 ft thick at the Rader Ridge Proximal measured section and is 60 ft thick at the Rader Ridge Distal measured section. The intraclasts are angular to sub rounded and are entrained in a light tan very fine grained calcarenite matrix. The unit is poorly sorted and has intervals of higher and lower fossil content in both the intraclasts as well as the matrix. Frequently, large oxidized sponges are observed within this interval. Additional macro fossils observed are crinoid stems, rugose corals, and bryozoans.

Fine grained, interbedded limestone and sandstone units are found throughout the lower and upper Rader Units on Rader Ridge, though they are most common at the

base of the lower Rader unit. These units are thinly bedded and almost always observed as repeating intervals of light to dark gray limestone interlayered with light tan, very fine grained sandstone (Figure 15(3)). These units are made up of very fine grained limestone and sandstone.
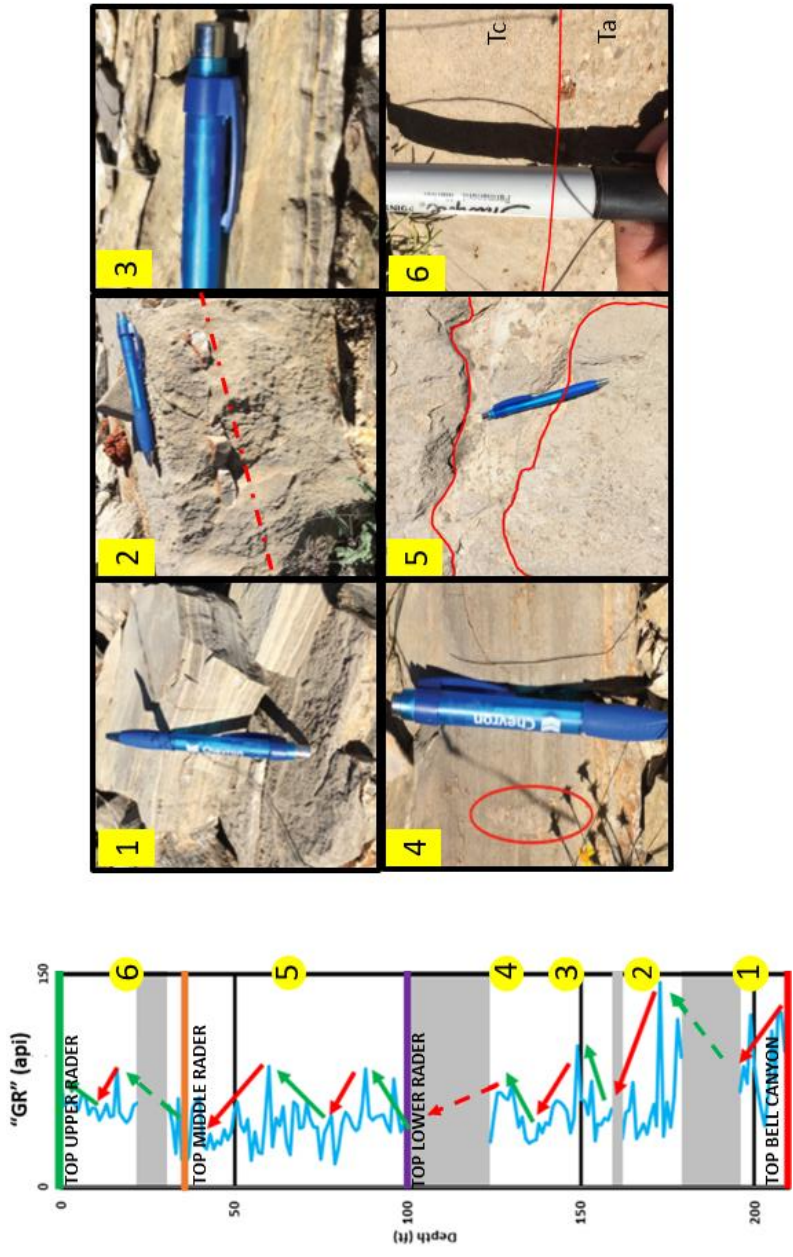
Figure 15: Lithofacies observed on Rader Ridge with 6 inch pen for scale. 1) Repeating intervals of light and dark gray very fine grained laminated limestone. These cycles are thought to demonstrate changes in organic matter preservation or greater organic matter deposition relative to carbonate deposition. 2) Massively bedded limestone unit. Note the discrete chert nodules oriented along the same stratigraphic level within the limestone bed. 3) Interbedded fine grained limestone and sandstone unit. 4) Bioturbation observed in laminated limestone. 5) Carbonate mega breccia with carbonate intraclasts within a tan calcarenite matrix. 6) Graded limestone bed with sub angular to sub rounded intraclasts at the base of the bed.

52

4.1.3 Rader Ridge Geochemical Proxy Observations

Geochemical proxies are utilized throughout this study at all outcrop locations except for the Creek Bed outcrop. The information below is a detailed background on geochemical proxies which serves as background for all geochemical proxy observations and interpretations found in this report.

Whole rock, inorganic geochemistry is a vital analysis which helps geoscientist gain a fuller understanding of ancient depositional environments. Advances in techniques used to measure the inorganic chemistry of rocks has propelled this discipline, making it more affordable and a less time sensitive enterprise. Such advances include the introduction of hand held tools such as the XRF, utilized in this study, allow for time efficient, nondestructive measurements to be taken in the field or in the lab. Smith and Malicse (2010) state that the handheld XRF provides the perfect tool to log the inorganic geochemistry of rocks down to the sub cm scale. These techniques are especially useful when analyzing sequences of similar rock type that vary little in terms of grain size, structure, or color over large vertical intervals. Accurate stratigraphic control in these monotonous sequences can be enhanced by chemostratigraphic techniques employing major, minor and trace element abundances and ratios (Smith and Malicse, 2010). R.M Slatt et al., (2012) and Slatt and Rodriguez (2012) also show that lithologic successions of visually homogeneous rock can contain significant heterogeneity. Chemostratigraphic analysis can readily identify these heterogeneities through chemostratigraphic analysis (Nance and Rowe, 2015; Turner et al., 2015).

As it applies to the discipline of stratigraphy, the used of inorganic or trace metal geochemistry focuses on the use of elemental proxies that indicate certain characteristics about a rock sample's provenance, depositional history, water mass conditions, and paleoenvironment (Crosby, 2015). Turner et al., (2015) note that certain elements act as proxies for local depositional and environmental conditions during sedimentation. Nance and Rowe (2014) further indicate that these elemental proxies also have a direct use in sequence stratigraphy as certain elements become enriched or depleted during sea level lowstand and highstand respectively.

In this study, the same procedures and analysis conducted in Crosby (2015) are applied due to similarity between the lithologies and transportation mechanisms observed in the Bone Spring Formation (Crosby, 2015), and the Rader Formation of this study. The following elements and ratios thereof were used based on their reliability as proxies, abundance in transported material as stated by Sageman and Lyons (2004), K.L Pigott (2007), and Parra-Galvez et al., (2009): silicon (Si), Iron (Fe), titanium (Ti), zirconium (Zr), aluminum (Al), potassium (K), phosphorous (P), calcium (Ca), strontium (Sr), magnesium (Mg), manganese (Mn), molybdenum (Mo), vanadium (V), cobalt (Co), nickel (Ni), copper (Cu), thorium (Th), and uranium (U) (Crosby, 2015).

Using geochemical proxies to understand the provenance and lithologic makeup of the Rader Formation provide a fully integrated record of earths past, and offers the opportunity to open a clearer window into the paleoenvironement at time of deposition (Sageman and Lyons, 2004). However, one cannot rely on a single elemental proxy to make an accurate interpretation as overprinting from different causes may occur. As such, Sageman and Lyons (2004), Parra-Galvez et al., (2009), and Tuner et al., (2014)

suggest that multiple elemental proxies be investigated to reduce the risk of interpreting post-depositional overprinting, such as diagenetic alterations as paleoenvironment proxies (Crosby, 2015). Secondary alterations, such as diagenetic processes are interpreted by using multiple proxy elements that are related to the same environment. Assuming minimal elemental migration, multiple elements derived from the same source should record a similar trajectory (e.g. Ti and Zr, Ca and Sr, K and Al) (Turner et al., 2016).

The provenance and lithologic makeup of the rock are related. In the Rader Formation the major lithology constituents are transported carbonate and siliciclastic sediments. Nance and Rowe (2015), point out that the distribution of carbonates and siliciclastics has geographic and sequence stratigraphic implications. For example, in their study they found greater carbonate influence at locations more proximal to carbonate shelves, thought to be the source, while greater siliciclastic influence was observed in locations more distal to the carbonate shelves due to proximity to the carbonate shelf (Nance and Rowe, 2015). Both Parra-Galvez et al., (2009) and Nance and Rowe (2015) have suggested sequence stratigraphy plays a significance role to the lithologic makeup of the rock, interpreting siliciclastic dominant intervals and carbonate dominant intervals to represent sea level lowstand and highstand respectively.

Terrigenous or siliclastic input can be analyzed through Si, Ti, and Zr elemental content as well as using elemental ratios such as Si/Al ratio (Crosby, 2015). Ti and Zr are associated with continentally derived sediment (Turner et al., 2015), observed in this study as sands and silts. Turner et al. (2015), elaborated that both Ti and Zr, are also quite immobile, which is important when it comes to elemental proxies. Parra-Galvez

et al., (2009) and Turner et al. (2015), interpreted declining trends in Ti and Zr content as retrogradational successions and increasing trends as progradational successions. Similarly, high siliciclastic input intervals mostly represent times of lowstand deposition (Parra-Galvex et al., 2009 and Nance and Rowe, 2015). Though Si is used as a proxy in the terrigenous sediment proxy suite, it may derive from both detrital and biogenic processes, consequently it must be observed with Al and the Si/Al ratio in order to accurately determine its origin (Sageman and Lyons, 2004; McCullough, 2014).

Clay content was analyzed by looking at SGR and pseudo GR readings generated from XRF measurements in conjunction with K, Al, and Si/Al measurements. Because Al can also be associated with feldspars, another terrigenous clastic material, and thus it cannot be used as the sole proxy for clay content, instead itt must be used in conjunction with other clay proxies, especially K (Treanton, 2014; Crosby, 2015). High SGR and pseudo gamma ray readings may indicate clay rich intervals, but if the reading is due to high U readings rather than high K values, then the reading is most likely attributed to another cause such as sediment anoxia, presence of organic matter, or a highly reduced paleo environment(Zhou, 2014; Crosby, 2015). Nance and Rowe (2015) interpreted clay rich facies to have developed in the after phase of depositional episodes or as an indication that a shift in depo-axes occurred. They further stated that clay dominant facies probably occur during periods of slow background sedimentation in the absence of turbidity-current deposition (Nance and Rowe, 2015).

Following the study conducted by Crosby (2015), P, CA, Sr, Mg, and Mn are analyzed congruently to determine carbonate influence. Turner et al., (2016) use Ca

and Sr to identify carbonate accumulations. The presence of dolomite makes Mg an important element to include in the carbonate elemental proxy suite. Mn was also included in the carbonate suite as it shows covariance with Ca, Sr, and Mg (Crosby, 2015). However, Mn concentration must be interpreted carefully as Mn is highly sensitive to redox conditions (Madhavaraju and Lee, 2009).

To analyze paleoredox conditions a suite containing Mo, V, Co, Ni, Cu, and Mn* was utilized after K.L Pigott (2007) and Crosby (2015). Using certain trace metals as paleoenvironment proxies are useful as they are more soluble under oxidizing conditions and less soluble in reducing conditions, resulting in authigentic enrichments in oxygen-depleted sedimentary facies (Tribovillard et al., 2006). Changes observed in V, Cr, U and Mo can indicate variation in oxygen content (i.e. suboxic, anoxic, or euxinic), insight into basin restriction (i.e. sill development), and the cause of oxygen fluctuation (Smith and Malicse, 2010; Tribovillard et al., 2006). Determining oxygen levels of a paleoenvironement is one of the key components to organic matter preservation. Anoxic and euxinic conditions provide the best preservation environments and occur when demand for oxygen is greater than supply, or, when restricted water column circulation prevents oceanic oxygen renewal (Tribovillard et al., 2006). Mo and V are two of the most commonly used elemental proxies to determine if conditions are oxidizing or reducing due to their immobility and independence from detrital fluxes (Tribovillard et al., 2006; K.L. Pigott et al., 2007). However, Algeo and Rowe (2012) indicate that lack of Mo and V enrichment can also indicate the "basin reservoir effect": where increasing restriction results in low deep-water Mo concentrations as a result of Mo removal to the sediment in excess of resupply from

ocean waters, and not as a result of reducing conditions. Unlike Mo and V, Cr and Co

are susceptible to detrital influences which would make them unsuitable for

paleoenvironment analysis (Tribovillard et al., 2006). Through simple cross plot

analysis between Cr and Co with Ti and Al, it was determined that these elements are

from detrital origin, based on the linear relationship observed. This relationship makes

them unsuited to be used as a paleo redox proxy. Ni and Cu are dominantly delivered to

sediment in association with organometallic complexes (OM), thus when high Ni and

Cu concentrations are observed it can be used as markers of high organic matter input

into the basin (Tribovillard et al., 2006). Additionally, U also serves a good marker for

high organic input, as McManus et al., 2005 and K.L. Pigott et al., (2007) showed a

good correlation between organic carbon rain rate and U abundance. Alfeo and

Maynard (2004) also discovered that high U values are associated with organic-carbon

content anoxic facies.

Tribovillard et al., (2006) insist that Manganese has only limited utility as a

redox proxy. However, others, such as Brumsack (2006) show it to be associated with

suboxic to anoxic conditions as Mn concentrations are elevated in the oxygen—

minimum zone. Additionally Madhavaraju and Lee (2009) indicate that manganese is

highly sensitive to environment redox conditions. Mn has a similar cycling pattern to

Fe (Tribovillard et al., 2006). Madhavaraju and Lee (2009) suggest this relationship

between Fe and Mn across redox boundaries at the sediment water-interface has

implications on paleo redox potential. This relationship is observed in the Mn* proxy

used in Crosby (2015) which normalizes measured Fe and Mn sample readings to

PAAS values of the same elements through: $Mn* = \log [(Mn_{sample} /$

MnPAAS)/(Fe$_{sample}$/Fe$_{PAAS}$)] with lower results indicating more anoxic conditions and

higher values representing more oxic conditions.

4.2.3.1 Rader Ridge Proximal
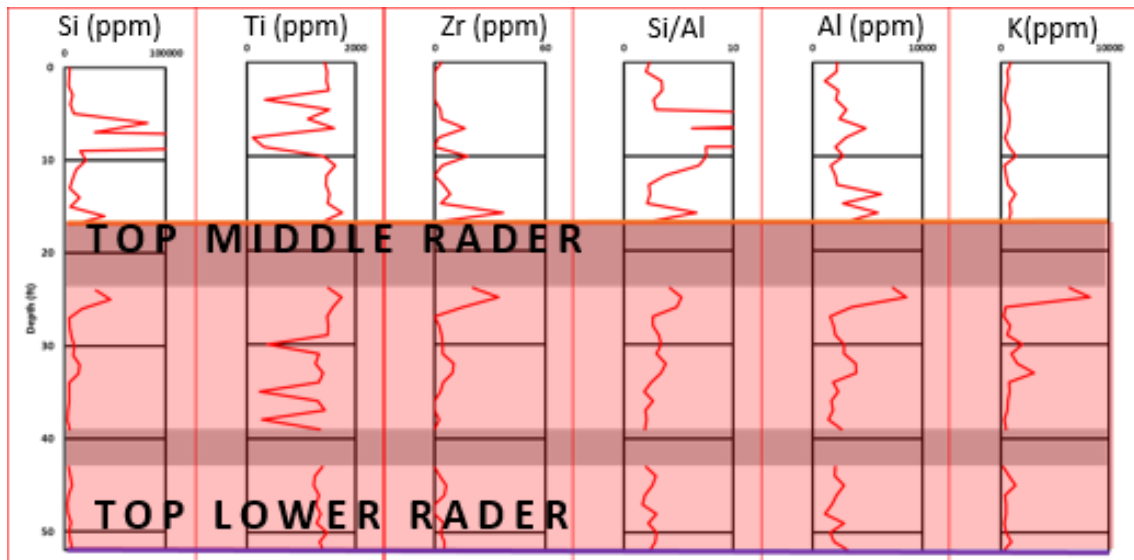
Figure 16: Clastic, clay composition, lowstand proxy elemental logging suite for the Rader Ridge Proximal outcrop displaying Si, Ti, Zr, Si/Al, Al, and K curves from right to left. 52 ft marks the base of the outcrop and 0 ft marks the top of the outcrop. Purple and tan horizontal lines represent the top of the lower Rader unit and top of the middle Rader unit respectively. Horizontal sections of gray fill represent sections of covered outcrop. Highlighted red interval represents interval of elevated clastic/lowstand elemental proxies relative to other interval.

Except for Ti, covariation is observed in Si, Zr, Al, and K proxies shown in the

terrigenous proxy suite in the middle Rader unit. These elemental proxies are

suppressed throughout the middle Rader interval, but all exhibit a spike at 25 ft. Ti is

more elevated relative to the SI, Al, and K throughout the middle Rader interval. The

increasing trend observed at the top of the middle Rader interval is observed across all

terrigenous proxies indicates an increase in detrital terrigenous sediment.

Decreasing trends are observed in Zr, Al and K throughout the upper Rader unit.

Ti also exhibits a slight decreasing trend, but the curve is dominated by two significant

troughs at eight ft and three ft. The trough observed at eight ft corresponds to a sharp

increase in Si and Si/Al, but the second trough observed at three ft does not correlate to

any other proxy. Significant Si peaks are observed from nine ft to five ft. These peaks

are not reciprocated by any other proxy except for Si/Al. This indicates a biogenic or

diagenetic source for the Si increase.
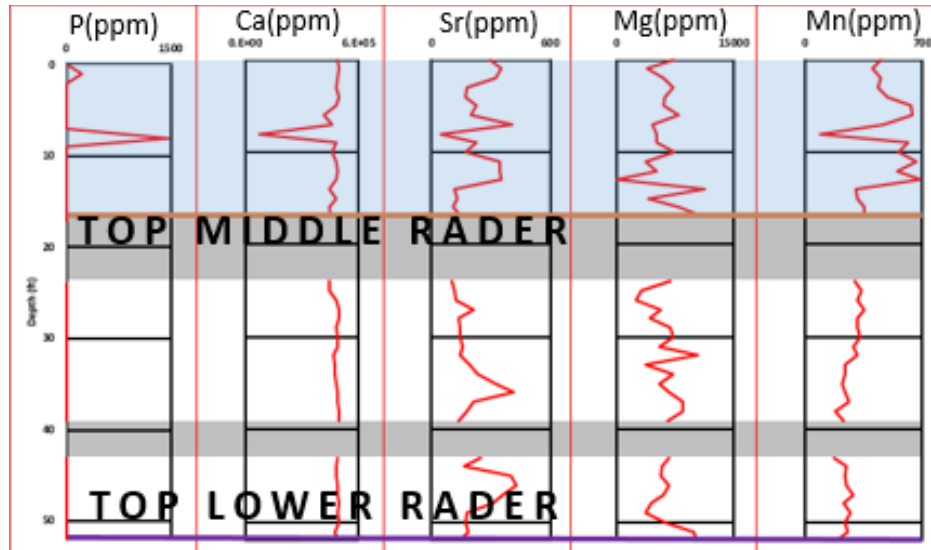
Figure 17: Carbonate, composition, highstand elemental proxy suite for the Rader Ridge Proximal outcrop displaying P, Ca, Sr, Mg, and Mn curves from left to right. 52 ft marks the base of the outcrop and 0 ft marks the top of the outcrop. Purple and tan horizontal lines represent the top of the lower Rader unit and top of the middle Rader unit respectively. Horizontal sections of gray fill represent sections of no outcrop. Highlighted blue interval represents interval of elevated carbonate/highstand elemental proxies relative to other interval.

Strong correlations between carbonate proxies are observed in the middle Rader

unit. Ca is constant and elevated throughout the middle Rader unit which is similarly

observed in the Rader Ridge Distal and Reverse Waterfall measured sections (Figure

17). Sr exhibits an upward decreasing trend from the base of the middle Rader unit,

while Mn shows an increasing trend from the base of the middle Rader unit to the top of

the unit. Conversely, Sr and Mn show upward increasing and upward decreasing trends

respectively within the interpreted correlative interval of 62 ft to the top of the middle

Rader unit in the Rader Distal measured section (Figure 17). Mg exhibits a sharp decrease from the base of the middle Rader unit until 49 ft where this trend is reversed and an increasing trend is observed from 49 ft – 32 ft. From 32 ft up to the top of the middle Rader unit, a decreasing trend is observed in the Mg curve. There is no P observed in the middle Rader unit.

Ca remains elevated at similar levels observed in the middle Rader unit throughout the upper Rader interval, but does experience a sudden trough in the middle of the interval. This sudden trough is also observed in both the Sr and Mn proxies and corresponds to a peak in P as well as in spikes observed in the Si and Si/Al curves from the terrigenous proxy suite. The Sr and Mn curves covariate in the upper Rader interval. Both Sr and Mn exhibit diluted concentrations at the base of the upper Rader unit. This dilution is followed by a sudden increase in concentration right before the large trough observed across the Ca, Sr, and Mn proxies at eight ft.

Constantly elevated Ca concentrations in conjunction with suppressed terrigenous proxies point toward times of highstand during deposition of the middle and upper Rader intervals.
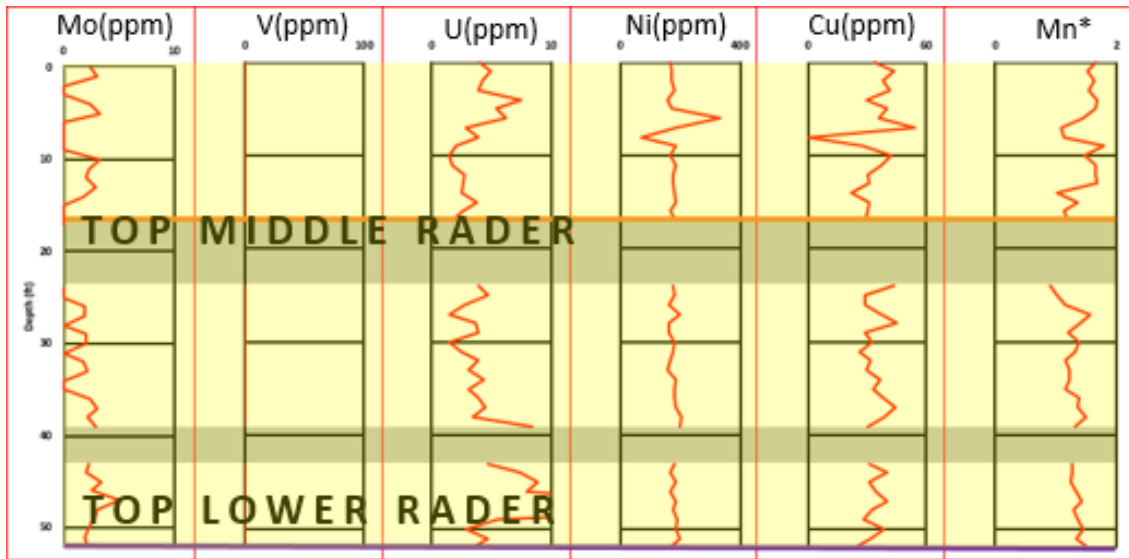
Figure 18: Paleoredox, basin restriction, and paleoenvironment elemental proxy suite for the Rader Ridge Proximal outcrop displaying Mo, V, U, Ni, Cu, and Mn* curves from left to right. 52 ft marks the base of the outcrop and 0 ft marks the top of the outcrop. Purple and tan horizontal lines represent the top of the lower Rader unit and top of the middle Rader unit respectively. Horizontal sections of gray fill represent sections of no outcrop. Highlighted yellow intervals represents intervals of more oxic conditions based on elemental proxies.

Elevated Mo isobserved at the base of the middle Rader interval, followed by a decreasing trend moving upwards towards the base of the upper Rader unit. Good covariation between Mo and U in the middle Rader unit is observed with both showing elevated levels at the base of the interval followed by upward decreasing trends to the top of the interval. Both Ni and Cu show a constant trend throughout the entire middle Rader interval, though Cu is observed to be more variable. Mn* also remains at constant levels throughout the Upper Rader interval, but does exhibit a sharp decrease right below the upper Rader interval indicating relatively oxic conditions during the deposition of the middle Rader interval. However, the decrease in Mn* at the top of the middle Rader interval correlates well to increases observed in terrigenous proxies at this same interval. No V is observed in the middle Rader interval.

62

Mo exhibits slightly higher concentrations in the upper Rader interval than

observed towards the top of the middle Rader unit. U, Cu, and Mn* covariate well,

displaying an overall increasing trend from the base of the upper Rader up to the top of

the measured section. Ni maintains a constant trend throughout the upper Rader

interval except for in the middle of the interval where a large spike and trough are

observed. The sudden and large decrease in concentration correlates to the spikes

observed in Si and Si/Al in the terrigenous proxy suite.   The significant trough

observed at eight ft in Ni, Cu, and Mn matches with peaks observed in the terrigenous

proxy suite.

4.2.3.2 Rader Ridge Distal
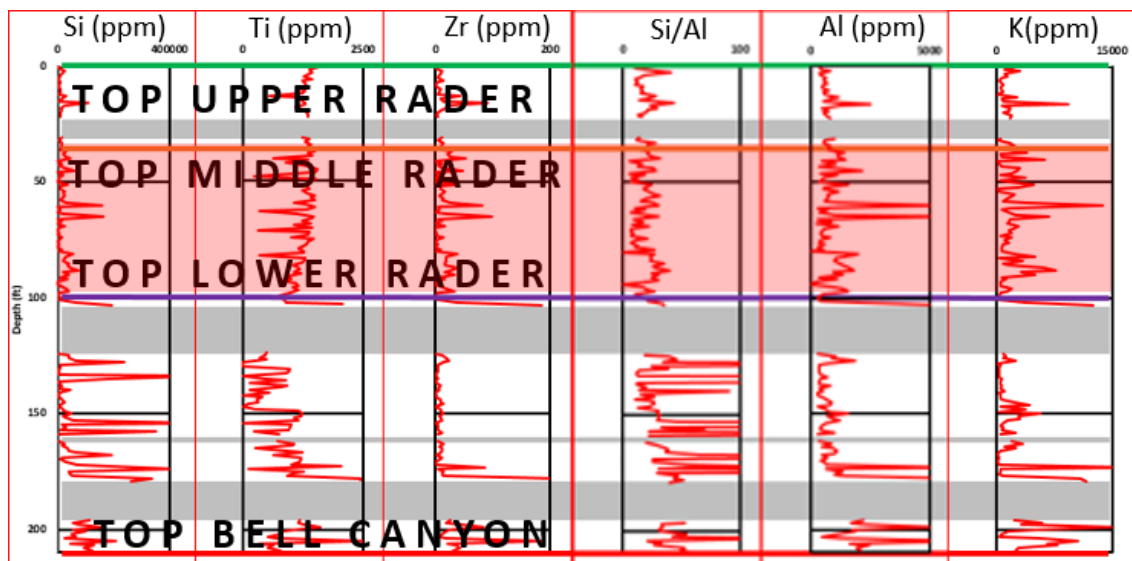
Figure 19: Clastic, clay, composition, lowstand proxy elemental logging suite for the Rader Ridge Distal outcrop displaying Si, Ti, Zr, Si/Al, Al, and K curves from right to left. 209 ft marks the base of the outcrop and 0 ft marks the top of the outcrop. Red, purple, tan and green horizontal lines represent the top of the Bell Canyon formation, top of the lower Rader unit, top of the middle Rader unit, and top of the upper Rader unit respectively. Horizontal sections of gray fill represent sections of no outcrop. Highlighted red interval represents interval of elevated clastic/lowstand elemental proxies relative to other intervals.

The Lower Rader Formation is peppered with massive spikes observed in all the proxies utilized in the suit (Si, Ti, Zr, Si/Al, Al, and K) though these spikes are only observed from 210 ft – 174ft except for Si and Si/Al which have large spikes throughout the entirety of the lower Rader interval. The spikes observed in Si and Si/Al from 174 ft to the top of the lower Rader are not observed in the other proxies. This is indicative of biogenic or diagenetic quartz deposition. All proxies exhibit a general increasing trend from 210ft – 174 ft. Si and Ti have a gradual decreasing trend after 174ft that continues to the base of the middle Rader unit. Zr, Al, and K exhibit a sudden decrease in concentration followed by constant low readings moving upward from 174 ft to the base of the middle Rader unit. All Proxies besides Si/Al show a large spike immediately before the base of the Mega breccia.

Si, Zr, Al, Si/Al, and K all covariate well throughout the middle Rader interval. Si, Zr, Al, and K all show spikes and troughs in the same intervals throughout the middle Rader unit. Si/Al follows the general trends observed in the other proxies, but does not exhibit spikes indicating that all of the terrigenous sediment is detrital. Si, Zr, and Al show similar readings to those observed from170 ft upward to the base of the middle Rader unit. Conversely both Ti, and K are elevated relative to the levels observed from 170 ft to the top of the lower Rader unit.   Ti is the only proxy that does not exhibit covariation to the other terrigenous proxies in the middle Rader interval. Ti exhibits an increasing trend from the base of the middle Rader unit until 50 ft where Ti displays a constant trend moving up for the remainder of the middle Rader interval. Throughout the middle Rader unit, Ti displays sudden, large troughs that are not reciprocated by any other proxy in the suite.

In the upper Rader unit, Si, Zr, Al, and K all exhibit strong covariation, displaying a constant trend moving up from the base of the upper Rader unit to the top of the measured section. Each displays a significant peak at sixteen ft. Si/Al correlates will with Si, Zr, Al, and K. Though Si/Al does exhibit peaks at four ft and sixteen ft, these are of lower magnitude than those observed in the lower Rader unit and are accompanied by increase in the other terrigenous proxies and thus are not interpreted to represent biogenic or diagenetic quartz deposition, but rather a greater increase in detrital Si relative to detrital Al. Ti does not correlate well with the other terrigenous proxies. Ti exhibits higher concentrations than the other terrigenous proxies and shows an increasing trend upward from the base of the upper Rader unit to the top of the measured section. Ti exhibits a trough at thirteen ft that correlates with small peaks observed in the other proxies.
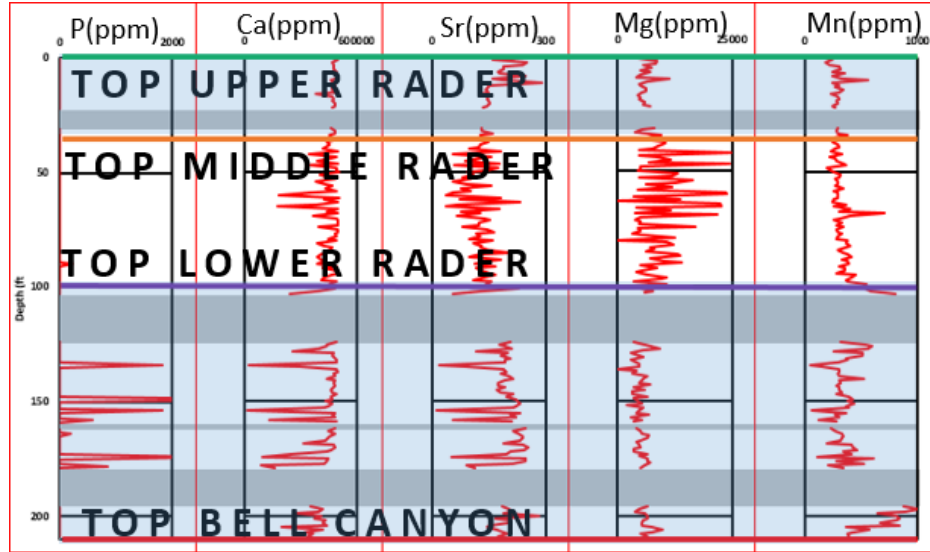
Figure 20: Carbonate, composition, highstand elemental proxy suite for the Rader Ridge Distal outcrop displaying P, Ca, Sr, Mg, and Mn curves from left to right. 209 ft marks the base of the outcrop and 0 ft marks the top of the outcrop. Red, purple, tan and green horizontal lines represent the top of the Bell Canyon formation, top of the lower Rader unit, top of the middle Rader unit, and top of the upper Rader unit respectively. Horizontal sections of gray fill represent sections of no outcrop. Highlighted blue intervals represents intervals of elevated carbonate/highstand elemental proxies relative to other intervals.

Covariation is observed in Ca and Sr throughout the lower Rader unit. Both Ca and Sr exhibit a general increasing trend moving up from the base of the lower Rader interval to 160 ft. In the Sr proxy this trend reverses into a decreasing trend from 170 ft to 124 ft. Ca shows a constant trend for the same interval. Both Ca and Sr are elevated relative to the other proxies, and both exhibit significant troughs at the same depths which match peaks observed in the terrigenous proxies in the lower Rader unit (Figure 19). Mg shows relatively consistent concentrations throughout the entire lower Rader interval. P is only observed as large spikes in the Lower Rader formation, matching troughs observed in Ca and Sr. Mn values are elevated from 210 ft to 195 ft, but fall sharply after the missing outcrop section. A gradual decreasing trend upwards from

180 ft to 159 ft is observed where the trend reverses into an increasing trend from 159 ft until the top of the lower Rader unit. Although the general trends observed in the Mn curve do not correlate with the other proxies, troughs observed in Mn throughout the lower Rader unit match troughs observed in the Ca and Sr curves as well as peaks observed in the P throughout the lower Rader unit.

A single small spike in P is observed at the base of the mega breccia interval at 90 ft. There is no significant change in Ca from the upper portion of the lower Rader formation. Throughout the middle Rader unit, Ca remains generally constant with no increasing or decreasing trends observed, although there are two major and sudden troughs observed in the middle of the interval at 65 ft and 59 ft. Covariation is not observed between Sr and Ca measurements in the middle Rader unit, and exhibits an inverse relationship to Mg in the middle Rader unit. Sr exhibits a general upward decreasing trend from the base of the middle Rader interval followed by a general upward increasing trend from the middle of the interval to the base of the upper Rader interval. Mn is constant in middle Rader interval with a single spike observed at 67 ft that matches spikes in Si, Zr, Al, and K (Figure 20).

No P is observed in the upper Rader Formation. Ca remains at constant concentrations throughout the upper Rader interval. Sr and Mg exhibit inverse trends from the base of the upper Rader interval to the base of the missing outcrop interval, but covariate well from 23 ft to the top of the measured section displaying an upward increasing trend from the base of the upper Rader to the top of the measured section. Mn is relatively constant throughout the interval but does exhibit a spike that matches spikes observed in Mg and Sr at ten ft.
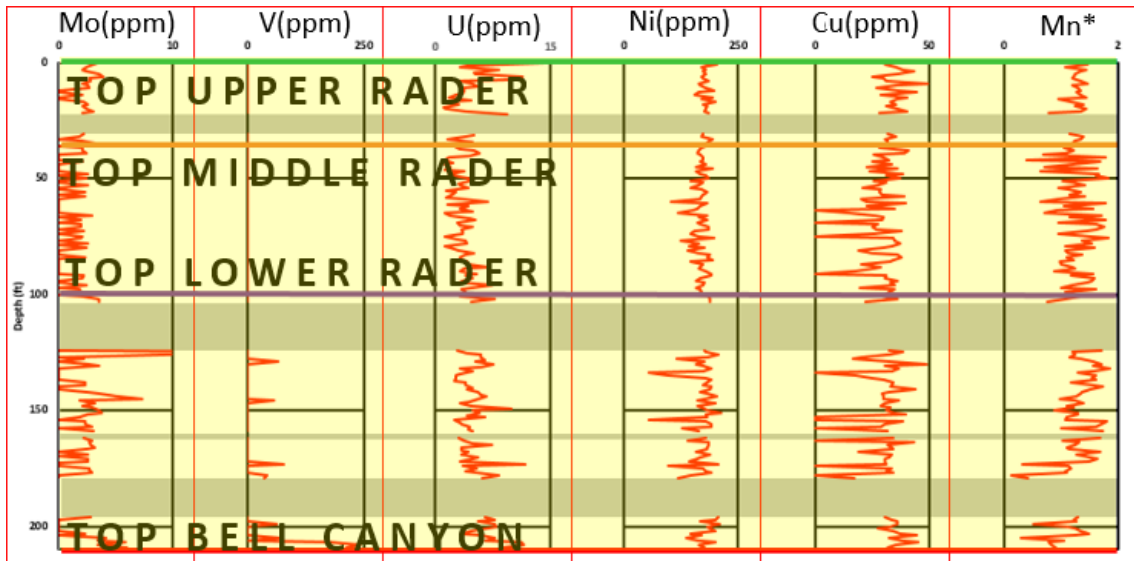
Figure 21: Paleoredox, basin restriction, and paleoenvironment elemental proxy suite for the Rader Ridge Distal outcrop displaying Mo, V, U, Ni, Cu, and Mn* curves from left to right. 209 ft marks the base of the outcrop and 0 ft marks the top of the outcrop. Red, purple, tan and green horizontal lines represent the top of the Bell Canyon formation, top of the lower Rader unit, top of the middle Rader unit, and top of the upper Rader unit respectively. Horizontal sections of gray fill represent sections of no outcrop. Highlighted yellow intervals represents intervals of more oxic conditions based on elemental proxies.

Mo concentrations are generally elevated in the lower Rader unit in comparison the overlying middle Rader. Spikes of V are observed in the Lower Rader Formation which decrease in frequency moving up from the base of the Lower Rader Formation toward the base of the middle Rader unit. U displays an overall decreasing trend moving upwards from the base of the lower Rader unit to the top of the unit. Ni and Cu exhibit covariation, and despite having significant and frequent troughs, show a general trend of consistent values from the base of the lower Rader unit to the top of the interval. Mn* shows an overall increasing trend from the base of the lower Rader interval to the top of the unit, but exhibit consistently lower concentrations from 210 ft to 173 ft than from 173ft to the top of the lower Rader unit. Mn* troughs match elevated levels of V and Mo.

In the middle Rader unit, Mo readings are suppressed relative to those observed in the lower Rader unit showing a constant trend form the base of the middle Rader to the top of the unit. No V is observed in the middle Rader unit. Ni and Cu correlate relatively well showing a constant trend from the base of the mega breccia interval to 62 ft where a slight increasing upward trend is observed from 62 ft to the top of the middle Rader interval. U exhibits an overall upward decreasing trend from the base of the middle Rader interval to the top of the unit. The Mn* curve is variable with frequent peaks and troughs, but exhibits lower values from the base of the unit to 80 ft than observed above 80 ft to the top of the middle Rader interval.

Covariation is observed between Mo and U, exhibiting an overall upward increasing trend in the upper Rader unit. Cu also exhibits an upward increasing trend, and matches the peaks and troughs observed in Mo and U. Ni and Mn* remain constant throughout the upper Rader interval. No V is observed in the upper Rader unit.

4.1.4 Rader Ridge Thin Section Observations
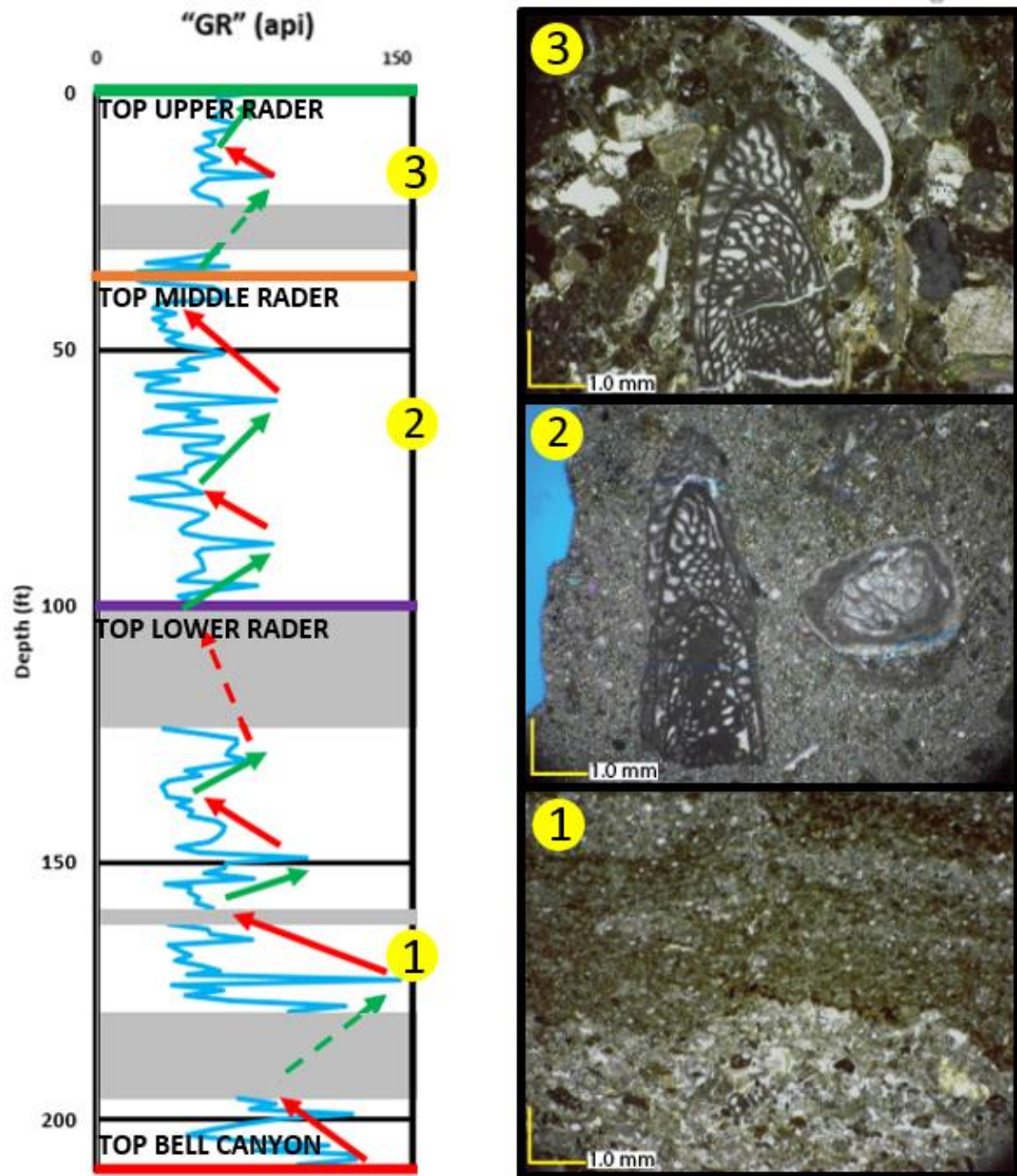
Figure 22: Thin section micro photographs of samples taken from the Rader Ridge Distal measured section. All images are shown in plain polarized light. 1) Sample taken from graded limestone interval of the lower Rader unit. 2) Sample taken from matrix dominated area of mega breccia of the middle Rader interval. 3) Sample taken from base of a graded limestone interval of the upper Rader unit. Arrows represent increase (red) and decrease (green) in process energy.

The thin section taken from a graded limestone unit observed at 160 ft exhibits distinct veritical changes in grain size (Figure 22(1)). The base of the sample is a fossiliferous packstone containing foraminifera, sponge spicules, brachiopod spines, as well as sparse sub angular to sub-rounded calcite grains. The base of the sample is well sorted and fine grained with all constituents less than 1 mm. The lower fossiliferous packstone is topped by a sharp contact with an overlying fossiliferous wackestone. The fossiliferous wackestone contains sponge spicules, brachiopod spines, radiolarians, and abundant pellets. The contact between the packstone and wackestone has significant oil staining. No porosity is observed throughout the thin section.

The thin sections taken from the mega breccia deposit of the middle Rader unit exhibit pellet rich intraclasts, a coated bryozoan, a fractured fusulinids, and a calcarenite matrix (Figure 22(2)). As observed in outcrop, no grading is observed within the thin section micro photographs. The intraclasts are observed to be pellet rich wackestone to packstones with sponge spicules and brachiopod spines making up a small constituency. Fusulinids and bryozoans are observed within intraclasts (Figure 22(2)) as well as within the calcarenite matrix (Figure 22(2)). The fusulinid observed is fractured indicating a very high energy depositional environment (Figure 22(2)). Interestingly, the bryozoan seen in Figure 22 **is** coated with submarine cement.

Thin section taken from 28 ft in the upper Rader unit exhibits a diverse fossil assemblage and though it was taken from the base of a graded limestone unit, the thin section does not show any grading (Figure 22(3)). In the center of the thin section Figure 22(3) is a large fusulinid containing sparry calcite filled fractures. Pellet rich

intraclasts, foraminifera, brachiopod spines, and a trilobite shell fragment are also observed.

4.2 Reverse Waterfall Observations

The Reverse Waterfall outcrop is located 2 km to the northeast of the Rader Ridge locality, and interpreted to be in a more distal portion of the toe of slope (Figure 4). At this location a single section was measured and described in one foot intervals. Additionally XRF measurements were taken every foot and used to generate geochemical proxy suites as well as a total pseudo gamma ray curve. The Reverse Waterfall measured section is a total of 129 ft and contains the top of the Pinery Formation, a covered outcrop section that is interpreted to be Bell Canyon sandstone, the lower Rader unit, and is capped by the middle Rader interval. The Pinery Formation occurs from 129 ft to 105 ft, the Bell Canyon is interpreted to occur from 105 ft to 92 ft, the lower Rader interval occurs from 92 ft to 40 ft, and the Middle Rader unit occurs from 30 ft to the top of the measured section.

4.2.1 Reverse Waterfall Pseudo Total Gamma Ray and Lithology Log
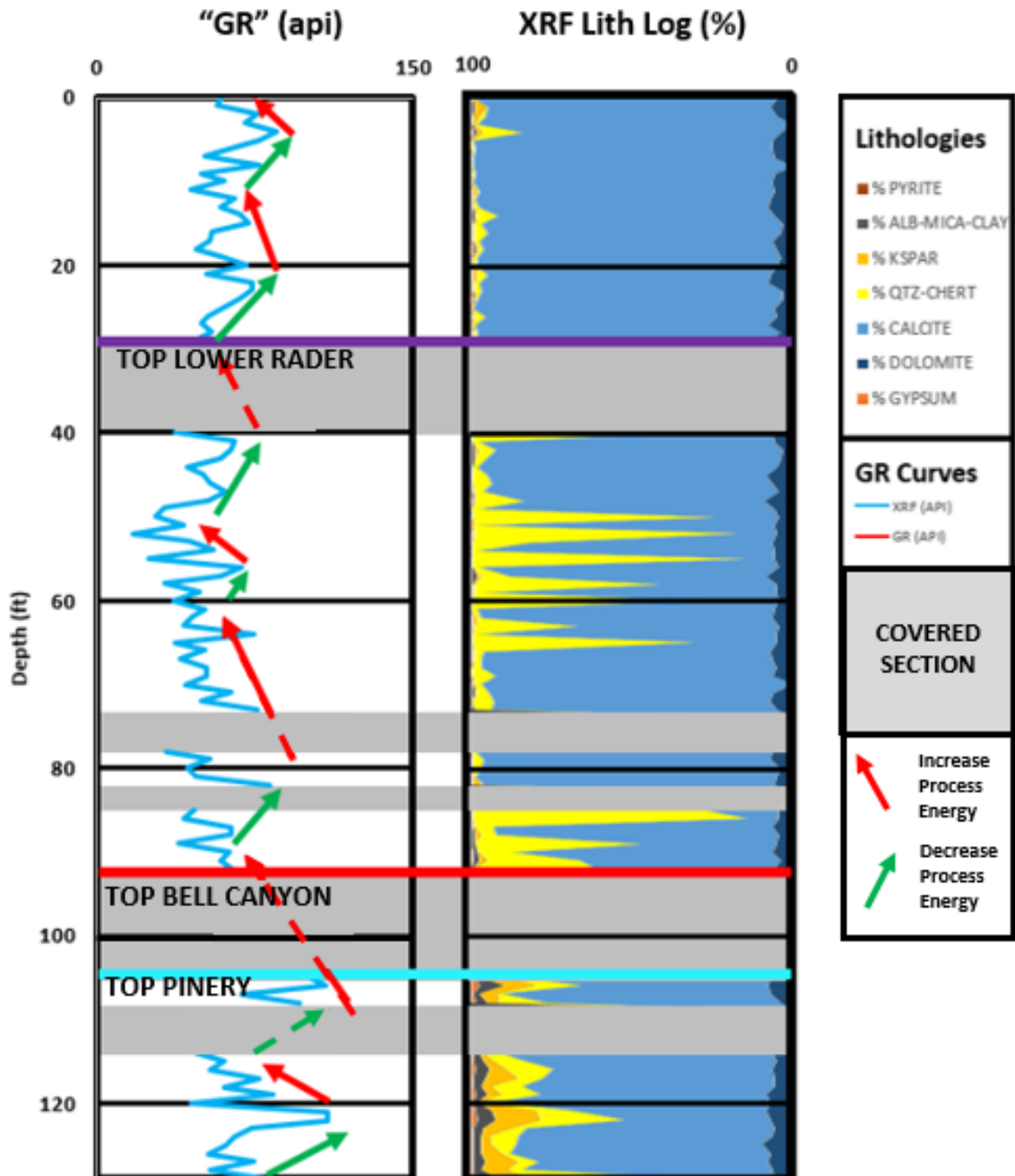
Figure 23: **Total gamma ray generated from XRF measurements (blue curve) shown in API units. Base of Reverse Waterfall measured section is seen at 129 ft and the top of the outcrop is measured at 0 ft. Lithology curve and legend seen on the right including lithology log coloring, GR curve coloring, and process energy trends.**

The Pinery interval observed from 129 ft to 105 ft has elevated clay and kspar content in comparison to the overlying Rader strata in the lithology log (Figure 23). This agrees with field observations that the Pinery interval is dominated by a sandy limestone lithofacies.   The gamma ray curve matches spikes in siliciclastics in the Pinery interval, however, the spikes seem to follow elevations in kspar content more than elevations in quartz content.

Increased quartz content is observed at the base of the lower Rader unit, and decreases moving upward from the base of the lower Rader unit, but kspar and clay content are significantly reduced when compared to the underlying Pinery interval. A dense clustering of isolated spikes of quartz are observed from 66 ft to 49 ft correlating well to field observations of increased chert nodules in this interval. The gamma ray curve in the lower Rader interval has an overall decreasing trend moving upward from the base of the lower Rader unit to 135 ft where a reversal of this trend is observed, and an upward increasing trend occurs to the top of the lower Rader interval. This trend matches the general total pseudo gamma ray trend observed in the lower Rader interval on Rader Ridge (Figure 13 & Figure 14). However, nested cycles of increasing and decreasing total pseudo gamma ray in the lower Rader interval of the reverse waterfall do not match those observed in the lower Rader unit on Rader ridge perfectly (Figure 13 & Figure 14).

The middle Rader unit is the upper most unit observed at the Reverse Waterfall locality. The middle Rader unit is dominated by calcite, and has very limited clay, kspar, and quartz in comparison to the underlying Pinery and lower Rader unit. Within the middle Rader unit the gamma ray exhibits an overall increasing trend moving from

74

the base of the middle Rader interval to the top of the measured section. This trend

does not match the total pseudo gamma ray trends observed in the middle Rader unit in

the Rader Ridge distal and proximal measured sections which exhibit overall upward

decreasing trends (Figure 13 & Figure 14).   There is limited dolomite content

throughout the entire outcrop.

4.2.2 Reverse Waterfall Lithofacies Observations

Similar to the Rader Ridge outcrop, the lithologies observed at the Reverse

Waterfall outcrop are dominantly carbonate. Siliciclastic contributions are minimal in

comparison to the outcrops observed at more distal, basin margin outcrops. The

carbonate lithofacies observed at the Reverse Waterfall locality are very fine grained

massively bedded limestones, very fine grained laminated limestones, normally graded

limestone beds, and a matrix and clast supported carbonate mega breccia deposit. A

mixed carbonate-siliciclastic lithofacies makes up a minor percentage of the observed

rocks. All of the lithofacies observed at the Reverse Waterfall share the same

characteristics described in detail above in the lithofacies section of the Rader Ridge

observation and results (Figure 15). However, only three distinct units of graded

limestone are observed in the intervals 81 ft to 77ft, 69 ft to 66 ft, and 62 ft to 58 ft.

Unlike Rader Ridge, no bioturbated limestone beds are observed at the Reverse

Waterfall locality.

At the Reverse Waterfall, a new lithofacies is observed within the Pinery

Formation at the base of the measured section. This lithofacie is a sandy massively

bedded limestone (Figure 24). This unit is medium bedded ranging in thickness from

four inches to 1 ft. This unit is dark tan to light gray in color. This lithofacies

75

dominates the Pinery formation observed at the Reverse Waterfall locality, and is very

similar in appearance to the massively bedded very fine grained limestone observed at

the Reverse Waterfall and on Rader Ridge, but has a much grittier texture, and in hand

sample fine quartz grains are discernable using a hand lens.

Unlike the overlying Rader deposits, no chert nodules are observed in the Pinery

Formation at the Reverse Waterfall locality. Chert nodules are observed in all

lithofacies except for the mega breccia observed in the middle Rader unit. Similarly,

the chert nodules occur at stratigraphically equivalent positions within beds. These

chert nodule-laden beds occur most frequently at the base of the lower Rader interval,

and in the highest density in the middle of the lower Rader from 66 ft to 49 ft.

**Figure 24: Sandy limestone lithofacies observed in the Pinery Formation at the
Reverse Waterfall outcrop. 1ft rock hammer for scale.**

4.2.3 Reverse Waterfall Morphological Observations

The Reverse Waterfall is was given its name by Pray (1985), but the dramatic

feature for which it is named has been observed and described in many studies (Rigby,

1958; Pray 1985; Lawson, 1989) with Rigby (1958) describing the feature in the most detail. He interpreted the feature to be the result of a breccia-laden submarine slide which eroded significant amounts of basin sediment, forming a steep contact. At this locality a deep ~35 m body of matrix and clast supported mega breccia abuts underlying lower Rader sediment in an apparent steep channel feature (Figure 25).

The Reverse Waterfall channel is filled by the clast and matrix supported mega breccia that makes up the middle Rader unit in the more proximal study locations. Seen at the Reverse Waterfall, as well as on Rader Ridge, the   the contact between the lower and the middle Rader unit is erosive, (Figure 25). No bedding or contacts are observed within the channel fill, indicating that the channel was eroded and filled by one catastrophic event. Slight down warping of sediment beneath the thickest part of the reverse waterfall could be the result of the weight of the deposit. The peculiar geometry of the feature observed in Figure 25 suggests that the channel is observed at an oblique angle to the channel axis.
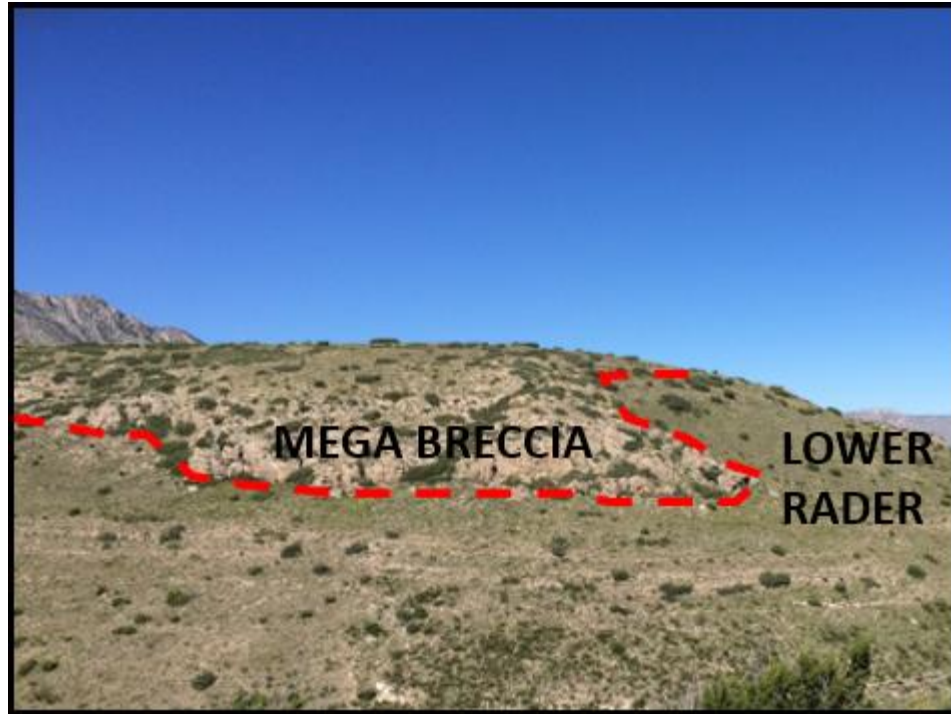
Figure 25: Reverse Waterfall feature named by Pray (1985) outlined by dashed red line. Notice very steep margin on the right side of the feature and the slight plunge of sediments beneath the thickest part of the Reverse Waterfall on the right side of the image. Photo taken of the southeast facing side of the hill upon which the Reverse Waterfall is located.

Additionally, shallow stacked channels are observed in the lower Rader unit at the Reverse waterfall outcrop (Figure 26). These have a width to height ratio of greater than twelve to one. A precise ratio is not given because no channels were observed in which the entire channel body was exposed. These channels are filled with fine grained grainstone and packstone. Additionally, many of these channels contain stratigraphically equivalent chert nodules described above (Figure 26). A faint fining upward trend is observed, however, the overall fine grained nature of the deposits make this difficult to discern.
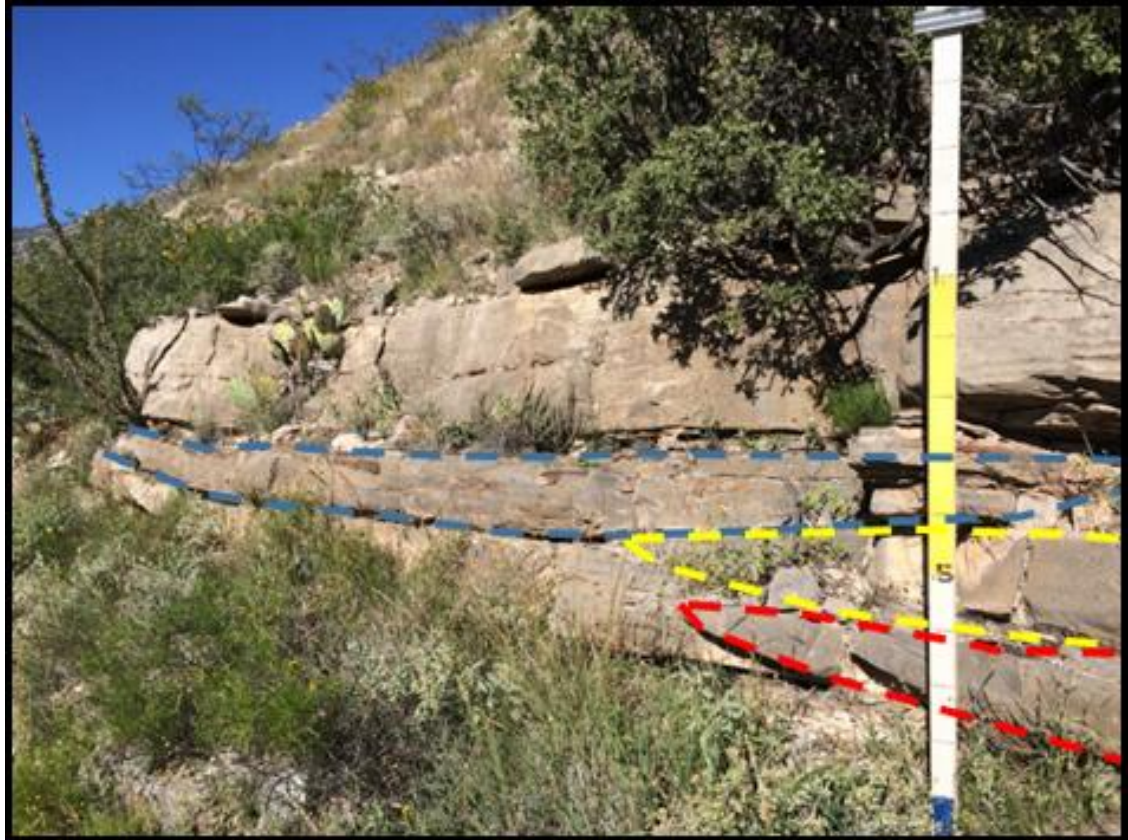
Figure 26: Shallow stacked channels observed in the lower Rader at the Reverse Waterfall Outcrop. Individual channel bodies highlighted by dashed blue, yellow, and red lines. Note aligned chert nodules in the channel body highlighted by the blue dashed line. Jacob staff for scale

4.2.4 Reverse Waterfall Geochemical Proxy Observations
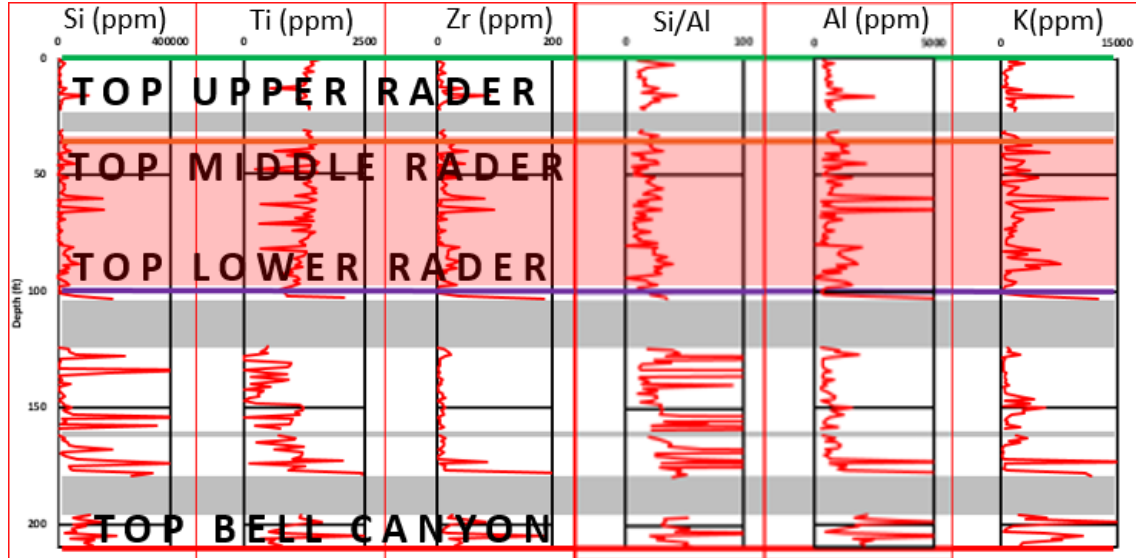
Figure 27: Clastic, clay, composition, lowstand proxy elemental logging suite for the Reverse Waterfall outcrop displaying Si, Ti, Zr, Si/Al, Al, and K curves from right to left. 129 ft marks the base of the outcrop and 0 ft marks the top of the outcrop. Light blue, red, and purple horizontal lines represent the top of the Pinery formation, top of the Bell Canyon formation, and top of the lower Rader unit respectively. Horizontal sections of gray fill represent sections of no outcrop. Highlighted red interval represents interval of elevated clastic/lowstand elemental proxies relative to other intervals.

There is a good covariation observed between Si, Ti, Zr, Al, and K in the Pinery Formation. All of the proxies besides Si/Al show an overall decreasing trend, though this is obscured by several large peak and troughs observed in Al and K in the Pinery Formation. In addition to the overall trend observed, a strong correlation is observed in matching peak and troughs of the elemental proxies, though, they occur at different magnitudes. The constant trend observed in the Si/Al curve from the base of the Pinery to the top of the Pinery indicate that siliciclastic input is generated from detrital sources and not biogenic or diagenetic sources.

In the lower Rader unit, Si and Si/Al exhibit elevated concentrations relative to the underlying Pinery Formation. Both Si and Si/Al curves decrease dramatically and

80

experience suppressed, constant concentrations from 83 ft to 64 ft where a dense cluster of sharp, large magnitude spikes are observed from 66 ft to 49 ft. Si and Si/Al curves again show a depressed, constant trend from 49 ft until 41 ft where a single spike is observed immediately below the top of the lower Rader unit. These spikes and lack of correlation in the other terrigenous proxies indicate that the Si observed is from biogenic, diagenetic, or of locally limited lateral extent. Ti, Zr, Al, and K correlate well and are all attenuated relative to the underlying Pinery Formation and exhibit decreasing trends upwards from the base of the lower Rader unit to 77 ft followed by constant trends to the top of the unit. This matches the profiles of the terrigenous proxies in the lower Rader interval at the Rader Ridge distal measured section, however, Ti is significantly elevated at Rader Ridge in comparison to Ti concentrations observed at the Reverse Waterfall (Figure 16, Figure 19 & Figure 27).

All of the terrigenous proxies exhibit strong covariation in the middle Rader interval. All are attenuated and exhibit constant concentrations from the base of the middle Rader unit to the top of the measured section. The only deviation from this is a slight increase in K at the top of the middle Rader unit. This increase is observed at smaller magnitudes in the other proxies. This matches the trends observed in the terrigenous proxies in the middle Rader interval at the Rader Ridge proximal measured section, however, the terrigenous proxies are more elevated in the middle Rader unit at the Rader Ridge Distal measured section (Figure 16, Figure 19 & Figure 27).
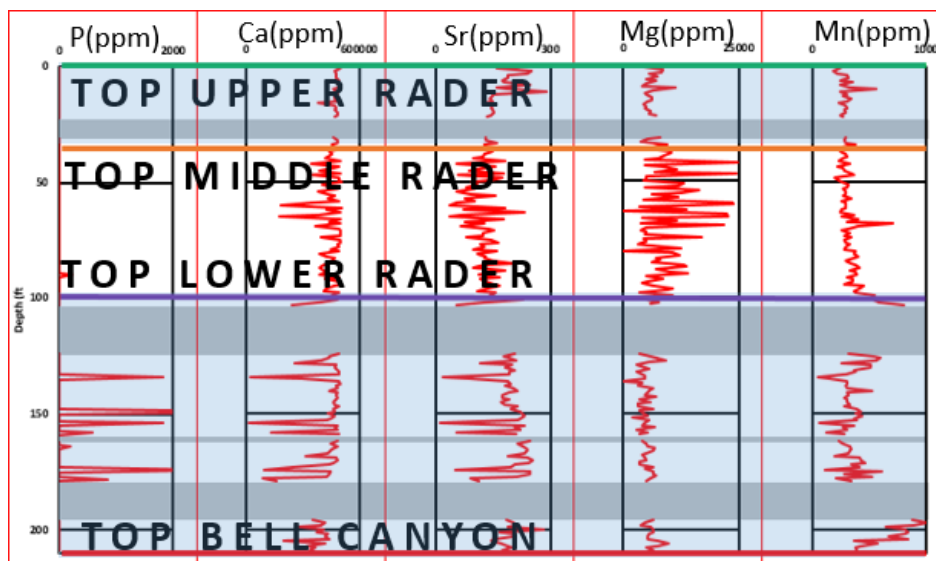
Figure 28: Carbonate, composition, highstand elemental proxy suite for the Reverse Waterfall outcrop displaying P, Ca, Sr, Mg, and Mn curves from left to right. 129 ft marks the base of the outcrop and 0 ft marks the top of the outcrop. Light blue, red, and purple horizontal lines represent the top of the Pinery formation, top of the Bell Canyon formation, and top of the lower Rader unit respectively. Horizontal sections of gray fill represent sections of no outcrop. Highlighted blue intervals represents intervals of elevated carbonate/highstand elemental proxies relative to other intervals.

There is an observed peak in P at the very base of the Pinery Formation interval, but P is not observed in the rest of the Pinery Formation. This peak correlates with spikes observed in the Si, Ti, Zr, Al, and K in the terrigenous proxy suite. Throughout the Pinery both Ca, Sr and Mn exhibit covariation, having an upward increasing trend from the base of the Pinery to the top of the formation. Troughs observed in Ca, Sr, and Mn in the Pinery Formation coincide with peaks observed in the terrigenous proxies (Figure 27). In this interval Mg has a slight decreasing trend which occurs from the base of the Pinery Formation interval towards the top of the interval.

Peaks in P at the base and towards the top of the Lower Rader correspond to observed peaks in Si and Si/Al in the terrigenous proxy suite, however, there are far fewer peaks in P than in Si and Si/Al in the terrigenous proxy suite. Again, Ca, Sr, and

82

Mn exhibit strong covariation, showing an overall upward increasing trend, though Ca exhibits more of a constant trend from the base of the lower Rader unit to the top of the interval. Troughs observed in Ca, Sr, and Mn match spikes observed in Si and Si/Al in the terrigenous proxy suite. This is pronounced from 66ft to 49 ft where a dense cluster of troughs correlate to a dense cluster of peaks observed in Si and Si/Al proxies in the terrigenous suite (Figure 27). Mg shows a slight upward increasing trend from the base of the lower Rader interval to 60 ft where the trend is reversed and a decreasing upward trend is observed from 60 ft to the top of the lower Rader interval. Mg does not exhibit the same troughs as the other carbonate proxies.

P is not observed in the middle Rader unit which is consistent with P concentrations observed in the middle Rader unit at the Rader Ridge measured sections. Unlike the underlying Pinery Formation and lower Rader intervals, Ca, Sr, and Mn do not exhibit strong covariation. Ca concentrations remain elevated and constant throughout the entire middle Rader interval. Sr values are elevated at the base of the middle Rader interval but decrease sharply and exhibit an upward increasing trend from 23 ft to the top of the measured section. Mn observes a decreasing trend form the base of the middle Rader unit until five ft where a sharp increase is observed. Mg values are sporadic and do not show any clear trends.
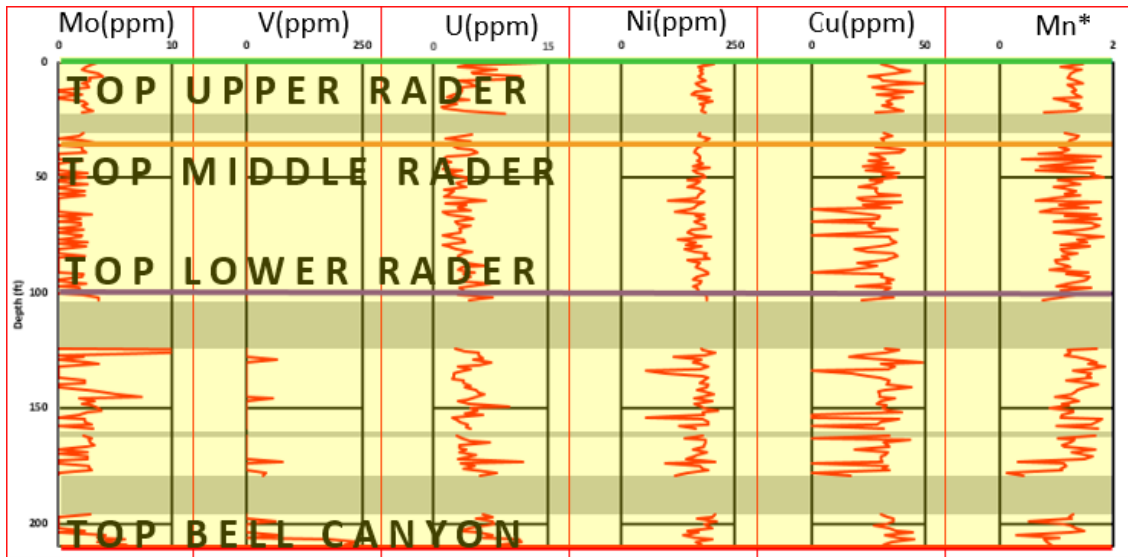
Figure 29: Paleoredox, basin restriction, and paleoenvironment elemental proxy suite for the Reverse Waterfall outcrop displaying Mo, V, U, Ni, Cu, and Mn* curves from left to right. 129 ft marks the base of the outcrop and 0 ft marks the top of the outcrop. Light blue, red, and purple horizontal lines represent the top of the Pinery formation, top of the Bell Canyon formation, and top of the lower Rader unit respectively. Horizontal sections of gray fill represent sections of no outcrop. Highlighted yellow intervals represents intervals of more oxic conditions based on elemental proxies.

Mo is observed as isolated spikes throughout the Pinerey interval which are of the same magnitude as Mo spikes observed above in the lower and middle Rader intervals. V is only observed at the base of the Pinery as two spikes at the very base of the Pinery Formation which match to elevated levels of U, and suppressed values observed in Mn*. U has an overall increasing trend moving from the base of the Pinery interval towards the top of the Formation made up of two increasing trends within the overall upward increasing trend observed from the base of the Pinery to 122 ft and 114 ft to the top of the Pinery Formation. Conversely, Cu has an overall decreasing trend from the base of the Pinery interval moving upwards, but does have a large spike at the top of the Pinery Formation. Ni and Mn* exhibit strong covariation within the Pinery Formation. However, Mn* values are subdued relative to values observed in the

84

overlying lower and middle Rader intervals but exhibit an upward increasing trend from the base of the Pinery to the top of the formation.

Mo shows a slight upward increasing trend from the base of the lower Rader interval to 78 ft, followed by a constant trend moving upward to the top of the lower Rader unit, exhibiting a significant spike at 48 ft which matches a trough in the Mn* proxy. V is only observed in two spikes at the very base of the lower Rader interval. U, Ni, and Cu exhibit covariation in the lower Rader unit. U, Ni, and Cu show a dense clustering of troughs from 66 ft to 49 ft which correspond to the spikes observed in the same interval in Si and Si/Al in the terrigenous proxies and the troughs observed in the same interval in the carbonate proxy suite (Figure 27, Figure 28 & Figure 29). An overall upward increasing trend is observed in the Mn* proxy moving from the base of the Lower Rader to the top of the interval.

Mo is elevated at the base of the middle Rader unit, but has a decreasing upward trend until two ft where a sharp increase is observed at the top middle Rader interval. This large spike observed in Mo at the top of the middle Rader interval matches the single large spike observed in V and a trough observed in Mn*. U, Ni, and Cu do not exhibit covariation in the middle Rader unit. U has variable readings and does not exhibit any general trend. Ni stays relatively constant throughout the middle Rader interval as does Cu except for one distinguish spike seen at eighteen ft that corresponds to a significant trough in the Mn* curve. Mn* values are elevated at the base of the middle Rader interval, but attenuate quickly moving upward from 24 ft to seventeen ft after which an upward increasing trend is observed before experiencing a trough at the top of the middle Rader interval that corresponds to increases in Mo and V.

4.3 Creek Bed Observation

The Creek Bed outcrop is located along a creek bed that is sourced from Bell Spring. This outcrop is located more distally in the study approximately three miles east of the Capitan Reef Slope and 0.25 miles due north of the Road Cut outcrop (Figure 4). This outcrop locality was discovered late in the research process and has only been included in one other study conducted by Lawson (1989). At this study locality, the outcrop was measured and described in one foot intervals, however, due to the late discovery of the outcrop no XRF measurements were taken, but LiDAR scans where acquired and thin sections where made from samples taken from the outcrop. The Creek Bed measured section is a total of 51 ft and contains the Bell Canyon Sandstone Unit One (Table 1), the Middle Rader interval, and the upper Rader unit.

4.3.1 Creek Bed LiDAR Observations
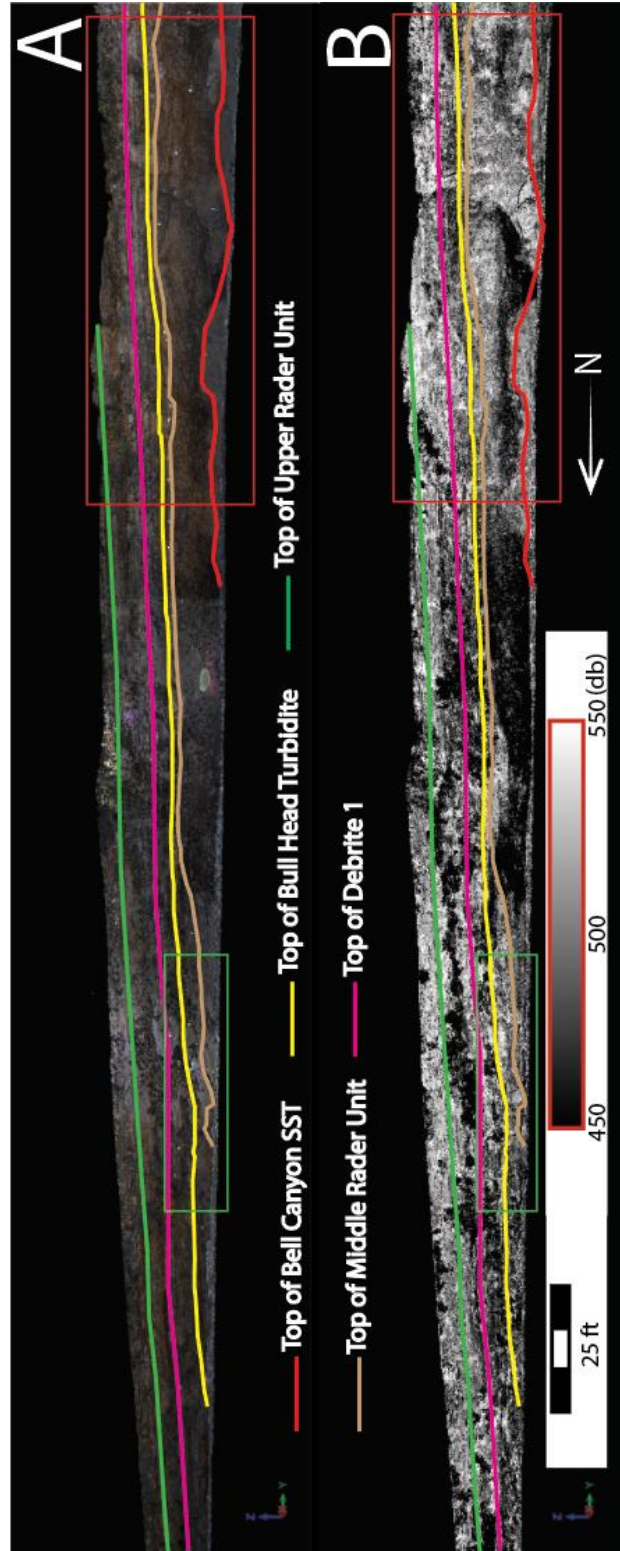
Figure 30: Composite LiDAR image showing the Creek Bed outcrop. Tops of lithologic units interpreted on the LiDAR scans. Red box and green box show sections that will be highlighted below. A) A colored LiDAR scan with pictures overlaid on the LiDAR point cloud data. B) LiDAR image showing reflectance from 450 dB to 550 dB in grayscale.

87

Figure 30 above shows an overview of the Creek Bed outcrop captured in LiDAR scans. All lithologic units are dipping to the north, roughly parallel to the orientation of the Guadalupe Mountains. The top of the Bell Canyon formation (Red Line) and the top of the Mega Conglomerate (Brown Line) are much more undulouse than the top of the Bull Head Turbidite, Debrite One, and top of the Rader Formation which is equivalent to the top of Debrite Two (Table 1). This could reflect a change from more turbulent, erosive flows in the base of the Rader in comparison to deposition of lower flow regimes at the top of the Rader formation. The interval from the top of Debrite One to the top of the Rader Formation thins to the north. Conversely, the Bull Head Turbidite thickens suddenly on the north side of the outcrop where HCS is observed.
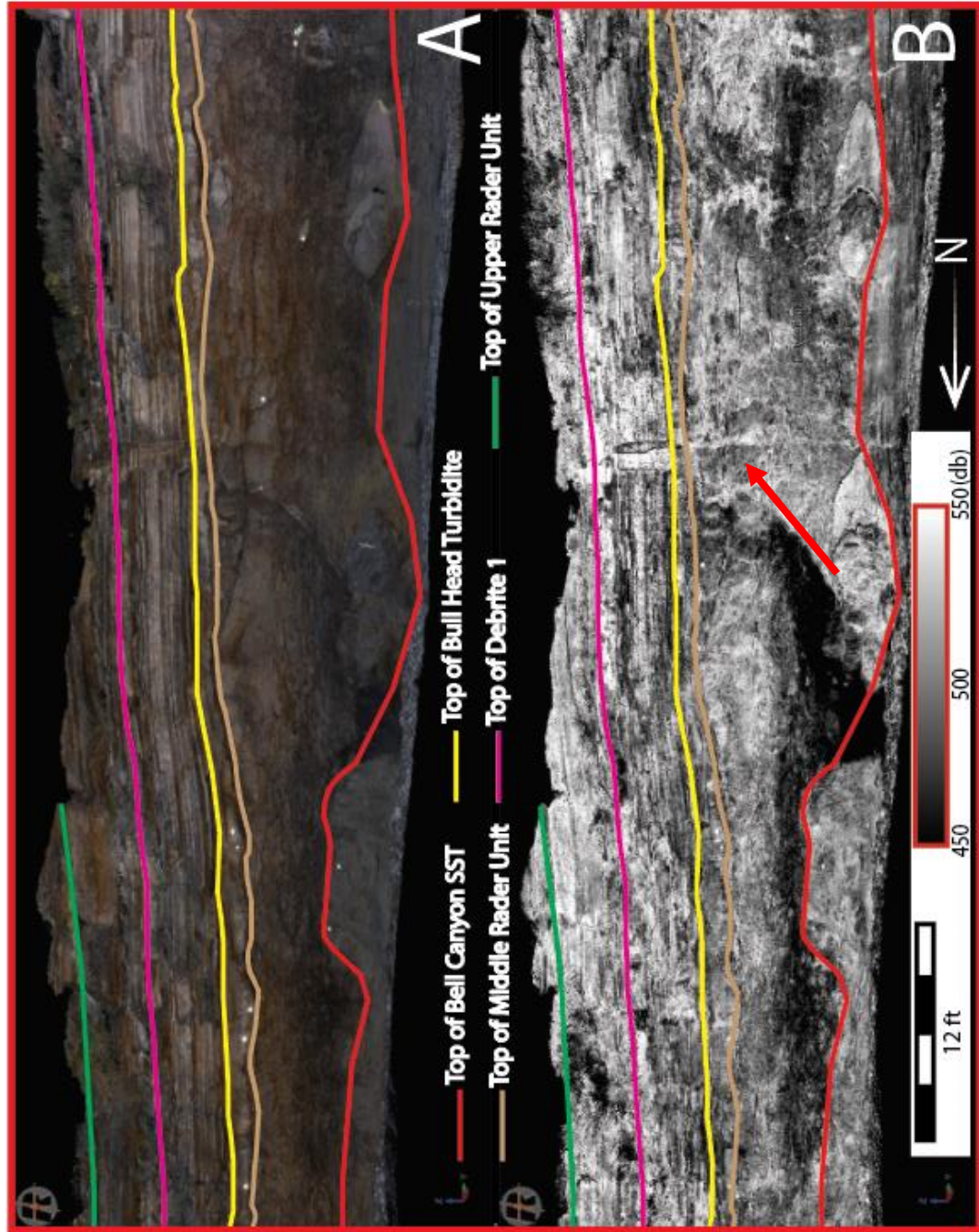
Figure 31: Enhanced LiDAR scans from the right side of the Creek Bed outcrop. Tops of lithologic units interpreted on the LiDAR scans. A) Colored LiDAR scan with photos overlain on top of the LiDAR point cloud data. B) LiDAR scan showing reflectance attribute with a range of 450 dB to 550 dB in grayscale.

Figure 31 shows a zoomed-in portion from the right side of the Creek Bed outcrop. The irregular base of the Mega Conglomerate Unit is clearly seen. Additionally, clearly seen in Figure 31 is the geometry of the sand envelopes which form around the boulder sized intraclasts of the Mega Conglomerate. The deformation caused by the boulder sized conglomerates is observed to be more elongate on the right side of the boulders than on the left side.   A change from massive and chaotically bedded lithologies to thinner, more linearly bedded occurs above the Bull Head Turbidite towards the top of the outcrop. This transition is seen more clearly in the colored LiDAR scan than in the scan displayed in reflectance (Figure 31).

The dark, low dB, reflectance values observed at the base of the Mega Conglomerate Unit do not represent a change in lithology as seen from the colored LiDAR scan. This is a response to lichen covered rocks at the base of the Mega Conglomerate Unit, as reflected in colored LiDAR scan. The LiDAR scan displayed in relfectance does highlight a significant vertical fracture which cuts through the entire outcrop, highlighted by a red arrow in Figure 31B.
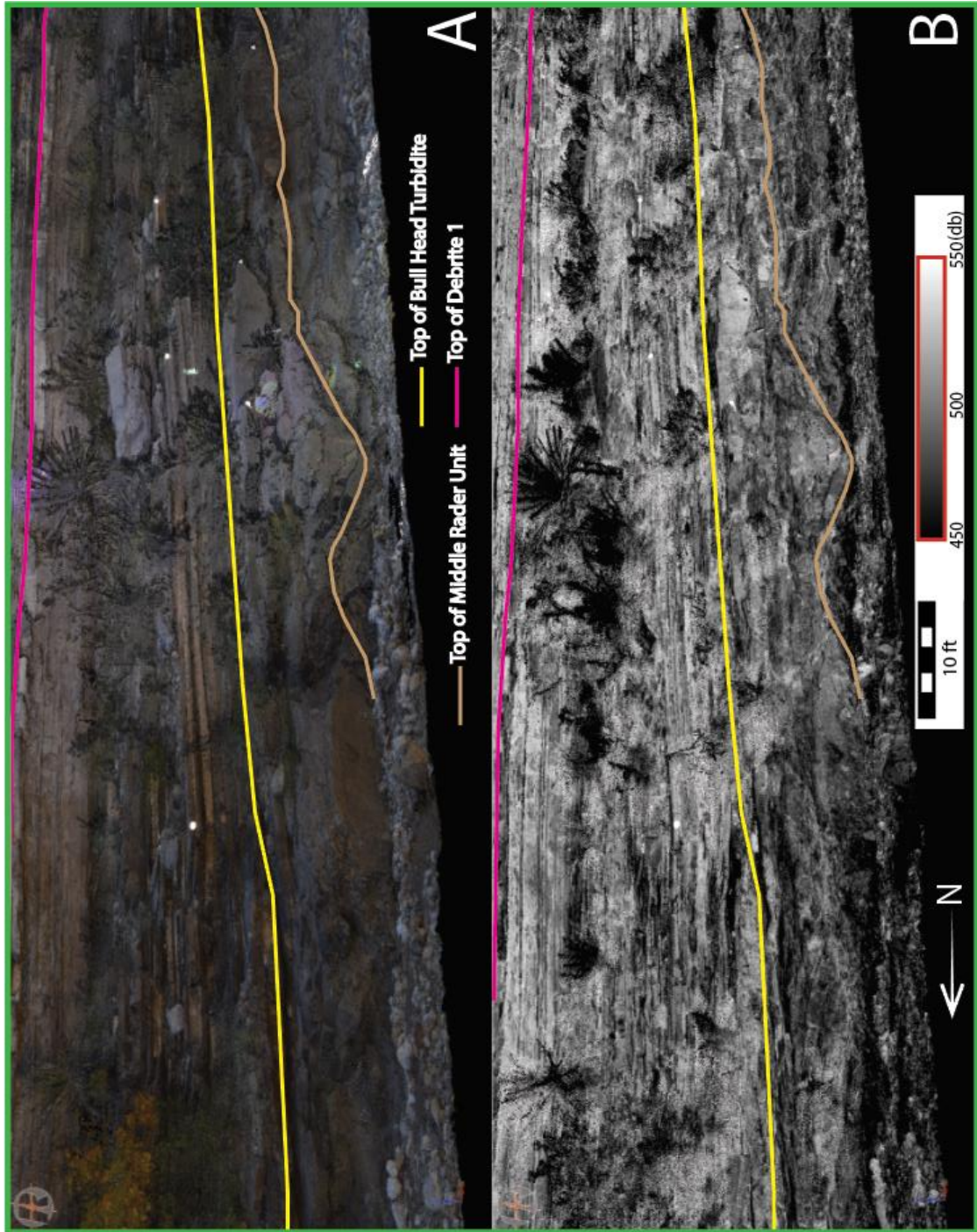
Figure 32: Enhanced LiDAR scans from the left side of the Creek Bed outcrop highlighting the HCS structures described above. Tops of lithologic units interpreted on the LiDAR scans. A) Colored LiDAR scan with photos overlain on top of the LiDAR point cloud data. B) LiDAR scan showing reflectance attribute with a range of 450 dB to 550 dB in grayscale.

Figure 32 shows a zoomed in section of LiDAR data which focuses on the HCS structures seen within the Bull Head Turbidite interval at the Creek Bed outcrop. The HCS structures are easily observed in both the colored LiDAR scan and the scan displayed in reflectance. This is highlighted by the sinusoidal top of the Mega Conglomerate Unit. In contrast, the top of the Bull Head Turbidite and Debrite One intervals are linear.

4.3.2 Creek Bed Lithofacies Observations

The Creek Bed outcrop is interpreted to be in a medial slope margin depositional environment. Here and at the Road Cut outcrop major differences in lithofacies are observed in comparison to the more proximal localities of Rader Ridge and the Reverse Waterfall. The Creek Bed outcrop contains higher siliciclastic content than in the more proximal outcrops. Silicicalstic lithofacies observed at the Creek Bed outcrop include amalgamated parallel laminated sandstone, laminated siltstone, and chaotically bedded sandstone. Additionally a mixed carbonate siliciclastic lithofacies is observed in a matrix-supported Mega Conglomerate Unit made up of massive, boulder sized carbonate intraclasts in a fine grained sand matrix. Carbonate lithofacies observed at the Creek Bed outcrop include normally graded limestone units and very fine grained laminated limestone beds.

Amalgamated, parallel laminated sandstones are the most common siliciclastic lithofacies observed in the distal outcrop locations (Figure 33(1)). These sandstones make up the Bell Canyon formation. These laminated sandstones are tan to grayish orange in color, very fine grained, exhibiting thin to medium bedding with bed thicknesses ranging from 1 inch to 2 ft. The parallel laminations observed are typically

a darker orange color. The laminations are very thin 0.003-0.006 inches thick. The sandstone is made up of predominantly quartz, with minor concentrations of kspar, and has a micitic matrix which fills most of the pore space. The sandstone is very well sorted and contains subrounded to sub angular grains which are ~0.003 inches in diameter.

Laminated siltstones are observed in more proximal localities, but are observed in thicker units and appear more frequently between sandstone and limestone units of the more distal localities. At the Creek Bed outcrop, these laminated siltstone packages are only observed in the upper Rader interval, are 0.5 inches to 6 inches thick, and light to dark gray in color (Figure 33(3)). The presence of laminated siltstone packages is interpreted to represent pelagic to hemipelagic deposition in between carbonate and sandstone units deposited by subaqueous flows. No siltstone is observed in the Bell Canyon Sandstone below the Rader deposits, and no siltstone is observed in the middle Rader deposits.

The chaotically bedded sandstone is unique to the Creek Bed outcrop. This lithofacies is the sandstone matrix of the Mega Conglomerate which makes up most of the middle Rader unit in the distal localities. Stratigraphically, this lithofacies sits directly on top of the parallel laminated sandstone of the Bell Canyon Formation, and beneath the Bull Head Turbidite (Table 1). This sandstone is made up of light gray to light tan sandstone and has random, chaotically-oriented bedding planes that merge and terminate randomly (Figure 33(2)). It is very fine grained, well sorted with no grading patterns observed.

The mixed carbonate-siliciclastic lithofacies observed at the Creek Bed outcrop is a mega conglomerate (Figure 33(6)). This deposit makes up the middle Rader unit in the distal, basin margin localities of the Creek Bed and Road Cut outcrops. This lithofacies is equivalent to the carbonate mega breccia observed in the more proximal localities of Rader Ridge and the Reverse Waterfall outcrops. At the Creek Bed outcrop the mega conglomerate contains massive boulder sized carbonate intraclasts reaching up to thirteen ft in their largest exposed dimension (Figure 33(6)). The limestone boulders in the Creek Bed outcrop are more resistant to weathering than the sandstone which hosts them. While the boulders are not completely exposed, one can infer with relative confidence that the boulders at the Creek Bed outcrop have an overall rounded geometry, and do not exhibit characteristics that would indicate that the boulders have an elongate geometry.

The most distinct graded bedding at the Creek Bed locality is observed in the Bull Head Turbidite unit which has a basal contact with the underlying Mega Conglomerate (Figure 33(4)). In this unit, small cobble to gravel sized clasts are observed at the base of the deposit with distinct graded layers becoming finer moving upwards from the base of the deposit to the top. Graded beds are also observed above the Bull Head Turbidite in the limestone deposits of the upper Rader unit, however, these units are very fine grained and grading is not easily recognized without a hand lens.

Very fine grained, massively bedded limestones are found throughout the upper Rader units at the Creek Bed outcrop (Figure 33(5)). These units are thin to medium bedded with unit thicknesses ranging from 2 inches to 6 inches. Unlike the massively

94

bedded limestones observed in the more proximal localities, here, no chert nodules are

observed. These rocks are very fine grained fossiliferous and peloidal grainstones.
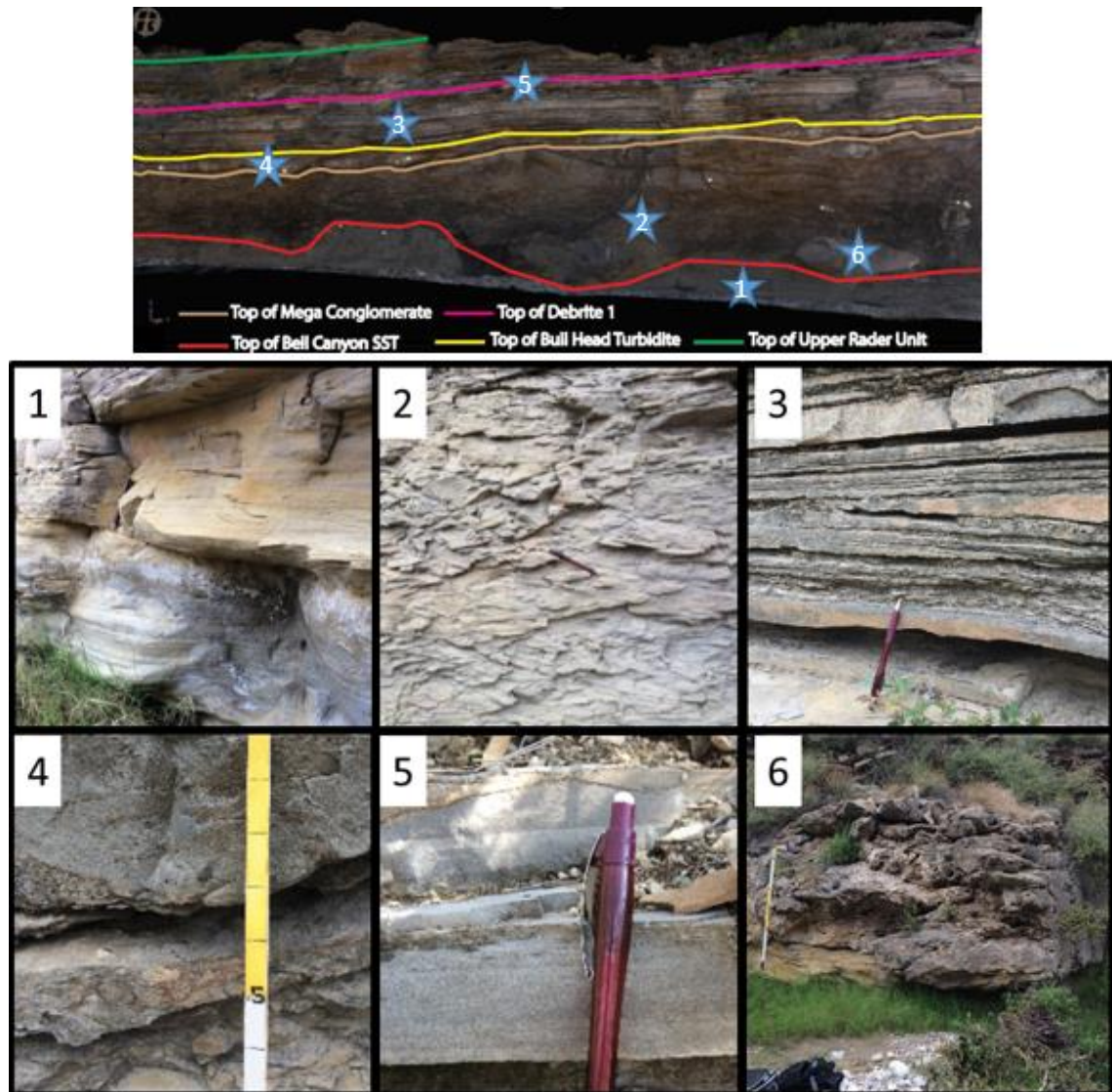
Figure 33: Lithofacies observed at the Creek Bed outcrop. 1) Amalgamated laminated sandstone which makes up the Bell Canyon Sandstone Unit 1. 2) Chaotically bedded sandstone. This constitutes the fine grained sandstone matrix of the Mega Conglomerate Unit. 3) Laminated siltstone observed in the upper Rader interval interbedded between thin limestone beds. 4) Graded limestone beds. These beds often have sharp grain size boundaries.   5) Very fine grained massively bedded limestone observed in the upper Rader interval. 6) Massive, boulder sized intraclast of the Mega Conglomerate Unit which constitutes most of the middle Rader unit.

4.3.3 Creek Bed Morphological Observations

Small scale anticlinal folds are observed in the parallel laminated sandstone lithofacies which comprise the Bell Canyon formation. The homogeneous nature of the lithologies which make up the folded interval indicates that differential compaction is not the cause of the folding. Instead, semi lithified beds are interpreted to slide over intra-bedded planes of weakness, resulting in the low angle anticlinal folds observed in Figure 34A.

Soft sediment deformation is observed only in the mega conglomerate intervals seen in the distal localities of the study. The soft sediment deformation is most notably observed in the Creek Bed outcrop and to a lesser extend in the Road Cut outcrop. At the Creek Bed locality, sandstone strata form "envelope-like" structures around the boulder sized conglomerates (Figure 34B). These "envelope" structures occur on both sides of the boulders in the Creek Bed outcrop, indicating that the movement of the boulders is into the outcrop face, or roughly perpendicular to the Guadalupe Mountain trend. This interpretation is strengthened by the lack of steep folds observed on either side of the boulders that would be expected if the boulder movement was parallel to the outcrop face, as opposed to perpendicular to it. The geometry of the enveloping sandstone also indicates that the boulders slid as they came to rest, and where not rolling immediately before coming to rest. Additionally, at the Creek Bed locality, the mega conglomerate boulder sized carbonate intraclasts are entrained in both the laminated sandstone beneath the boulders, and also the chaotic sandstone which constitutes the matrix of the mega conglomerate at the Creek Bed outcrop. This implies that the boulders were deposited in the same flow as the chaotically bedded sandstone

and that the flow was not dense enough or strong enough to raft the boulders, with the boulders being transported at the base of the flow.

A major channel is interpreted to be present at the Creek Bed outcrop. This feature is interpreted to be filled by the Mega Conglomerate Unit of the middle Rader unit described above (Figure 34C), and be topped by the Bull Head Turbidite (Table 1). The basal contact of the channel is the laminated sandstone of the Bell Canyon Formation. This channel is interpreted to have eroded the lower Rader unit which is observed in more proximal localities, but not at the Creek Bed or Road Cut outcrops. The dimensions of the channel are not known as the channel margins are not exposed at the Creek Bed outcrop.
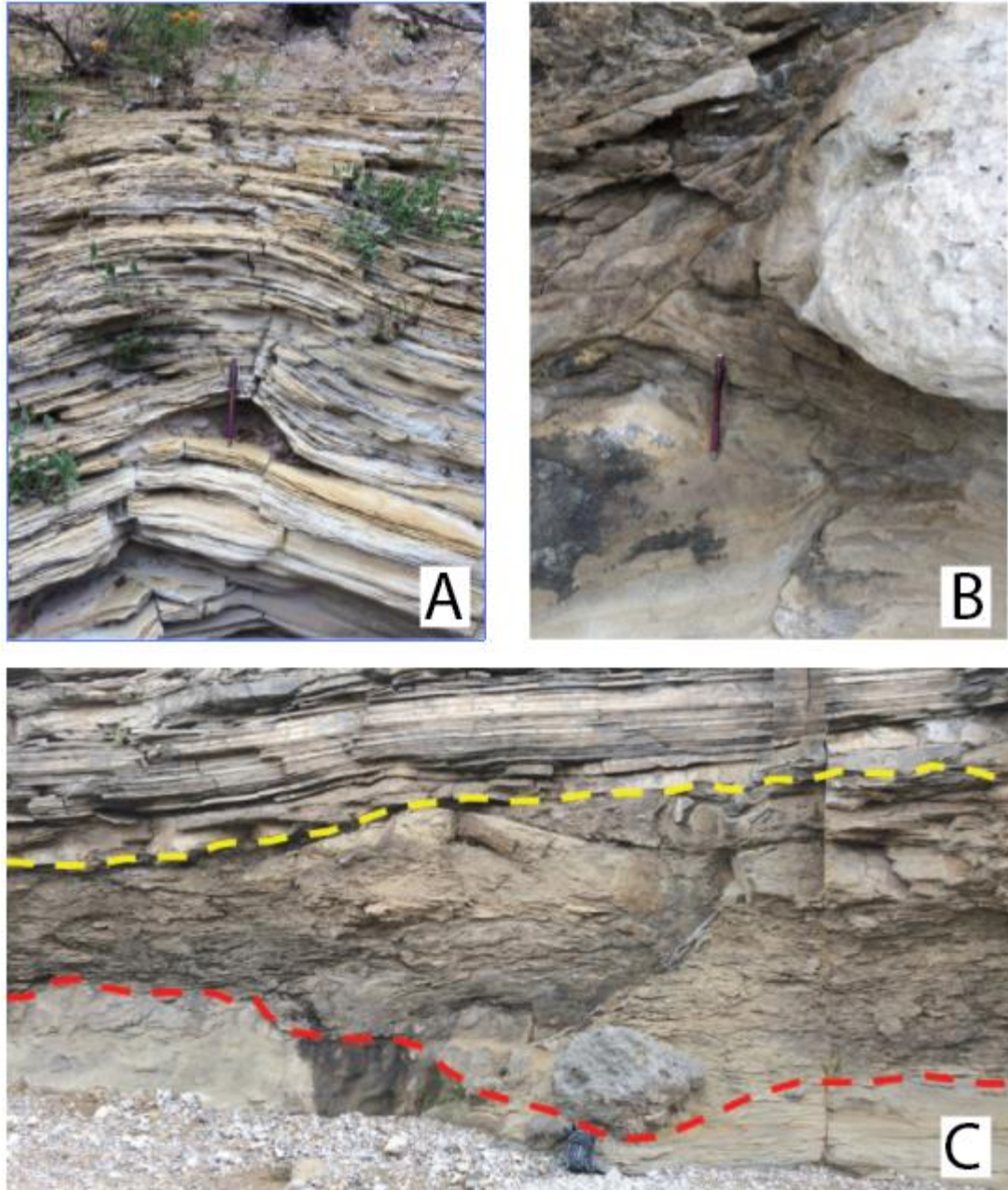
Figure 34: Major geomorphological features observed at the Creek Bed outcrop. A) Small anticlinal folding observed in the parallel laminated sandstone which makes up the Bell Canyon Sandstone Unit 1. B) Soft sediment deformation in the sandstone matrix forming "envelopes" around the boulder sized carbonate intraclasts. C) Interpreted channel filled with the Mega Conglomerate lithofacies of the middle Rader interval. Basal contact (red dashed line) is the parallel laminated Bell Canyon Sandstone. Upper contact (yellow dashed line) is the Bull Head Turbidite of the middle Rader interval.

Topping the interpreted channel is the Bull Head Turbidite. Previous studies (Lawson, 1989) interpreted the Bull Head Turbidite to be an erosive turbidite with an undulous base. However, there is a cyclicity observed to this feature in the Creek Bed outcrop which gives it the appearance of a swale-and-fill structure with repetitive amplitude and wavelength features. This feature is interpreted to be hummocky cross stratification (HCS). The HCS exhibits wave amplitudes of 1.2 ft to 1.5 ft and wave lengths of 7.5 ft, and exhibit a fining upward trend, with coarser, gravel sized clasts observed at the base grading into fine grained packstone. The HCS observed has an apparent repeating nature moving upward, however, the stratigraphically higher HCS structures are not as continuous as the basal feature observed in Figure 35. These stacked HCS intervals are separated by a thin layer of silt and mud. The stratigraphically higher intervals have similar amplitudes measured at 1 ft, and wavelength of 7 ft. Additionally, the HCS observed at the top of the interval exhibits a planar top, in contrast to the basal interval which exhibits a more sinusoidal top (Figure 35). Above the HCS features observed in the Bull Head Turbidite, are the finer grained limestone, siltstone, and sandstone units of the upper Rader interval.

Figure 35: Hummocky cross stratification (HCS) observed at the Creek Bed outcrop in the Bull Head Turbidite. Basal HCS structures have amplitudes of 1.2 ft to 1.5 ft and wave lengths of 7.5 ft (red dashed line). Upper HCS structures have amplitude of 1 ft and wave lengths of 7 ft. Note the planar top of the upper HCS unit (green dashed line). 6 inch white ruler for scale.

4.3.4 Creek Bed Thin Section Obsrvations
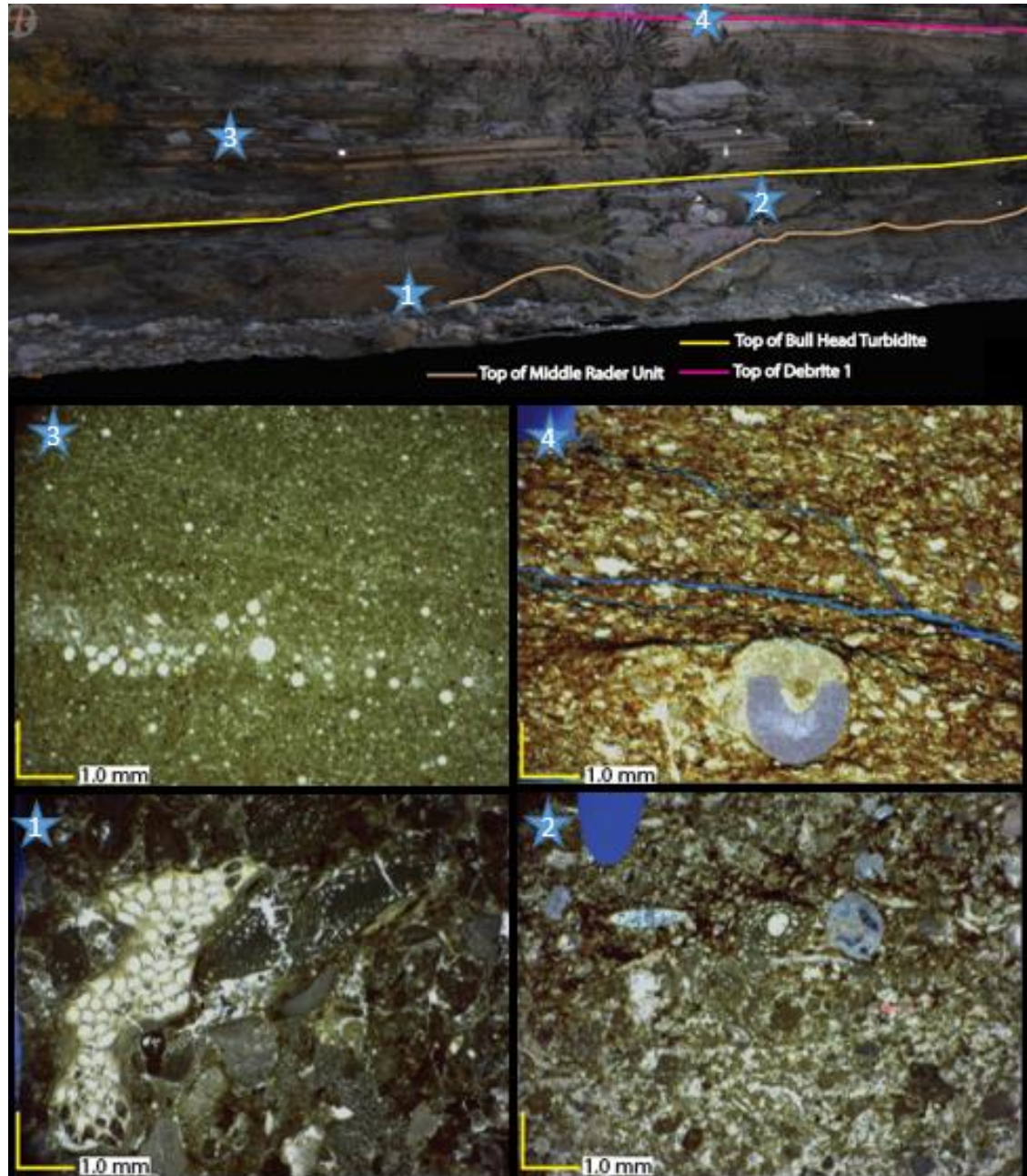
Figure 36: Thin section micro photographs of samples taken from the Creek Bed outcrop location. All micro photographs are taken in plain polarized light. 1) Sample taken from the base of the Bull Head Turbidite. 2) Sample Taken from the top of the Bull Head Turbidite. 3) Sample taken from thin limestone bed located within the Interbedded Carbonate and Sandstone unit 1. 4) Sample taken from DDebrite 1.

Figure 36(1) & (2) show thin sections taken from the base and top of the Bull Head Turbidite, interval respectively (Table 1). The sample taken from the base of the Bull Head Turbidite shows a coarser, less sorted packstone, containing a more diverse fossil and intraclast assemblage. Intraclasts observed at the base of the Bull Head Turbidite are angular to sub-rounded pelloidal and micritic clasts with *girvanella algea*. These clasts range in size from 0.003 inches to 1 inch. Large fossils are also observed including large bryozoans and fusulinids. The fusulinid observed in Figure 36(1) is heavily fractured indicting high depositional energy. Conversely, the thin section taken from the top of the Bull Head Turbidite (Figure 36(2)) is a much finer grained, well sorted packstone. The sample is dominated by oriented sponge spicules and foraminifera with significant sparry calcite replacement observed. Additionally, in contrast to the bottom of the Bull Head Turbidite, angular to sub-rounded quartz grains are observed as well as oil staining.

The sample taken from a limestone bed of the Interbedded Limestone and Sandstone Unit One (Table 1) is a faintly laminated fossiliferous micritic mudstone. There is a linearly oriented interval in the middle of Figure 36(3) of densely clustered calcipheres which have sparry calcite replacement (Figure 36(3)). Fossils observed in the sample are calcispheres, foraminifera, radiolarian, and sponge spicules. Additionally, sparse organics are observed, though no oil staining is seen.

The sample taken from Debrite One (Table 1) is a grain rich wackestone, and the entire sample appears to be oil stained. There are horizontally oriented fractures observed throughout the sample filled with black oil. Despite the ubiquitous oil staining, no porosity is observed. Calcite grains less than 0.003 inches that are angular

to sub rounded make up the majority of clasts, though some small pelloidal intraclasts are observed. A single large crinoid stem is observed as a part of an intraclast toward the base of Figure 36(4). The sample is medium sorted and no apparent grading is observed. Besides the large crinoid stem, foraminifera, brachiopod spines, sponge spicules, and *girvanella algae* are observed as minor constituents.

4.4 Road Cut Observations and Results

The Road Cut outcrop is the most distal location observed in this study. It is 3.5 miles east of the Capitan Reef Slope and .25 miles due south of the Creek Bed outcrop (Figure 4). This is the most commonly observed outcrop of the Rader formation due to its location along US HWY 62 just south of the entrance to Mckittrick Canyon. The outcrop was measured and described in 1 ft intervals. At this locality XRF and SGR measurements were taken in a grid fashion at the Road Cut outcrop as described in the methods section. The Road Cut outcrop is a total of 60 ft and contains the Pinery Formation, Bell Canyon Sandstone Unit One, Middle Rader unit, upper Rader unit, and Bell Canyon Sandstone Unit Two. The Pinery Formation occurs from 60 ft to 56 ft, the Bell Canyon Sandstone Unit One occurs from 56 ft to 41 ft, the middle Rader unit occurs from 41 ft to 28 ft, the upper Rader interval occurs from 28ft to eleven ft and the Bell Canyon Sandstone Unit Two occurs from eleven ft to the top of the measured section.

4.4.1 Road Cut LiDAR Observations
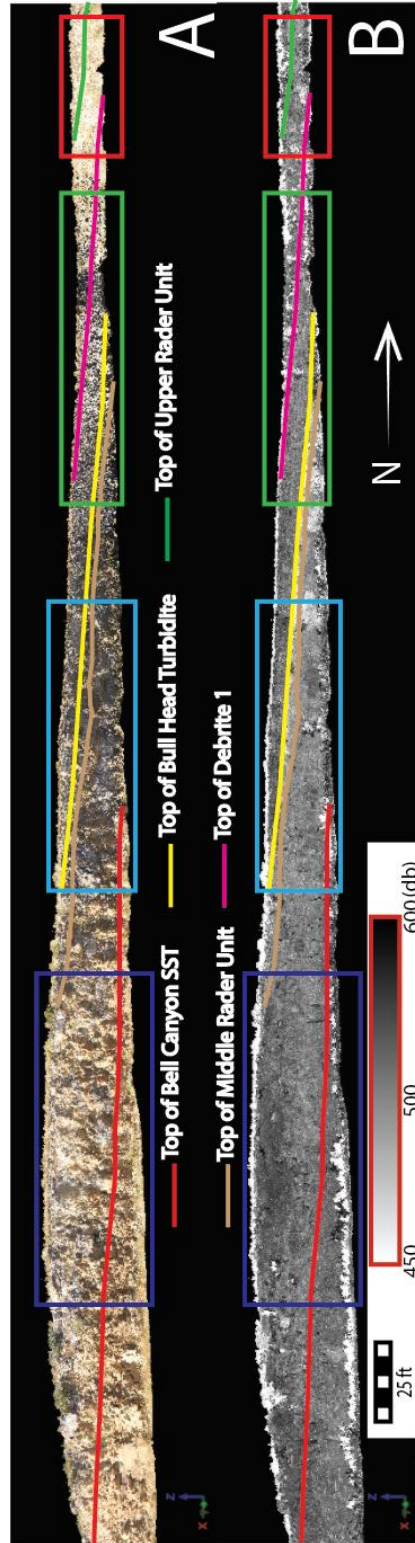
Figure 37: Composite LiDAR image showing the Road Cut outcrop. Tops of lithologic units interpreted on the LiDAR scans. Colored boxes indicate sections that will be zoomed in on below. A) Colored LiDAR scan with pictures overlaid on the LiDAR point cloud data. B) LiDAR image showing reflectance from 450 dB to 600 dB in grayscale.

Figure 37 above displays an overview of the LiDAR scan taken at the Road Cut outcrop. All of the beds interpreted on the scans are dipping to the north, but the dip observed in the top of the Bell Canyon Sandstone Unit One is slightly less than the dips observed in the tops of lithologic units making up the Rader formation. This difference in dip is highlighted in Figure 45.

As observed in the LiDAR results for the Creek Bed outcrop, the top of the Mega Conglomerate Unit is less linear than those of the Bull Head Turbidite, Debrite One, and Debrite Two lithologic units. However, the top of the Bell Canyon Sandstone Unit One is linear where the top of the Bell Canyon Sandstone Unit One observed in the Creek Bed is much more undulous and irregular.
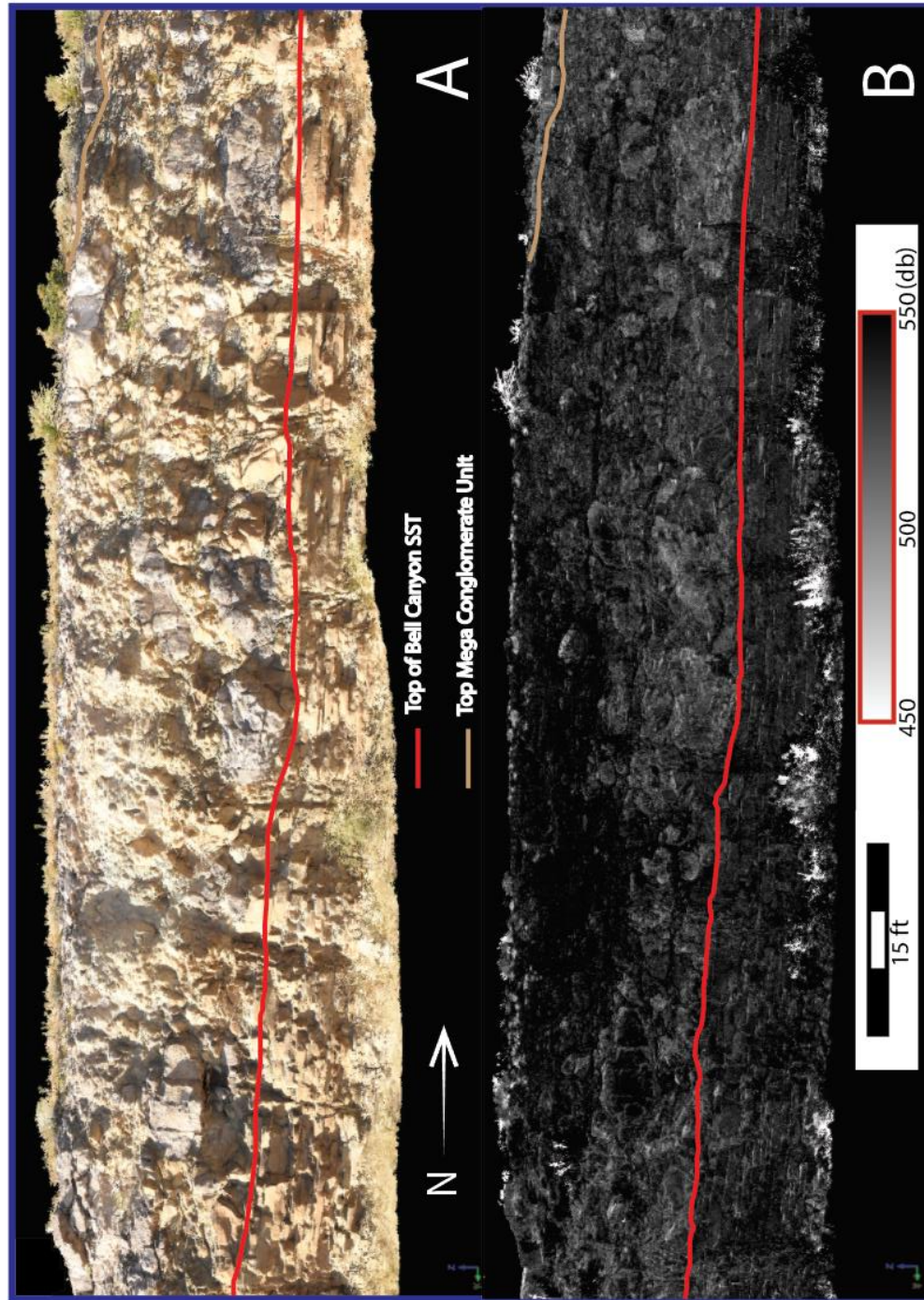
Figure 38: Zoomed in LiDAR scan from the left side of the Road Cut outcrop showing the Bell Canyon Formation, Mega Conglomerate Unit, and a small portion of the Bull Head Turbidite in the upper left corner of the image. A) Colored LiDAR scan with photos overlain on top of the LiDAR point cloud data. B) LiDAR scan showing reflectance attribute with a range of 450 dB to 550 dB in grayscale.

Zoomed in section of the Road Cut LiDAR scan on the left side of the Road Cut outcrop, highlighted by a purple box in Figure 37. This section highlights the Bell Canyon Sandstone Unit One and Mega Conglomerate lithologic units, and also shows a small portion of the Bull Head Turbidite in the top right corner of Figure 38.

The LiDAR image using reflectance attribute accentuates the parallel bedding geometries observed in the Bell Canyon Sandstone Unit One. However, it gives a mixed reflectance values for the large, boulder sized carbonate intraclasts observed in the Mega Conglomerate Unit. However, when viewed in conjunction with the LiDAR scan with photos overlaid, the geometries of the carbonate boulders are able to be identified. In contrast to the Mega Conglomerate Unit viewed at the Creek Bed outcrop, the carbonate boulders have much denser spacing. Additionally, the boulders are not exclusively located along the bottom of the Mega Conglomerate Unit, but are distributed throughout the lithologic unit, and do not exhibit the same sand enveloping seen at the Creek Bed outcrop.
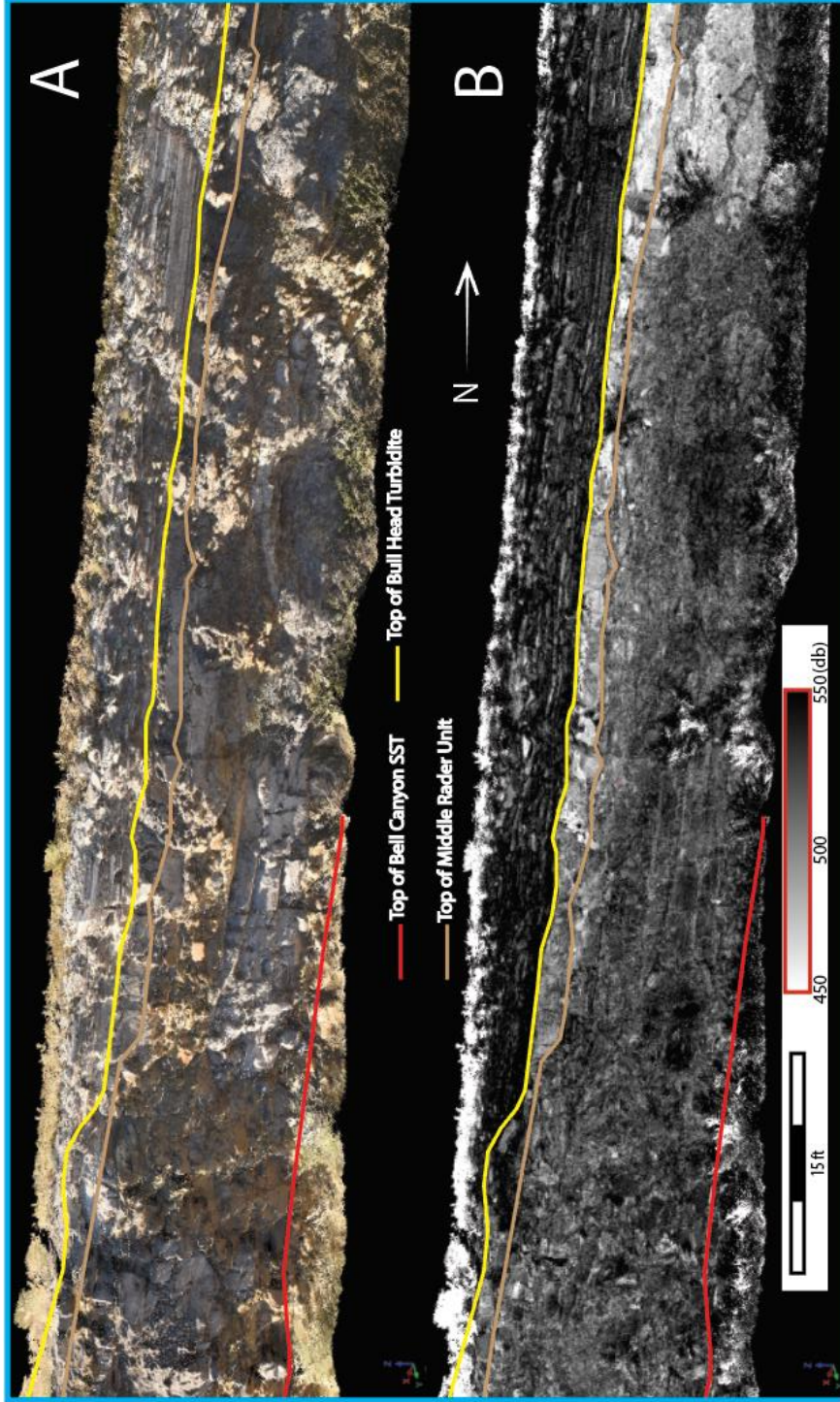
Figure 39: Zoomed in LiDAR scan from the middle-left side of the outcrop (blue box in overview image) showing the top of the Bell Canyon Sandstone, Mega Conglomerate Unit, Bull Head Turbidite, and the Interbedded Limestone and Sandstone Unit 1. A) Colored LiDAR scan with photos overlain on top of the LiDAR point cloud data. B) LiDAR scan showing reflectance attribute with a range of 450 dB to 550 dB in grayscale.

108

Zoomed in section of the Road Cut LiDAR scan on the middle left side of the Road Cut outcrop is highlighted by a light blue box in Figure 37. Also shown is the Bull Head Turbidite and the Interbedded Limestone and Sandstone Interval which overlays the Bull Head Turbidite. Figure 39 shows the close proximity of the boulder sized carbonate intraclasts of the Mega Conglomerate and the overlying Bull Head Turbidite, with the two becoming difficult to differentiate. This proximity is not reciprocated in the Creek Bed outcrop, where the boulder sized conglomerates are exclusively observed at the base of the Mega Conglomerate Unit.

Again, as observed in Figure 38 the boulder geometries are very difficult to identify in the LiDAR image displayed in reflectance. In contrast the Bull Head Turbidite is highlighted in the reflectance attribute, and is easily differentiated from the overlying thin beds of the Interbedded Limestone and Sandstone Unit One. This contact is much more obvious in the scan displayed in reflectance than the scan overlaid with photographs of the outcrop. This stark contrast between the Bull Head Turbidite and overlying Interbedded Limestone and Sandstone Unit One is not observed in the Creek Bed outcrop scans. Further, the reflectance attributes accentuates the individual layers of the Interbedded Limestone and Sandstone Unit One, though these beds are also well displayed in the scan with photographs overlain.
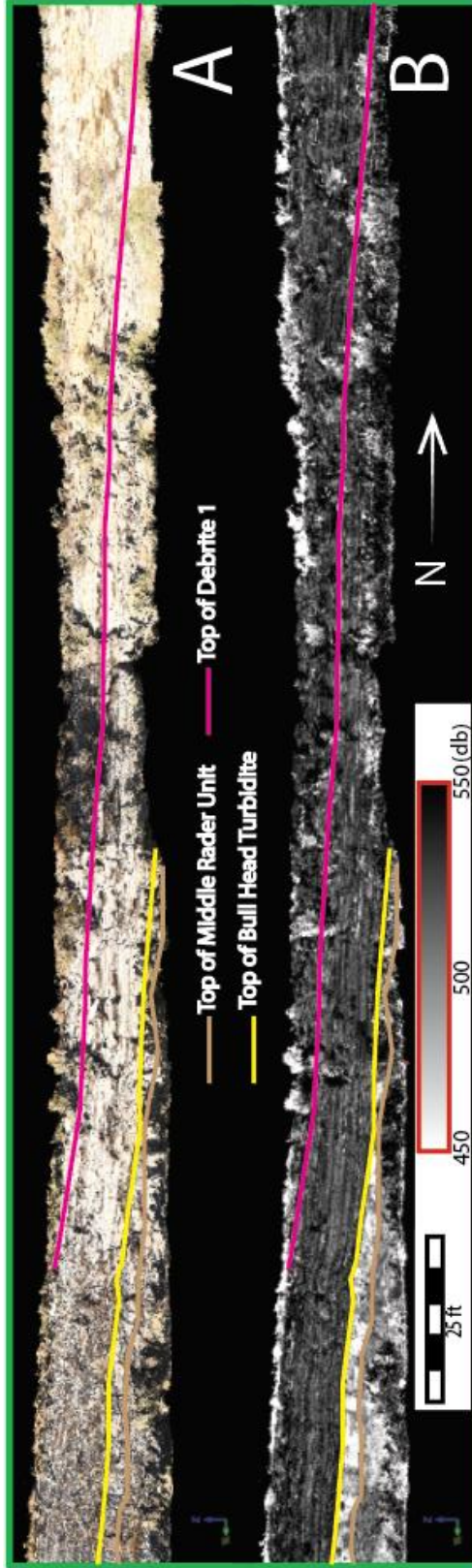
Figure 40: Zoomed in LiDAR scan from the middle right of the outcrop (green box in the overview image) showing the top of the Mega Conglomerate Unit, Bull Head Turbidite, the Interbedded Limestone and Sandstone Unit 1, Debrite 1, and topped by the Interbedded Limestone and Sandstone Unit 2. A) Colored LiDAR scan with photos overlain on top of the LiDAR point cloud data. B) LiDAR scan showing reflectance attribute with a range of 450 dB to 550 dB in grayscale.

Zoomed in section of the Road Cut LiDAR scan on the middle right side of the Road Cut outcrop is highlighted by a green box in Figure 37. A small portion of the Mega Conglomerate Unit is observed in the bottom left of the image. Additionally, the Bull Head Turbidite, Interbedded Limestone and Sandstone Unit One which is topped by the Derbite One unit and the Interbedded Limestone and Sandstone Unit Two are seen in the scans shown in Figure 40.

Figure 40 displays some of the issues which can arise from coloring LiDAR scans with photos. Situations outside of the control of the operator can have negative impacts on the results such as orientation of the sun which can adversely affect the quality of the pictures. This is seen on the right side of Figure 40A where the sun is positioned in such a way that the pictures taken of the light tan outcrop make it difficult to discern the nature of the outcrop. This is also seen in the middle of Figure 40A, where shadows cast by vegetation on the outcrop make it difficult to identify outcrop characteristics. These adverse effects are not seen in scan displaying reflectance. Figure 40B allows for bed geometries on the right side of the outcrop to be observed.

As seen in Figure 39, the LiDAR scan displayed in reflectance excellently delineates the Bull Head Turbidite from overlying thin beds of the upper Rader interval. The thin beds making up the upper Rader (Interbedded Limestone and Sandstone Units One & Two and Debrite One) are clearly displayed.
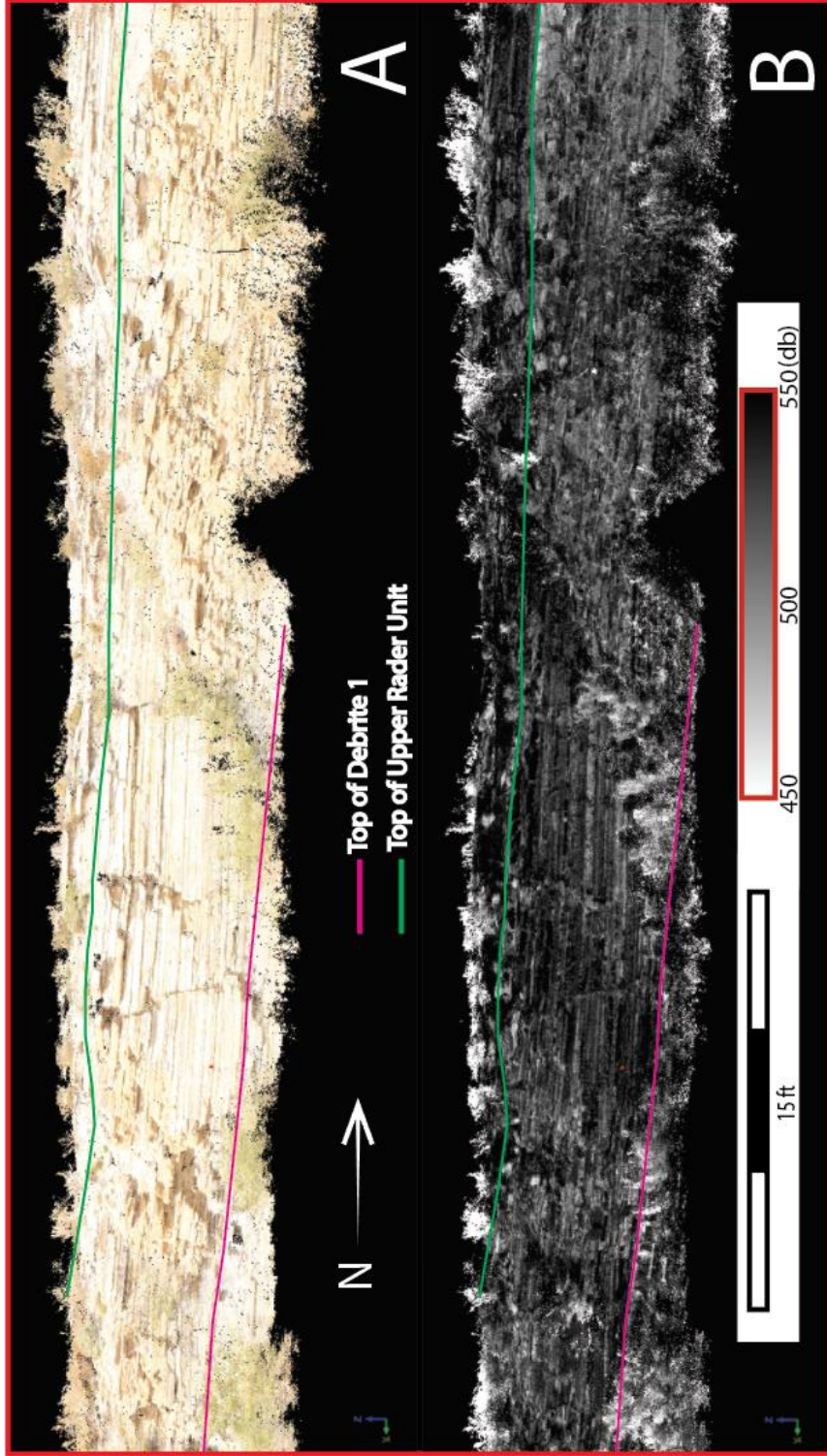
Figure 41: Zoomed in LiDAR scan from the right side of the outcrop (red box in outcrop overview image) showing the top of the Interbedded Limestone and Sandstone Unit 1, the top of the Debrite 1 unit, the Interbedded Limestone and Sandstone Unit 2, the top of the Debrite 2, and the Bell Canyon Sandstone Unit 2. A) Colored Lidar scan with photos overlain on top of the LiDAR point cloud data. B) LiDAR scan showing reflectance attribute with a range of 450 dB to 550 dB in grayscale.

Zoomed in section of the Road Cut LiDAR scan on the right side of the Road Cut outcrop is highlighted by a red box in Figure 37. A small portion of the Interbedded Limestone and Sandstone Unit One topped by Debrite One is observed at the bottom left side of the LiDAR scans. Additionally, the Interbedded Limestone and Sandstone Unit Two topped by Debrite Two which constitutes the top of the upper Rader interval is observed with the Bell Canyon Sandstone Unit Two overlying the top of the upper Rader.

The thin, parallel nature of the Interbedded Limestone and Sandstone Unit 1 is seen in both Figure 41A & B. However, some portions of the colored scan is obscured by the position of the sun when the picture/scan was taken. This also hinders the identification of the top of the Rader Formation in the scan colored by overlain photos. This is not observed in the scan displayed in reflectance, as the Debrite Two unit which marks the top of the Rader Formation is easily identified, especially on the right side of Figure 41B.

4.4.2 Road Cut Total Gamma Ray and Lithology Log
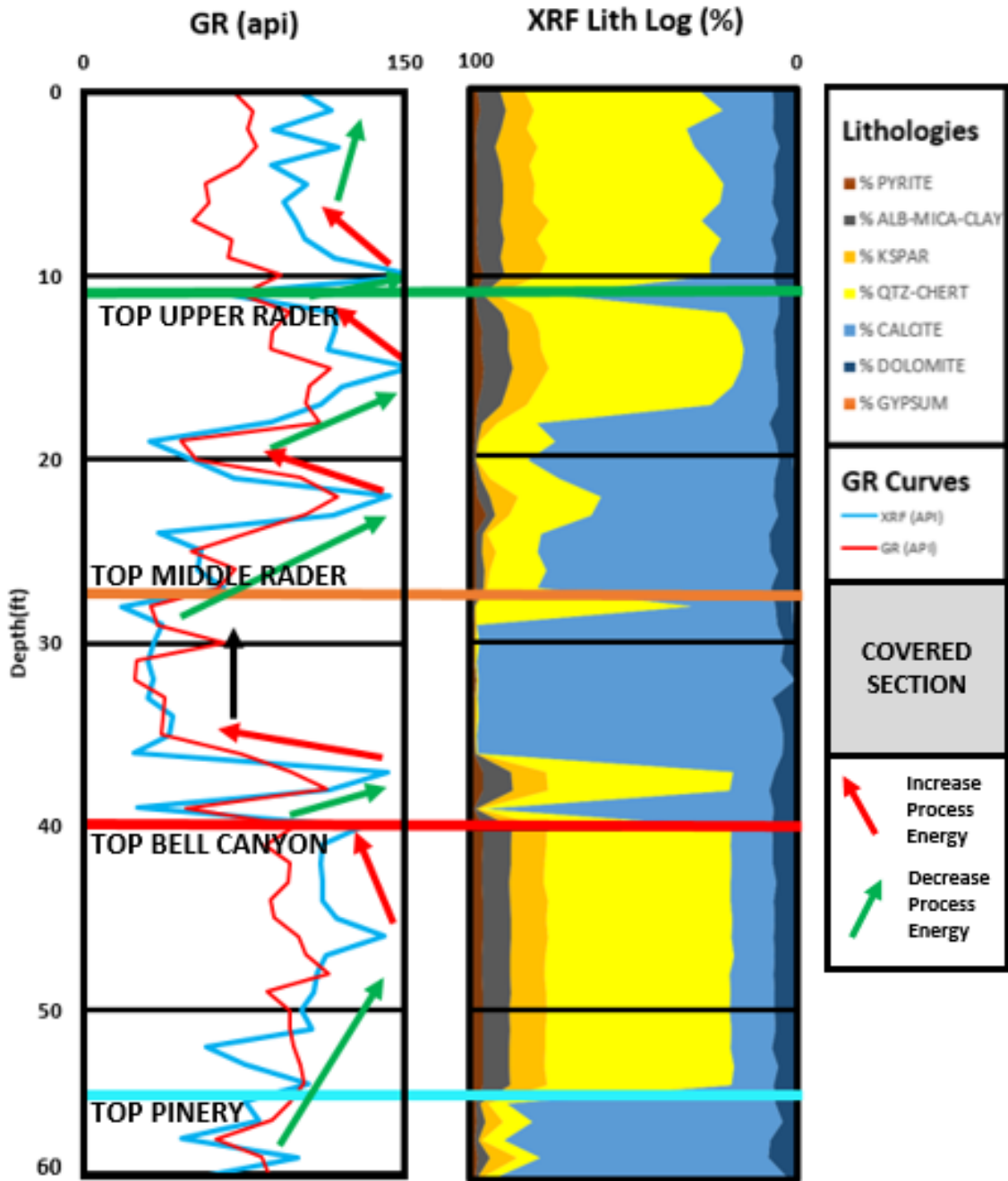
Figure 42: Total gamma ray generated from XRF measurements (blue curve) shown in API units. Base of the Road Cut measured section is seen at 60 ft and the top of the outcrop is measured at 0 ft. Lithology curve and legend seen on the right including lithology log coloring, GR curve coloring, and process energy trends.

The Pinery Formation observed at the base of the section from 60 ft to 56 ft is a carbonate dominant unit. It is the 2nd carbonate sub unit of the Bell Canyon Formation which precedes the Rader unit. The total pseudo gamma ray and total SGR gamma ray are variable in this interval, with no clear correlation in peaks and troughs to changes observed in the lithology log.

The overlying Bell Canyon formation, observed from 56 ft to 41 ft, is a dominantly sandstone unit. In this unit there is an increase in clay content seen from the lithology log which is expected in a more siliciclastically dominated interval. Additionally, a slight increase in pyrite is observed in comparison to the more carbonate dominated intervals. This interval is very consistent in terms of lithologic percentages observed. In outcrop observation, this interval is observed as homogeneous parallel laminated very fine grained sandstone. The total pseudo gamma ray and total SGR gamma ray curves are elevated relative to carbonate dominated intervals, though these curves do not exhibit as consistent of a profile as seen in the lithology curve. The SGR total gamma ray curve is more consistent than the total pseudo gamma ray curve which exhibits a significant trough at 52 ft and a large spike at 46 ft with no apparent change in lithology. Smaller spikes and troughs are also observed in the SGR total gamma ray curve, also with no corresponding change in the lithology curve.

The Mega Conglomerate Unit and Bull Head Turbidite, which make up the middle Rader interval, are observed from 41 ft to 28 ft and contains both carbonate and siliciclastic dominated intervals. These changes from carbonate dominated to siliciclastic dominated measurements represent the boulder sized carbonate intraclasts and very fine grained sandstone matrix respectively within the mega conglomerate

lithofacies. It should be noted that in this interval calcite has the largest contribution of any lithology, indicating that the boulder sized carbonate intraclasts are almost pure limestone. In this interval the total pseudo gamma ray and SGR total gamma ray change with the lithology curve, with siliciclastic dominated intervals corresponding to elevated gamma ray readings in both curves and carbonate dominated intervals matching suppressed gamma ray curves.

The middle Rader interval is topped by the upper Rader unit, observed form 28 ft to 11 ft, consisting of interbedded carbonate siliciclastic beds. The lower half of the upper Rader unit is more carbonate dominated from 28 ft to 18 ft, with a clear switch to a more siliciclastically dominated interval in the upper half of the upper Rader unit from eighteen ft to eleven ft where the upper Rader interval is topped by a large carbonate spike observed in outcrop as the Debrite Two unit (Table 1). In this interval, the total pseudo gamma ray as well as total SGR gamma ray curves are elevated when siliciclastics are dominant, and are suppressed when carbonates are the majority.

Above the upper Rader is the Bell Canyon Sandstone Unit Two (Table 1) observed from 11 ft to the top of the measured section. Similar to the Bell Canyon Sandstone Unit One observed from 56 ft to 41 ft, this is a sandstone dominated interval though higher concentrations of calcite are observed. Additionally, the profile of the lithology curve as a whole in this interval is not as consistent as that observed in the underlying Bell Canyon Sandstone Unit One. In outcrop this section is more fissile and portions do not exhibit parallel laminations. In this interval, the total pseudo gamma ray and total SGR gamma ray exhibit very similar trends, though the total pseudo gamma ray curve is elevated relative to the total SGR gamma ray curve. Here the total SGR

gamma ray curve exhibits more suppressed readings, similar to values exhibited in carbonate dominated intervals, while the total pseudo gamma ray curve exhibits more elevated readings, more consistent with values observed in other siliciclastically dominated intervals.

4.4.3 Road Cut Lithofacies Observations

The Road Cut outcrop shows similar lithofacies to the Creek Bed outcrop previously described, with small differences. Similarly to the Creek Bed outcrop, siliciclastic are a much larger constituency than in the more proximal Rader outcrops. Siliciclastic lithofacies observed at the Road Cut outcrop include amalgamated parallel laminated sandstone and laminated siltstone. A mixed carbonate siliciclastic lithofacies is observed in a matrix supported Mega Conglomerate Unit made up of massive boulder sized carbonate intraclasts in a fine grained sand matrix. Carbonate lithofacies observed at the Creek Bed outcrop include normally graded limestone units and very fine grained massively bedded limestones. All of the lithofacies observed at the Road Cut exhibit the same characteristics as those described above in the Creek Bed lithofacies section, but differences are observed in the parallel laminated sandstone facies and mega conglomerate facies.

The parallel laminated sandstone of the Bell Canyon Formation observed at the Road Cut outcrop are very similar to the same lithofacies observed at the Creek Bed outcrop, but the exposures are better due to the dynamite blasting used in the construction of US HWY 62. Figure 43(1) clearly exhibits the parallel laminations that are typically a dark orange color, with occasional dark gray laminations. As observed in the Creek Bed outcrop, these sandstone beds are amalgamated.

117

Laminated siltstone seen at the Road Cut outcrop are thicker than those seen in the more proximal Rader localities (Figure 43(2)). These siltstones are observed between sandstone beds within the Bell Canyon Formation (Figure 43(2) as well as between thin limestone beds of in the upper Rader interval. Similar to the laminated siltstone observed in the Creek Bed outcrop are 0.5 inches to 6 inches thick.

The mixed carbonate-siliciclastic lithofacies observed at the Road Cut is a mega conglomerate (Figure 43(3)). Similar to the Mega Conglomerate Unit observed at the Creek bed the Mega Conglomerate Unit observed at the road cut consists of boulder sized carbonate intraclasts entrained in a fine grained sandstone matrix. However, there are several differences between the Mega Conglomerate Unit observed at the Road Cut outcrop and the Mega Conglomerate Unit seen in the Creek Bed outcrop. Firstly, the color of the very fine grained sandstone matrix is a light tan color as opposed to the light gray color of the sandstone matrix observed at the Creek Bed outcrop, and is observed a formless sandstone in contrast to the chaotically bedded sandstone seen at the Creek Bed outcrop (Figure 33(2), Figure 33(6) & Figure 43(3)). Additionally, the large boulder sized intra clasts are rafted in the matrix throughout the Mega Conglomerate Unit at the Road Cut outcrop whereas they are ubiquitously observed at the base of the Mega Conglomerate interval at the Creek Bed outcrop. Also, there is no sand envelopes observed surrounding the boulder sized intraclasts observed at the Road Cut locality. There is soft sediment deformation caused by the intraclasts deforming underlying sandstone beds, but this deformation is subtle and not as easily identified as the soft sediment deformation at the Creek Bed outcrop. There are also significantly more boulders are observed within the Mega Conglomerate Unit at the Road Cut

118

outcrop than at the Creek Bed outcrop. Also, the boulders at the Road Cut outcrop are only seen in two dimensions, so it is impossible to make inferences about their geometries. Finally, all of the carbonate intraclasts observed at the Creek Bed outcrop appear to be homogeneous micritic limestone. In contrast the boulder size carbonate intraclast at the Road Cut exhibit variable make ups with some being homogeneous micritic limestone like observed at the Creek Bed outcrop, but many have large cobble sized carbonate intraclasts within a homogeneous micritic limestone matrix.

Graded limestone beds are also observed at the Road Cut outcrop. These beds are fine grained (Figure 43(4)), and exclusively observed in the upper Rader unit. These beds are thin to medium bedded with thicknesses ranging from 2 inches to 6 inches. Unlike the Bull Head Turbidite seen at the Creek Bed outcrop, the Bull Head Turbidite observed at the Road cut does not exhibit grading.

The final carbonate lithofacies observed at the Road Cut outcrop is a fine grained massively bedded limestone (Figure 43(5)). These beds are similar to those observed at the Creek Bed outcrop. They are found throughout the upper Rader interval and are 1 inch to 6 inches thick. Also, unlike the massively bedded limestone observed in the more proximal localities there are no chert nodules observed in these beds at the Road Cut outcrop.
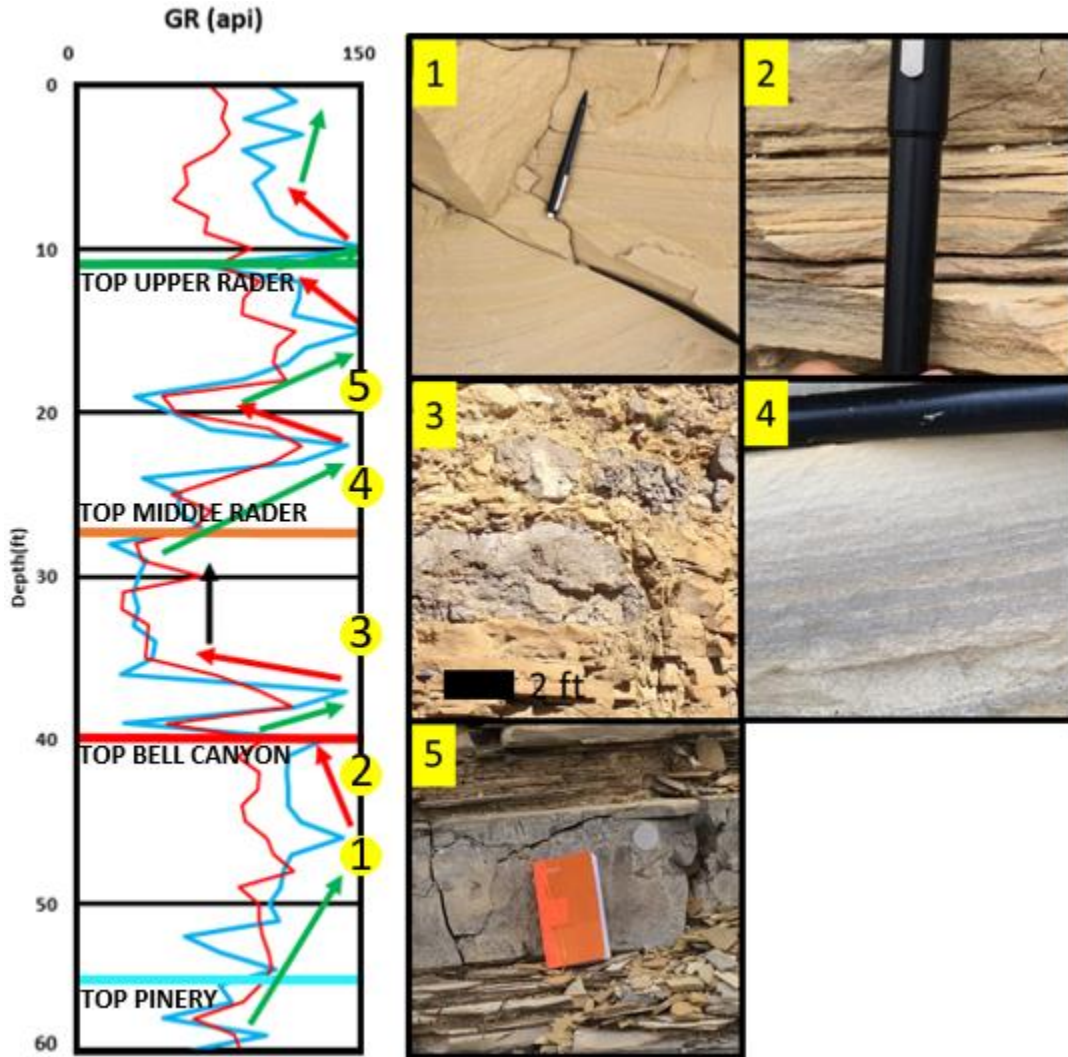
Figure 43: Lithofacies observed at the Road Cut outcrop. 1) Amalgamated parallel laminated sandstone of the Bell Canyon Formation. 6 inch pencil for scale. 2) Laminated siltstone observed in the Bell Canyon Formation. 6 inch pencil for scale 3) Mega Conglomerate Unit observed at the Road Cut outcrop. 2 ft black bar for scale. 4) Graded limestone bed from a limestone bed of the Interbedded Limestone and Sandstone Unit 1. 6 inch pencil for scale 5) Fine grained massively bedded limestone bed from Debrite 1. 8x5 inch note book for scale.

4.4.3 Road Cut Morphological Observations

Small anticlinal folds observed at the Road Cut outcrop occur in mixed siliciclastic and carbonate intervals below and above the Mega Conglomerate Unit (Figure 44). Though the constituent beds observed in the folding at the Road Cut outcrop are not as homogeneous as those observed at the Creek Bed outcrop, bedding thicknesses remain constant, inferring again, that differential compaction does not contribute to the folding observed.

Figure 44: low angle anticlinal folding observed in mixed carbonate-siliciclastic unit at the Road Cut outcrop. Not the constant bed thicknesses observed in both the carbonate and siliciclastic beds.

Soft sediment deformation is also observed at the Road Cut outcrop, though it is more subtle than observed at the Creek Bed outcrop. It is possible that the sand enveloping observed at the Creek Bed is present at the Road Cut outcrop, but dynamite blasting used in the construction of HWY 62 removed this texture. However, subtle

soft sediment deformation is observed beneath carbonate boulders which make up the Mega Conglomerate Unit of the middle Rader interval.

Characteristics indicating channeling or amalgamated deep water fan deposits are also observed at the Road Cut outcrop seen in Figure 45 below. The LiDAR scan taken along the Road Cut outcrop is useful in recognizing the subtle differences in bed geometries between stratigraphic units. In field observations, the dip of bedding angles observed at the Road Cut outcrop appear to be consistent throughout all lithologic units. However, it was observed after viewing the outcrop several times that there is a slight change in dips between the Bell Canyon sandstones and the overlying units constituting the Rader Formation. This observation was confirmed when measuring dips with a Brunton compass. The dips of the Bell Canyon sandstone are 7 degrees while the dips of the overlying Rader strata are 12 degrees. Upon inspecting LiDAR scans acquired at this location, a change in dip between Bell Canyon Sandstone and the beds constituting the Rader Limestone is clearly observed, and is much more pronounced than when observing the feature in the field (Figure 45). The ability of the LiDAR to enhance subtle differences in bed geometries could be key in studies where portions of the outcrops are not able to be measured with a Brunton compass.
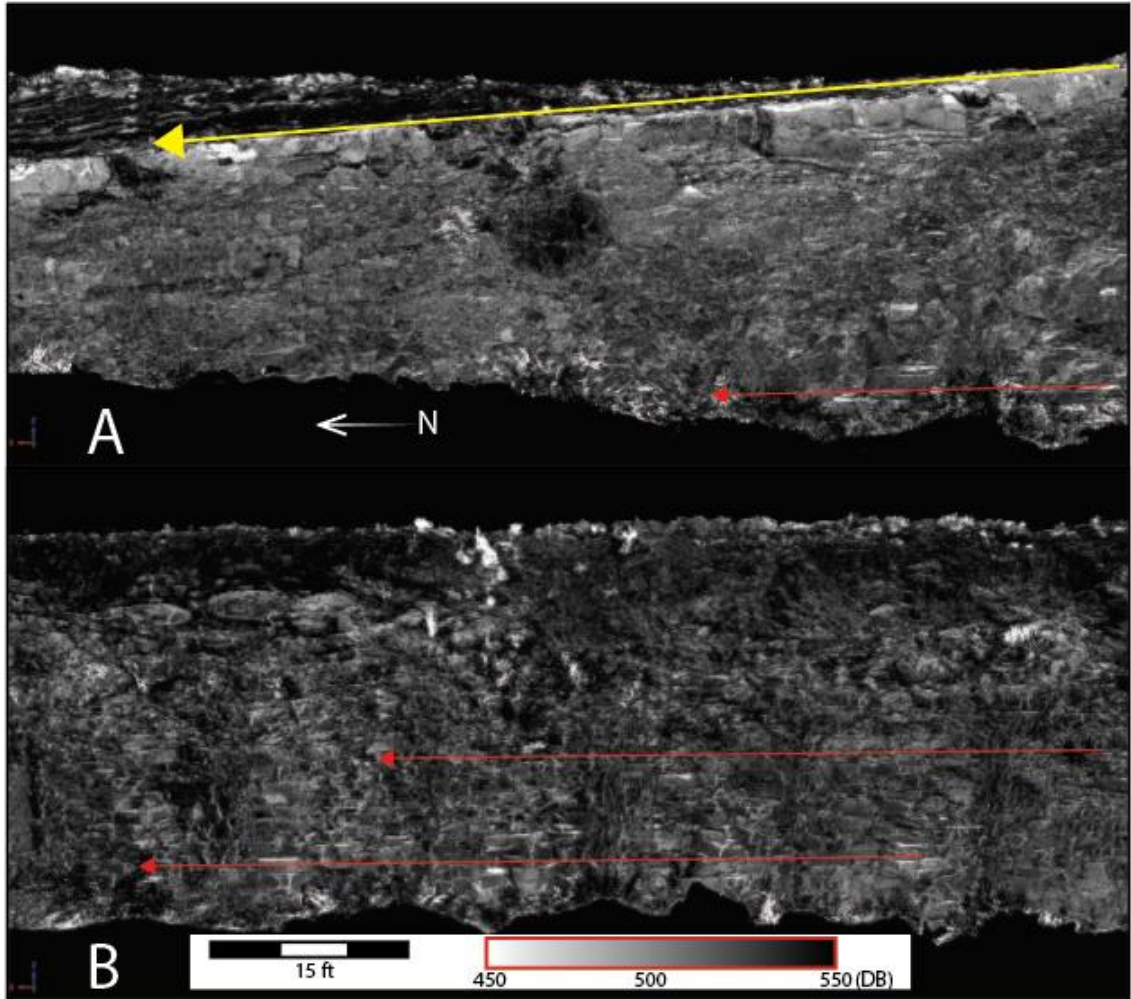
Figure 45: LiDAR scans showing reflectance range of 450 to 550 dB. Center of top images is approximately 35m from center of lower image. A subtle difference in dip between the Bull Head Turbidite of the Rader Formation and underlying sandstone beds of the Bell Canyon Formation is exacerbated when observed in LiDAR scans relative to viewing in the field. (A) The contact between the Bull Head Turbidite and overlying thin bedded carbonates. Notice the angle of dip. (B) Very low angle dipping sandstone beds of the Bell Canyon Formation.
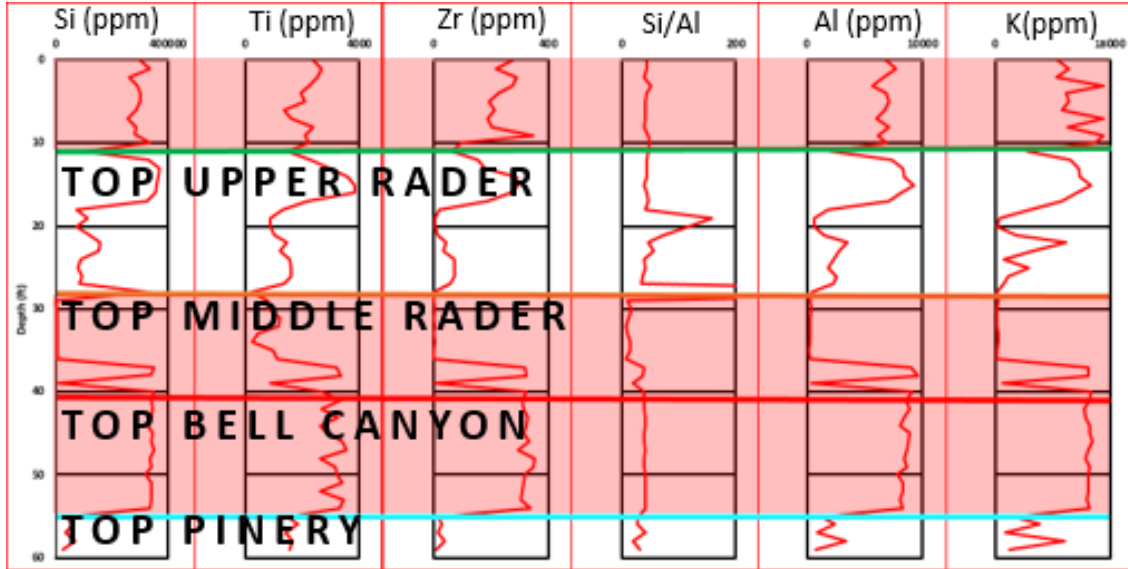
Figure 46: Clastic, clay, composition, lowstand proxy elemental logging suite for the Road Cut outcrop displaying Si, Ti, Zr, Si/Al, Al, and K curves from right to left. 60 ft marks the base of the outcrop and 0 ft marks the top of the outcrop. Light blue, red, tan, and green horizontal lines represent the top of the Pinery formation, top of the Bell Canyon formation, top of the middle Rader unit, and top of the upper Rader unit respectively.   Highlighted red intervals represents intervals of elevated clastic/lowstand elemental proxies relative to other intervals.

Si, Ti, Zr, Al, and K values are all suppressed in the Pinery interval in

comparison to all other intervals besides the middle Rader interval. All proxies are

relatively constant except for Al and K which have significant spikes.

The Bell Canyon Sandstone Unit One is clearly delineated by elevated levels of

all of the terrigenous proxies. Once again, all terrigenous proxies correlate well and

there are no Si/Al spikes observed in this interval indicating that the Bell Canyon

Sandstone Unit One is sourced from detrital sources.

All of the terrigenous proxies decrease sharply at the interval separating the top

of the Bell Canyon sandstone interval from the middle Rader unit. All of the proxies

show a flat curve in the middle Rader unit except for Ti which forms a trough geometry.

Si and Si/Al each have a peak at the base of the Upper Rader interval that is not reciprocated by the other proxies indicating an isolated biogenic or diagenetic siliciclastic bed.   Si/Al has a second peak in the middle of the interval, but this does not correspond to a peak in Si, but rather to a decrease in Al at seventeen ft. All of the proxy's exhibit elevated levels from eighteen ft to twelve ft indicating a more clastically dominated Interbedded Limestone and Sandstone Unit Two interval (Table 1). Si, Ti, Zr, Al, and K exhibit strong covariation in the upper Rader interval. The upper Rader interval ends with all terrigenous proxies exhibiting a large trough in response to the carbonate Debrite Two (Table 1).

Above the upper Rader unit all proxies correlate well and no spikes in the Si/Al curve are observed. Si and Al proxies exhibit a constant to slight increasing trend from the base of the second Bell Canyon unit (Table 1) to the top of the outcrop. Zr and Ti correlate well showing more variable concentrations, but an overall upwards increasing trend from the base of the second Bell Canyon unit to the top of the outcrop. K also exhibits variable concentrations throughout the second Bell Canyon unit, and is the only proxy to show an overall decreasing upward trend from the base of the unit to the top of the outcrop.
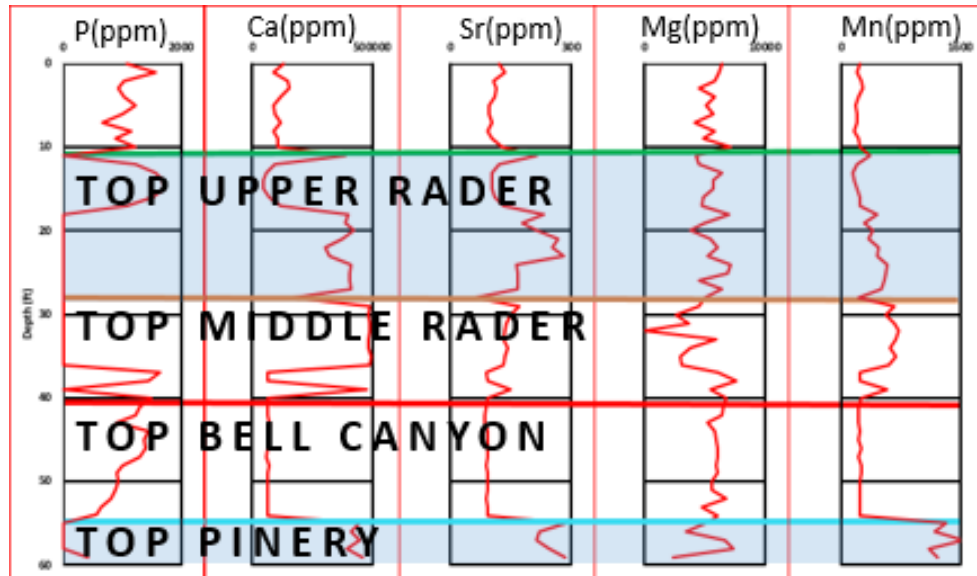
Figure 47: Carbonate, composition, highstand elemental proxy suite for the Road Cut outcrop displaying P, Ca, Sr, Mg, and Mn curves from left to right. 60 ft marks the base of the outcrop and 0 ft marks the top of the outcrop. Light blue, red, tan, and green horizontal lines represent the top of the Pinery formation, top of the Bell Canyon formation, top of the middle Rader unit, and top of the upper Rader unit respectively. Highlighted blue intervals represents intervals of elevated carbonate/highstand elemental proxies relative to other intervals.

P is only observed at the very base of the Pinery interval. Carbonate proxies are elevated in the Pinery interval, but do not show particularly strong correlations in regards to matching peak and trough geometries. Ca and Mn are relatively constant, while Sr and Mg show variable concentrations. The highest concentrations of Mn are observed in the Pinery Formation.

There is an upward increasing trend seen in P from the base of the first Bell Canyon Sandstone interval, peaking at the top of the interval. Ca, Sr and Mn are all significantly attenuated and show a very consistent profile throughout the interval. Mg is elevated in the Bell Canyon sandstone interval relative to Ca, Sr, and Mn.

P is only observed as a large spike near the base of the middle Rader interval associated with the sandstone seen in Figure 47. This peak correlates to a small peak

observed in Mg and also to sudden troughs observed in Ca, Sr, and Mn. Ca, Sr, and Mn are elevated throughout the interval, though Ca and Mn have a stable profile, while Sr has an increasing profile moving upward in the middle Rader unit. Mg is variable and the peaks and troughs observed do not correlate well to any other curve in the middle Rader unit.

P is only observed at the top of the Upper Rader interval as a sudden spike that matches the switch from the lower carbonate dominated interval of Interbedded Limestone and Sandstone Unit One to the more siliciclastically dominated interval of Interbedded Limestone and Sandstone Unit Two (Table 1) seen in Figure 42. Ca and Sr are correlative throughout the upper Rader unit, exhibiting a large trough at the top of the interval which matches the peak observed in P and the increases observed in the terrigenous proxies from eighteen ft to twelve ft (Figure 46). Mg is relatively constant throughout the upper Rader interval. Mn shows an obvious upward decreasing trend from the base of the upper Rader unit to the top of the interval. A small trough is observed from eighteen ft to twelve ft, though it is of smaller magnitude that of those observed in Ca and Sr at the same interval.

P shows an increasing trend from the top of the upper Rader unit to the top of the outcrop. Ca, Sr, Mg, and Mn all correlate well above the top of the upper Rader unit, exhibiting relatively stable and constant trends from the top of the Rader unit to the top of the outcrop. Mg exhibits more variable measurements than Ca, Sr, and Mn.
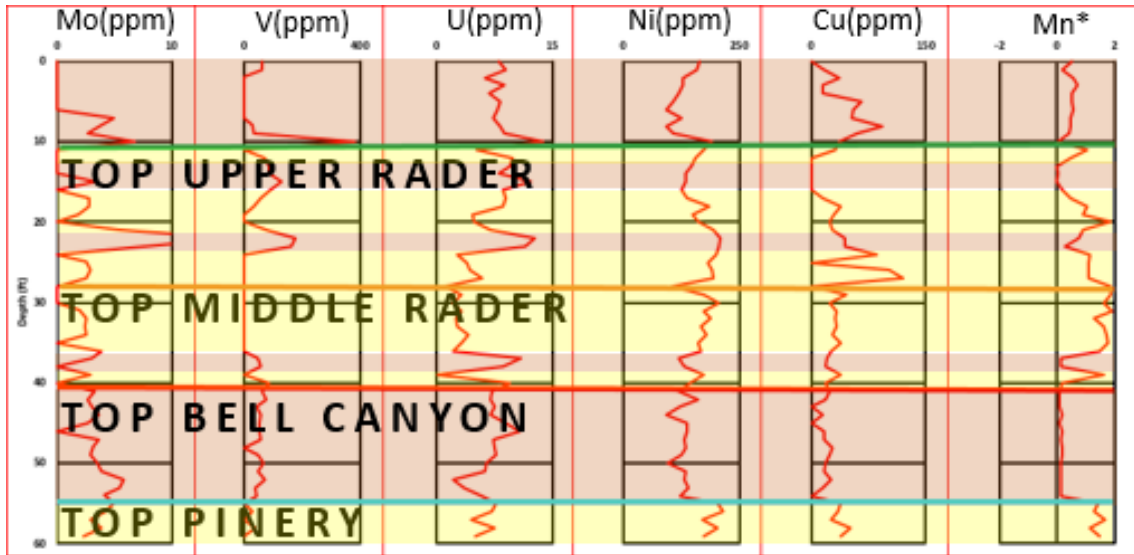
Figure 48: Paleo redox, basin restriction, and paleo environment elemental proxy suite for the Road cut outcrop displaying Mo, V, U, Ni, Cu, and Mn* curves from left to right. 60 ft marks the base of the outcrop and 0 ft marks the top of the outcrop. Light blue, red, tan, and green horizontal lines represent the top of the Pinery formation, top of the Bell Canyon formation, top of the middle Rader unit, and top of the upper Rader unit respectively. Highlighted yellow intervals represents intervals of more oxic conditions, while highlighted brown intervals represent intervals of more anoxic conditions based on elemental proxies.

Mo shows an increasing trend moving upward in the Pinery interval while V has relatively constant trend in the interval. U, Ni, Cu and Mn* all exhibit constant elevated concentrations throughout the Pinery Formation.

Mo shows a decreasing trend moving upward from the base of the Bell Canyon Sandstone Unit One interval to the base of the middle Rader unit. Conversely, V has a very subtle increasing trend moving upward from the base of the Bell Canyon to the top of the interval. Mn* exhibits the lowest readings in the entire Road Cut outcrop within the Bell Canyon Sandstone Unit One interval. U, Ni and Cu correlate relatively well in the Bell Canyon Sandstone Unit One, though U exhibits concentrations higher than observed in the Pinery Formation while Cu and Ni exhibit lower concentrations than observed in the Pinery Formation than observed in the Bell Canyon Sandstone.

128

Mo exhibits a constant to slightly upward decreasing trend in the middle Rader interval. V is only observed from the base of the middle Rader interval to 36 ft. Ni and Cu correlate very well in the middle Rader unit, with both exhibiting upward increasing trends from the base of the middle Rader unit to the top of the interval. U exhibits a trend that is the inverse of those observed in Ni and Cu in the middle Rader unit. Peaks observed in U at the base of the middle Rader interval correlate with peaks observed in V and Mo and also with troughs observed in Mn*. From 36 ft to the top of the middle Rader unit, U exhibits a slight upward decreasing trend. Mn* is elevated compared to the Bell Canyon sandstone interval below the middle Rader unit.

Mo displays constant concentrations through most of the upper Rader interval with a large spike observed at 22 ft. This spike is observed in V and U, but is observed as a significant trough in Mn*. V correlates well with U with both exhibiting an inverse relationship to concentration levels observed in Mn* throughout the upper Rader interval. Ni and Cu are covariate relatively well, with both displaying overall decreasing trends upward from the base of the middle Rader unit through the top of the interval. Mn*, as stated previously exhibits an inverse relationship to Mo, V, and U. Mn* displays lower values associated with sandstone dominated intervals and higher readings associated with carbonate dominated intervals (Figure 42 & Figure 48).

Mo, V, U, and Ni are covariate, exhibiting peaks at the base of the second Bell Canyon interval and having subdued concentrations from six ft to the top of the outcrop. The peaks observed in these proxies are reciprocated by troughs observed in Mn*. Cu is not correlative with any other proxies in the second Bell Canyon interval and displays an overall upward decreasing trend from the base of the unit to the top of the outcrop.

Mn* exhibits consistently subdued concentrations throughout the second Bell Canyon

interval, with the lowest values being observed in correlation with increased values in

V, Mo, and U.

4.4.5 Road Cut Thin Section Observations
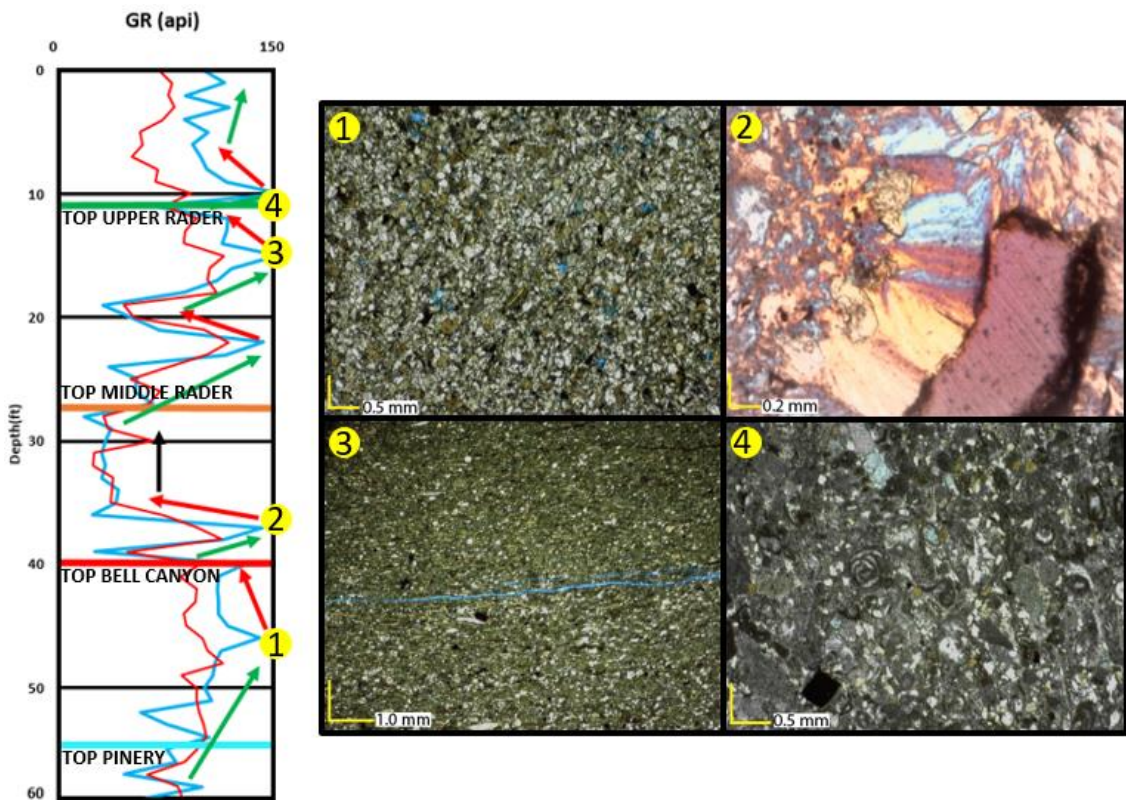
Figure 49: Thin section micro photographs of samples taken from the Road Cut outcrop location. All micro photographs taken under plain polarized light except 2 which was taken using a gypsum plate. 1) Sample taken from the Bell Canyon Sandstone Unit 1. 2) Sample taken from a limestone boulder within the Mega Conglomerate Unit. 3) Sample Taken from fine grained limestone bed of Interbedded Limestone and Sandstone Unit 2. 3) Sample taken from Debrite 2.

Figure 49(1) shows a thin section sample taken from the Bell Canyon Sandstone

Unit One (Table 1) observed beneath the Rader Formation. This sample is made up of

very fine sub angular to sub rounded quartz grains. Orthoclase and albite grains are

observed as minor constituents. Additionally, sparse organics and sponge spicules are

observed throughout the sample as well as limited porosity, seen as light blue voids in the thin section.

Figure 49(2) shows a thin section taken from a large limestone boulder from within the Mega Conglomerate Unit. This image was taken with a gypsum plate in the microscope. The unique crystal structure highlighted in Figure 49C is length-slow chalcedony. Folk and Pittman (1971) state that this is unusual in nature. They go on to state that the rare type of fibrous silica occurs almost exclusively in association with sulphates and evaporites, forming primarily in salt-flat, Sabkha, or sulphate-rich environments. This observation could have major implications on the provenance of the carbonate boulders found within the Mega Conglomerate Unit.

Figure 49(3) shows a thin section sample taken from a limestone bed of the Interbedded Limestone and Sandstone Unit Two (Table 1). A distinct fining upwards trend is observed in this sample, grading from a fossiliferous wackestone at the base into a fossiliferous mudstone towards the top. Sponge spicules, bryozoans, foraminifera, and radiolarians are observed throughout the sample.

Figure 49(4) shows a thin section taken from the Debrite Two lithologic unit. This unit is a fine grained fossiliferous grainstone. No grading is observed in the thin section. Angular to sub-rounded quartz grains are present alongside foraminifera, brachiopod spines, sponge spicules, bryozoans, and pellets. Organics are observed but no oil staining is seen.

Chapter 5: Interpretation

The study of the Rader Formation provides critical insight to understanding process sedimentology of deposits in the transition from the Capitan Reef slope into the Delaware Basin. Observations detailed above are synthesized below in an attempt to explain provenance, depositional settings, a sequence stratigraphic model, sedimentation mechanisms responsible for the deposition of the Rader Formation, cause of the interpreted platform failure, and provide evidence of tsunami deposits. This interpretation not only aims to elucidate the depositional environment and processes responsible for the Rader Formation, but also hopes to aid in the interpretation of other analogous deposits in the Delaware Basin and beyond.

5.1 Provenance

Mentioned in the background, the Delaware basin, as with almost all basins, is divided into discrete depositional settings such as the shelf, margin, and basin, (Figure 2). These areas can be further divided into back reef, reef crest, fore reef, slope, etc. By examining faunal assemblages found within the Rader deposits, sources and provenances may be determined as different discrete areas mentioned above which contain different characteristics such as: water circulation, salinity, light, energy, depth, etc. (Lawson, 1989). These characteristics affect what organisms can survive in each environment as well as which sedimentary structures would be observed.

During the time of Rader deposition, the Delaware Basin was becoming increasingly restricted, causing non-normal salinity conditions. As a result, during this time the reef was likely becoming sick and less diverse. These conditions could exacerbate failure of a portion of the platform. However, fossils and grains observed in

outcrop and thin section analysis do not indicate that the entire carbonate platform collapsed. Lack of non-skeletal grains, such as ooids, indicate that the restricted back reef environments were not affected by the platform failure and resulting catastrophic flow deposits. Additionally, the absence of clasts which have fenestral fabrics, pisolitic grains and restricted marine fauna further support this interpretation (Lawson, 1989). However, some coated grains are observed in thin section samples taken from the mega breccia deposit on Rader Ridge (Figure 22(2)) indicating that some sediment may have been derived from the reef crest. Additionally, large sponge fossils contained within the mega breccia and mega conglomerate, as well as the presence of rugose coral fragments further support the interpretation that portions of the reef crest were involved in the platform failure.

Floatstones observed in the mega breccia and mega conglomerate deposits of the middle Rader interval, as well as coated grains observed in the mega breccia indicate that some of the allochthonous debris making up the middle Rader unit was derived from the reef crest. Skeletal to no skeletal grainstones, packstones and wakestones which dominate the lower and upper Rader deposits indicate a source basinward of the reef crest, but shelfward of the toe of slope.

The flows responsible for the lower and upper Rader deposits likely occurred as the sediment built up on the slope and exceeded the angle of repose. Mudstones observed in the lower and upper Rader deposits are interpreted to be pelagic to hemipelagic deposits, though it is not certain if these are a result of settling from the numerous sub aqueous gravity flows observed or just sediment falling out of the nepheloid layer. The mega breccia and mega conglomerate units which constitute the

133

majority of the middle Rader interval is interpreted to have been derived from the reef crest and fore slope deposits as a result of platform failure.

5.2 Water Depth and Redox Interpretation

Based on present day relief from the top of the Capitan Reef and the Bell Canyon Formation, Newell et al., (1953) estimated water depth to be 1500 ft 1.5 miles from the rim of the basin. Though there is no consensus on water depth during the deposition of the Rader Formation, most authors agree that water depths were greater than 900 ft (Adams, 1936; King, 1948; Meissner, 1972; Lawson, 1989).

Most researchers have suggested that the basin during the deposition of the Rader Formation was anoxic (Fischer and Sarnthein, 1988; Lawson, 1989). However, elemental proxies, obtained through XRF measurements in this study, suggest a more suboxic environment during deposition of the carbonate dominated intervals of all outcrop locations measured (Figure 18, Figure 21, Figure 29 & Figure 48). This is clearly displayed in the Mn* proxy in which higher values represent more oxic conditions while lower values represent less oxic conditions (Figure 18, Figure 21, Figure 29 & Figure 48). In contrast the siliciclastic dominated intervals show more anoxic trends, which are illustrated by low values observed in the Mn* proxy (Figure 18, Figure 21, Figure 29 & Figure 48).

Mo and V values are observed to be suppressed except for isolated peaks (Figure 18, Figure 21, Figure 29 & Figure 48). This supports the interpretation of more oxic conditions, as opposed to anoxic conditions. However, during the deposition of the Rader Formation, the Delaware Basin was becoming increasingly restricted from the Panthalassa Ocean. This increasing restriction is interpreted to be the main cause of

low Mo and V readings (Algeo and Rowe, 2012). Algeo and Rowe (2012) describe this as the reservoir effect, where increasing restriction results in low deep water Mo and V due to a lack of replenishment of these elements from normal oceanic conditions.

Bioturbation is exclusively observed at the Rader Ridge outcrop in the lower Rader interval. The bioturbation is scarcely observed and isolated, supporting the interpretation of suboxic conditions. Suboxic conditions and discrete intervals of bioturbation observed in the lower Rader unit on Rader Ridge could be the result of oxygenated waters being brought down into the less oxic, deep basinal waters by sub aqueous gravity flows responsible for the deposition of the majority of the rocks observed in the study area (Harms and Williamson, 1988).

5.3 Depositional Setting

The observations that are detailed above are best organized into the facies of an upper slope submarine fan. This view is supported by Jacka et al., (1972) who proposed a submarine fan channel complex as the primary depositional mechanism within the Delaware Basin for sediments deposited basinward of the shelf edge. However, this hyperpycnal flow interpretation is not shared by all who have studied Delaware Basin deposits. Most notably, Harms and Williams (1988) interpreted basinal siliciclastic sediment to be transported into the basin via saline density currents. These dense bottom-hugging currents are interpreted by Harms and Williams (1988) to have eroded broad, flat channels filled by sandstone and siltstones. This divergence of views is due to the ambiguity surrounding how fine grained siliciclastics were transported into the basin. The interpretation proposed by Harms and Williams (1988) relied heavily on the notion of sediment by-pass by a density stratified water column providing a means to

transport sediment over the carbonate reef rimmed margin of the Delaware Basin. This

sediment transportation interpretation was supported by the study of the Rader

Formation conducted by Lawson (1989).

From this study, it was determined that a more probable model is one where

paleo-canyons and channels allowed for sediment to enter the basin. These paleo-

canyons and channels are hypothesized to be expressed as present day canyons, such as

McKittrick and Slaughter Canyon (Personal Communication of 2017 with Dr. John D.

Pigott). This hypothesis is supported by Figure 50 showing an isopach map of the Bell

Canyon Formation deposited prior to Rader Limestone deposition (Geissen and Scholle,

1990). This map highlights several localized input points for grain flow and turbidite

transport of sediments into the basin. On the isopach map, the thicker sediment

intervals are interpreted as submarine canyons closer to the basin margin and fans

farther out into the basin (Geissen and Scholle, 1990). Colored dots in Figure 50 show

approximate outcrop locations used in this study (Personal Communication of 2017

with Dr. Peter Scholle).
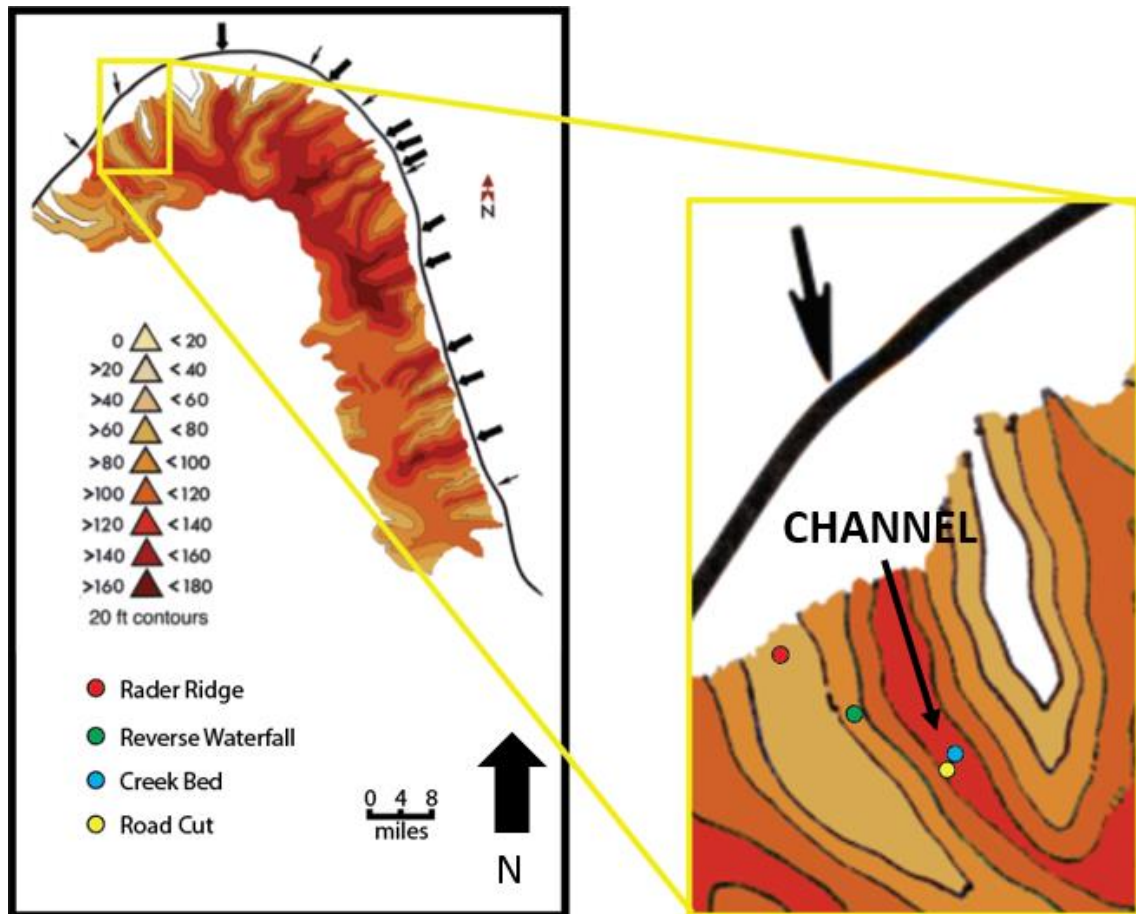
Figure 50: Isopach map of Bell Canyon formation prior to Rader Deposition. Several well defined, localized input points (arrows) of downslope subaqueous flows through submarine canyons and fans. Colored dots represent approximate location of outcrop localities. Figure modified from Scholle et al. (2015).

From this model, it is interpreted that the Rader Ridge outcrop and Reverse Waterfall outcrop are located in a more marginal portion of the upper slope submarine fan margin, while the Creek Bed and Road Cut outcrops are located in a more central, upper slope submarine fan channel axis environment (Figure 50). This is supported by the higher energy required to deposit the large, boulder sized intraclasts observed in the Mega Conglomerate Unit at both the Creek Bed and Road Cut outcrops. In contrast, the mega breccia observed at the Rader Ridge and the Reverse Waterfall outcrops contain smaller carbonate intraclasts that reach a maximum of a couple of feet in their longest

137

exposed dimension. Additionally, the matrix of the mega conglomerate observed at the

Road Cut and Creek Bed outcrops is a fine sandstone while the matrix of the mega

breccia is a fine calcarenite, indicating a different depositional facies. This

interpretation is further supported by a lack of correlation in total gamma ray trends

seen in Figure 51.
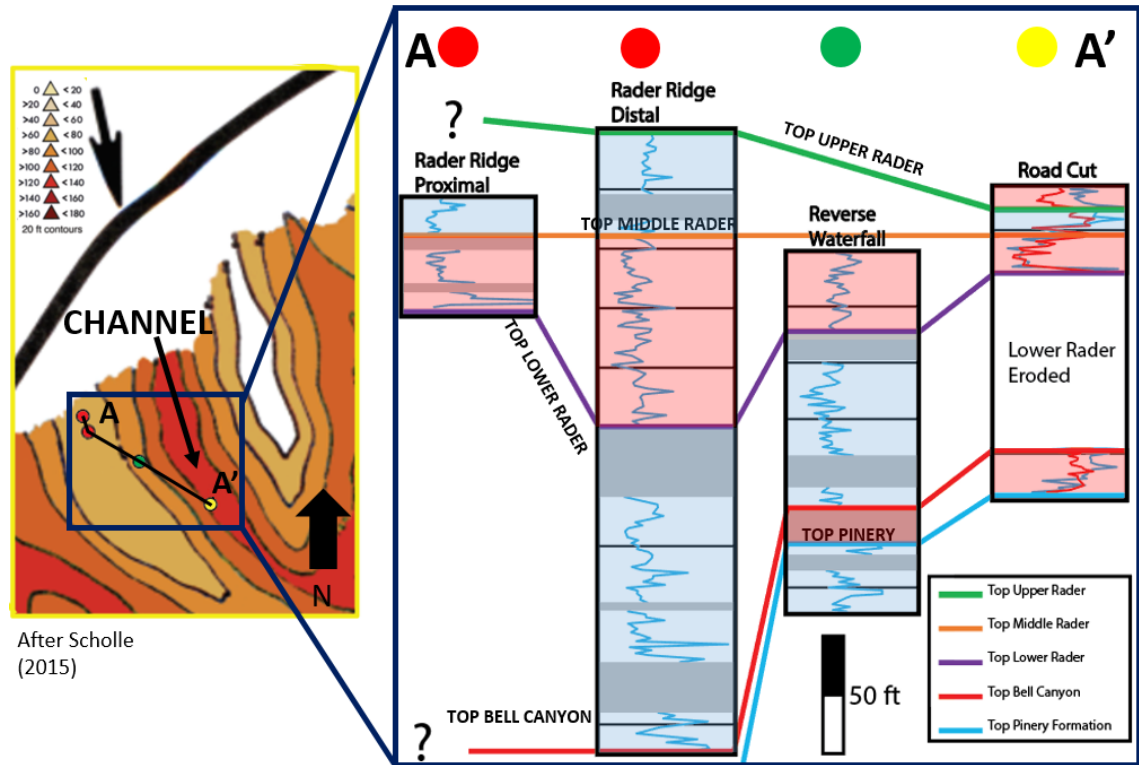
Figure 51: Fence diagram of total gamma ray profiles from all outcrop locations. The profiles are hung on the top of the middle Rader unit. These profiles represent Rader Ridge Proximal, Rader Ridge Distal, Reverse Waterfall, and Road Cut outcrop locations from left to right respectively. The lack of GR correlation between localities indicate these outcrops occur in different depositional facies of an upper slope submarine fan. Red and blue highlighted intervals represent interpreted lowstand and highstand deposits based on geochemical proxy analysis.

5.4 Sequence Stratigraphic Interpretation

Fluctuations in sea level have been studied in detail since the introduction of sequence stratigraphy by Larry Sloss (1963), the father of American stratigraphy. In a mixed carbonate and siliciclastic environment, as is observed in the Delaware basin, changes from carbonate to siliciclastic intervals indicate fluctuation in sea levels (Mullins and Cook, 1986). In general, increased carbonate content is accepted to indicate higher sea levels, while increased siliciclastic input is interpreted to represent lower sea level conditions (Silver and Todd, 1969; Mullins and Cook, 1986; Nance and Rowe, 2015). Mullins and Cook (1986) described this as reciprocal sedimentation, in which they note that carbonate sediment gravity flows along deep-water flanks of carbonate platforms do not typically produce submarine fans, but rather form wedge-shaped carbonate aprons. This pattern of deposition is observed in the study area, and is modeled below in Figure 52.
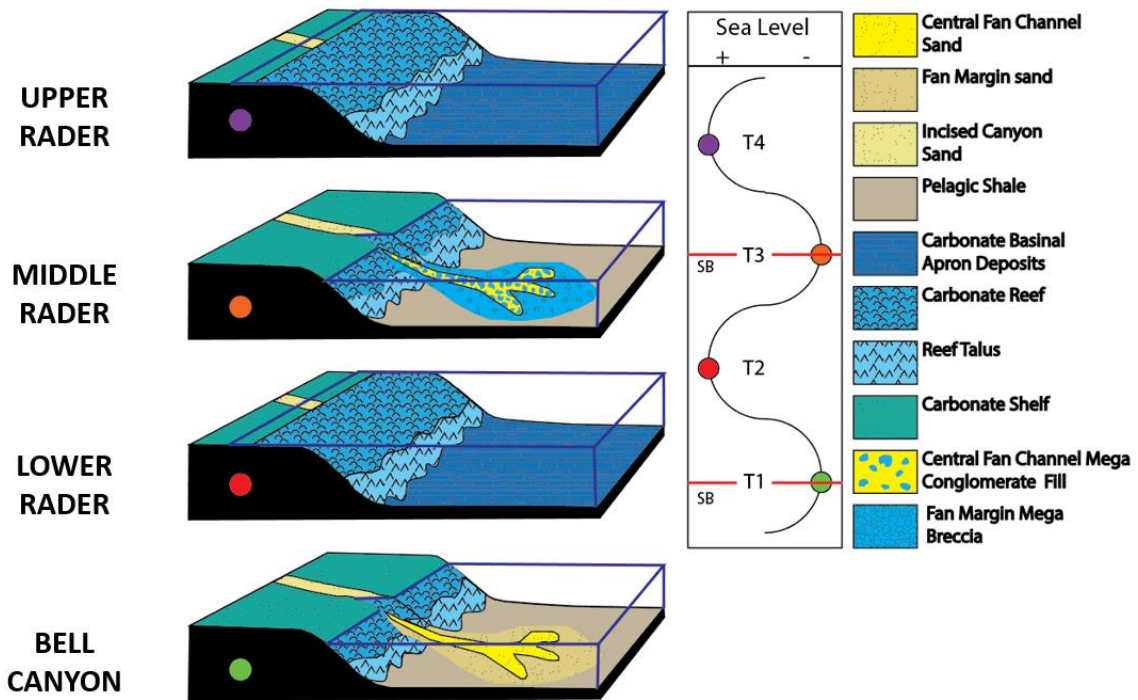
Figure 52: Model of reciprocal sedimentation during deposition of Rader Formation. T1 represents a low stand in which siliciclastic fan is deposited. T1 is interpreted to be the deposition model for the Bell Canyon Sandstone. T2 shows a highstand in which carbonate reef transgresses, reef talus expands down slope, and basinal deposits are blanketed by fine grained carbonate wackestones and grain stones. T2 is interpreted to be the deposition model for the lower Rader unit. T3 shows a lowstand in which the fan channel fills and fan margin facies are filled and dominated by matrix supported carbonate mega conglomerate and matrix and clast supported carbonate mega breccia respectively. T3 is interpreted to be the deposition model for the middle Rader unit. T4 shows a highstand in which carbonate reef transgresses, reef talus expands down slope, and basinal deposits are blanketed by fine grained carbonate wackestones and grain stones. T4 is interpreted to be the deposition model for the upper Rader unit.

Using relative fall in sea level as parasequence boundaries, the Rader

Formation contains two parasequence boundaries. However, the entire outcrop

observed at the Road cut contains three sequence boundaries. At the Road Cut outcrop,

the first boundary is observed in the transition from the Pinery Formation to the Bell

Canyon Sandstone Unit One (Table 1). This follows the framework of reciprocal

sedimentation, with the Pinery expressing a carbonate apron and the overlying Bell

140

Canyon interval representing a siliciclastic fan deposited during a sea level low stand (Figure 52). The next boundary is observed at the base of the mega conglomerate and mega breccia intervals associated with the middle Rader interval. This interval overlies the lower Rader interval which is not present at the more distal outcrop localities of the Creek Bed outcrop and Road Cut outcrop, as the high energy mega conglomerate flows observed eroded the lower Rader unit completely in the more distal localities (Figure 52). The lower Rader unit observed in the more proximal Rader Ridge and Reverse Waterfall outcrop localities show an upper erosive contact with the overlying mega breccia deposit. The presence of the lower Rader unit at both the Rader Ridge, and Reverse Waterfall outcrops further supports the interpretation that these outcrops are located on a more distal portion of a upper slope submarine fan, where lower energy deposition of the mega breccia unit was less powerful than the Mega Conglomerate Unit which eroded the entire lower Rader unit at the Road Cut and Creek Bed localities. The final sequence boundary observed is at the conformable contact between the top of the upper Rader interval, made up of the Debrite Two lithologic unit (Table 1), and the Bell Canyon Sandstone Unit Two (Table 1). At this contact the switch from carbonate to siliciclastic deposits marks the transition from highstand deposition to lowstand deposition (Figure 52).

This interpretation is consistent with the basinal cycles and sea level fluctuations interpreted by Lawson (1989) who describes two sequence boundaries at the base of the mega breccia and Mega Conglomerate Units as well as at the contact between the top of the upper Rader interval and the Bell Canyon sandstone above the Rader Formation. She notes that while the two boundaries are extremely different, one being truncational

141

and the other marking a switch from carbonate to siliclastic deposition, both represent a change in composition that is concomitant with lower sea level.

5.5 Depositional Mechanisms

Water depth some 2 miles from the basin margin was interpreted to be at least 1000 ft (King, 1948; Adams, 1936; Meissner, 1972; Lawson, 1989). Geologically, this paleo-water depth estimation makes the Rader deposits examined in this study to be deep water deposits. Deep water deposits are defined as "sediments that have been transported under gravity-flow processes and deposited in the marine environment, beneath storm-wave base, from the slope to the floor of the basin" (Slatt, 2013). These deposits can be classified as intrabasinal, where sediment is sourced from inside the basin, or extrabasinal, where sediment is sourced from outside the basin (Slatt, 2013). The deposits observed in this study are determined to be intrabasinal, as evidence points to the provenance of Rader sediments to be sourced from the reef crest and more distal fore slope environments.

Stark differences between the deposits observed in the lower and upper Rader deposits and the middle Rader deposits, indicate that several different transport mechanisms were responsible for these studied deposits. Different sub aqueous gravity flows are separated and identified based on several different criteria including rheological character and grain support mechanisms of individual flows (Lawson, 1989). Grain support mechanisms include fluid turbulence, hindered settling, dispersive pressure, and matrix strength (Lowe, 1982). Figure 53 summarizes and describes these sediment support mechanisms. In a single flow, multiple grain support mechanisms

142

may be at work. Thus, flow deposits may express characteristics of several grain

support mechanisms, creating muddled nomenclature boundaries (Lawson, 1989).
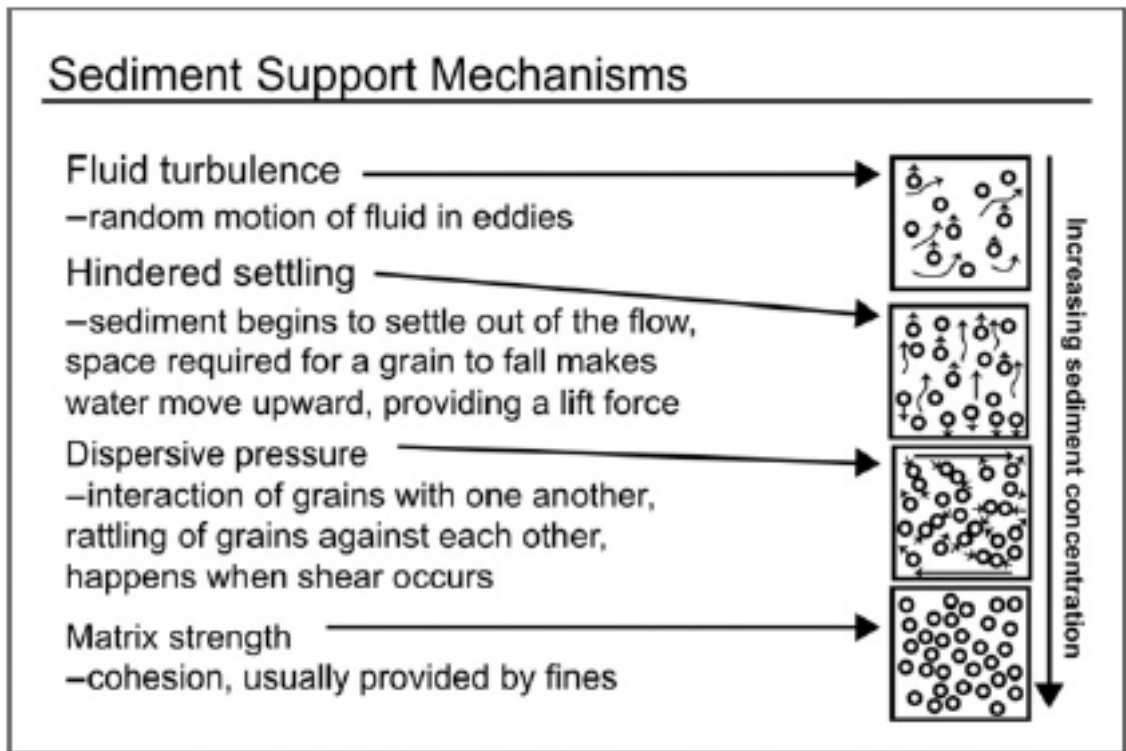
**Figure 53: Sediment support mechanisms acting on sediment gravity flows.
Modified from Lowe (1982). Figure taken from Slatt (2013).**

The ungraded massive limestone deposits observed in this study are classified as

grain flows, turbidites, and debris flows. Almost all flows except for very thin intervals

observed in thin sections are made up of very fine grainstones and packstones. These

are interpreted to have been very dense grain supported flows. In these deposits the

high density of the grains entrained in the flow causes the grains to collide, creating

dispersive stress which prevents settling (Figure 53) (Lowe, 1982). Grains observed in

these deposits are a mixture of skeletal and non-skeletal grains described above in more

detail in the lithofacies and thin section observation sections at each locality.

Graded limestone beds observed throughout the study area in the lower and upper Rader units are interpreted to be high density turbidite deposits. These flows exhibit waning characteristics vertically as the grain size decreases from the base to the top. The high density turbidites exhibit Bouma units A, A-B, B-C, C-E, and D-E. Bouma A-D is not observed in the current study, though Lawson (1989) observed Bouma A-D sequences in basinal deposits that might not have been viewed in the current study.

The mega breccia and mega conglomerates observed at the Rader Ridge/Reverse Waterfall and Road Cut/Creek Bed outcrops respectively exhibit characteristics most compatible with that of debris flows. However, many characteristics observed within these deposits are atypical of debris flows. Debate exists as to how to properly classify the Mega Conglomerate Unit observed at the Road Cut and Creek Bed outcrops and the mega breccia observed at the Rader Ridge and Reverse Waterfall outcrops. In her study on the Rader deposits, Lawson (1989) classified the mega conglomerate as a debris flow, and classified the mega breccia as a density modified grain flow.

The Mega Conglomerate Unit observed at the Road Cut and Creek Bed outcrops has an erosive base, and the boulder sized carbonate clasts are matrix supported. The matrix consists of very fine grained sandstone and contains very small amounts of mud and clay. The unit exhibits very poor sorting and no grading, with boulder sized carbonate clasts rafted throughout the deposit. The boulder sized carbonate intraclasts are rounded to sub rounded. The Mega Conglomerate Unit is topped by the Bull Head Turbidite, though whether the Bull Head Turbidite is related to the mega conglomerate

144

deposit below is debated. Lawson (1989) believes that the mega conglomerate and the Bull Head Turbidite are not related, a view not shared in this report.

The mega breccia observed at the Rader Ridge and Reverse Waterfall outcrops has an erosive base, and the carbonate intraclasts that are up to three ft in their longest exposed dimension are observed to be both matrix and clast supported. The matrix is made up of a very fine grained light tan calcarenite and contains very small amounts of mud and clay. The unit exhibits poor sorting and no grading with the large intraclasts observed throughout the entire unit.

Both the mega breccia and Mega Conglomerate Unit are poorly sorted and poorly graded. The mega conglomerate is matrix supported while only portions of the mega breccia are matrix supported. Both exhibit rafted clasts near the top of the deposit. The mega conglomerate is observed to be able to travel across low angle slopes as it is observed in the basin margin. Conversely, the mega breccia is only observed in the toe of slope, and cannot be described with certainty to be able to travel across low angle slopes. Additionally, both exhibit random clast orientations. All of the above are characteristics of a debris flows. Atypical of a debris flow, however, is the erosive base observed in both the mega conglomerate and mega breccia, as well as non-mud or non-clay dominated matrixes.

Very few of the above listed characteristics comply with the definition of a density-modified grain flow which are: grain supported, inverse grading, coarse matrix (minor mud, imbrication of clasts, zones of turbidite-like features, and poorly sorted fabric). The only characteristic that the mega conglomerate and mega breccia share with the density modified grain flow is a mud poor matrix. Although, the mega breccia

and Mega Conglomerate Units do not match the characteristics of either a debris flow or density modified grain flow perfectly, they share more characteristics with debris flows, indicating that both the mega breccia and mega conglomerate deposits are debris flows.

5.6 Cause of Catastrophic Failure

Many theories exist on the cause of the catastrophic failure which resulted in the deposition of the mega breccia and Mega Conglomerate Units. These include undercutting of the steep shelf by wave action or currents (Jones and Ng, 1997), earthquakes (Lawson, 1989), tsunamis, lowstand incisions of canyons ((Scholle et al., 2015), lowstand dissolution and karstification of shelf deposits (Scholle et al., 2015), and cementation and fracturing of Capitan Shelf-margin carbonates (Scholle et al., 2015).

A tsunami as a cause of the catastrophic deposits observed in the middle Rader interval is rejected as there is no evidence of major fault displacement within the Delaware Basin during the late Permian. Additionally, there is a lack of terrigenous sediment and back reef fossils found in the megabreccia and Mega Conglomerate Units. This would be expected as a tsunami capable of causing such a large scale platform failure would have significant run up height and distance, which would transport significant terrigenous debris well behind the reef crest into the basin (Shiki et al., 2008). While a tsunami is not interpreted to be the cause of the catastrophic deposits of the Rader Formation, evidence of tsunamiites are observed in the study area and will be discussed later in this section.

Undercutting of the slope by wave action (Jones and Ng, 1988) is unlikely as even in periods of lowstand the reef crest was not believed to be subaerialy exposed. It

146

was reported by Garret (2016) that the reef was below wave base, as the constituents of the reef towards the end of the Permian were not strong enough to resist such a high energy environment. Additionally, no karsting is observed in the Capitan Reef, which would be expected from a subaerialy exposed carbonate body.

Earthquakes and seismicity in general is commonly employed as an explanation for catastrophic flows resulting from platform failures. This hypothesis is difficult to discount as even small seismic events can induce large catastrophic slope collapses (Spence and Tucker 1997). Cook et al. 1972, Mutti et al., (1984), and Marjanac (1984) believe that large-scale, platform-margin collapses occur catastrophically by earthquake shocks (Mullins and Garulski, 1986). The effectiveness of seismicity to trigger catastrophic flows in sub aqueous environments is primarily due to their ability to instantaneously increase pore fluid pressure, greatly reducing stability of sediments (Spence and Tucker, 1997).

Based on all observations and research, this study favors the hypothesis that the catastrophic deposits observed in the Rader Formation are the result of a fall in sea level contributing to shelf instability. This interpretation is further supported by Spence and Tucker (1997) who found that both rises and falls of relative sea level can have either a casual or direct link to the initiation of gravitational instability, but overall relative sea-level falls are more favorable to a greater range of potential trigger mechanisms for megabreccia formation. Furthermore, 80% of megabreccias are deposited during relative sea-level falls (Spence and Tucker, 1997). As sea level drops, less water is present to support platform sediments which increases shear stress on underlying slope sediment (Spence and Tucker, 1997). At a critical point, in order for initiation of a

147

catastrophic platform failure, yield strength of the slope is overcome by the shear stress

generated by sediment weight increase caused by fall in sea level (Lawson, 1989).

Yield strength is a function of cohesion and internal friction, and is defined as the

maximum stress which can be supported before platform failure occurs (Bangnold,

1968; Rodine and Johnson, 1976; Hampton, 1979; Lawson, 1989).   Decreasing yield

strength is elevated pore pressure which occurs in response to the increasing weight of

shelfal sediments as sea level drops (Spence and Tucker, 1997). Spence and Tucker

(1997) go on to state that megabreccia deposits may build volumetrically significant

toe-of-slope wedges and aprons during relative lowstands of sea-level, as is interpreted

in the middle Rader unit observed in this study. This catastrophic collapse was likely

aided by pre-existing planes of weakness seen in sub-marine cemented fractures

observed in the Capitan Reef (Figure 54).

Figure 54: Sub-marine cemented fractures observed in the Capitan Reef near Whites City, New Mexico. These fractures likely contributed to the platform failure caused by falling sea level during the deposition of the middle Rader interval as they are evidence of pre-existing plains of weakness. Rock hammer for scale. Photo courtesy of Dr. John D. Pigott.

5.7 Evidence of Tsunamiites

One of the hypothesis for the trigger of the catastrophic megabreccia and mega conglomerate deposits is a tsunami. While this theory is rejected as a cause for the catastrophic deposit, the author does believe that there is evidence of tsunami deposits,

forthwith called tsunamiites which is related to the deposition of the mega breccia and Mega Conglomerate Units.

The cut-and-swale feature observed at the Creek Bed locality in the Bull Head turbidite is interpreted to represent hummocky cross-stratification (Figure 35). Hummocky cross-stratification was originally defined by Harms et al. (1975), and classically is interpreted to represent shore face and shelf environments well above effective storm wave base (Prave and Duke, 1990). These sedimentary structures are thought to represent storm deposits (Harms et al., 1975). Though the origin of hummocky cross-stratification remains controversial, commonly suggested causes include strong oscillatory flows and combined flows involving oscillatory and unidirectional components (Harms et al., 1975; Prave and Duke, 1990). A significant source of controversy arises from the fact that laboratory experiments have not been able to reproduce the structures, and direct observations on the continental shelves do not exist (Morsilli and Pomar, 2012). Recent work has identified hummocky and hummocky like cross-stratification in increasingly deep water environments summarized in Table 2 below. In the most extreme case, hummocky like cross-stratification was identified by Mulder et al. (2008) in estimated water depths of 1000 to 1500m.

Depositional environments			References
continental		marine	
FLUVIAL			Rust and Gibling (1990), Cotter and Graham (1991)
LACUSTRINE			Campbell and Oaks (1973), Eyles and Clark (1986), Pérez et al. (1987)
ESTUARINE			Campbell and Oaks (1973)
INTERTIDAL FLAT			Campbell and Oaks (1973), Yang et al. (2006)
		TURBIDITES	Prave and Duke (1990), Monaco (1992), Mulder et al. (2009)
		PELAGIC	Séguret et al. (2001)
		SPICULITIC CHERT	Gates et al. (2004)
		BLACK SHALES	Schieber (1994)

Table 2: Depositional environments where hummocky cross-stratification or hummocky like cross-stratification has been observed. Increasing depth from the left to the right. Table taken from Morsilli and Pomar (2012).

As mentioned above, hummocky cross-stratification is multi-genetic and does not indicate a specific depositional environment or hydrodynamic conditions (Prave and Duke, 1990). Small scale hummocky cross-stratification and hummocky like cross-stratification are thought to be the result of antidunes formed by the flow of deep water turbidites (Prave and Duke, 1990; Mulder et al., 2008). These small scale hummocky cross-stratification deposits are determined to not be caused by oscillatory flow associated with reflected (sloshing) because there is no evidence of returning flows such as sharp grain size breaks or mud partings (Prave and Duke, 1990). Additionally, Prave and Duke (1990) reject tsunamis as a possible generative mechanism as the periods associated with such flows are too long to be able to create oscillatory bed forms with decimeter-scale spacing observed in small scale hummocky cross-stratification and hummocky like cross-stratification.

The hummocky cross-stratification observed at the Creek Bed outcrop does not fit into the characteristics of small scale hummocky cross stratification observed by Prave and Duke (1990) or the hummocky like cross-stratification observed by Mulder et al., (2008) as the wave lengths are greater than one meter. Fujiwara and Kamataki (2007) describe hummocky cross-stratification deposits associated with Tsunamiites.

151

The hummocky cross stratification observed has wavelengths on the order of meters and not decimeters, and also observe normal grading with hummocky cross stratification packages overlain by mud drapes (Fugiwara and Kamataki, 2007). The internal structure of tsunamiites are distinct, reflecting the extremely long wavelengths and wave period of tsunami events. This is reflected in the long wave lengths observed in the hummocky cross stratification (up to 2 m) and the mud draping observed above each hummocky cross stratification interval seen at the Creek Bed outcrop (Figure 35).

Tsunamiites are classically identified in four main bed forms separated from one another by mud drapes, these bed forms are labeled Tna, Tnb, Tnc, and Tnd (Fujiwara and Kamataki, 2007; Shiki et al., 2008). Figure 55 below describes the idealized tsunamiite with associated wave amplitude responsible for each bed form. Like turbidite deposits, tsunamiites are often incomplete. At the Creek Bed outcrop, the Bull Head Turbidite is interpreted to only represent Tnb deposits. The Tna deposit is interpreted to have been eroded by the Tnb deposit. Additionally, it is possible that the Tna, Tnc, and Tnd deposits are not found at this distal locality because of non-deposition. This could be caused by the lower wave amplitude and strength associated with their deposition in comparison to that responsible for the Tnb deposit (Figure 55). Additionally, in the deep water setting observed for the Rader deposits, typical shallow water tsunamiite deposits (Figure 55) likely do not apply as the repeating up-flow and return flow are expected to be different. Additionally, the very steep shelf slope profile present in the Delaware Basin greatly affected the wave propagation, and could explain the lack of terrigenous detritus observed in the interpreted tsunamiites seen at the Creek Bed outcrop.

152
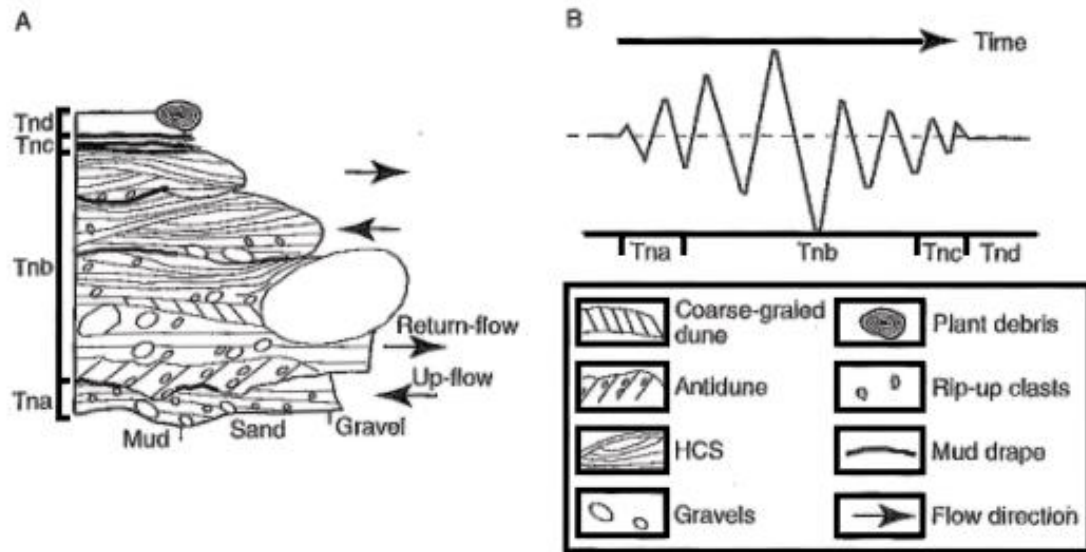
Figure 55: Idealized depositional model and waveform of run-up tsunamis. (A) Schematic succession of sediment sheets in tsunamiites. From bottom to top, depositional units Tna to Tnd correspond to wave forms in (B). (B) Schematic waveform of tsunami wave magnitudes responsible for sediment sheets Tna-Tnd seen in (A). Figure modified from Shiki et al. (2008).

Tsunamiites have been observed and interpreted in extremely deep water depths. Tsunamiites termed homegenites have been observed on the abyssal plain of the Mediterranean Sea in water depths in excess of 2000m (Shiki et al., 2008). Further, it is suggested that the maximum water depths where erosion and reworking of sediment is between 1000 and 3000m (Shiki et al., 2008; Weiss, 2008). The tsunamiites observed at these depths are called homogenites because of the very subtle changes in grain size, and for the most part appear to be homogeneous. They are deposited as a result of fine sediment falling out of a suspension cloud generated by tsunamis (Shiki et al., 2008). These deposits are not the tsunamiites observed in the Rader Formation, and the water depths they are observed in far exceed the water depths in which the Rader Formation was deposited. However, these examples serve the purpose showing that it is possible for tsunamis to influence sediment at the water depths of 300-500m present during the

deposition of the Rader Formation, and it is possible for tsunamiites to be deposited in such water depths.

Tsunamis are generated by various sources including asteroid impacts, earthquakes, volcanism, landslides, and subaqueous slides (Shiki et al., 2008). Shiki et al. (2008) state that subaqueous earthquakes and slides are major triggers, while volcanic activity and asteroid impacts are occasional factors, though more are being discovered. All of the above mentioned possible triggers are potential catalysts for the tsunamiite deposits observed in the Rader Formation, however, the idea of an impact tsunami is not probable as there is no evidence of an asteroid impact in the Permian Basin during the deposition of the Rader Formation. However, it is not possible to disregard this with 100% certainty as the Late Devonian Alamo Impact in southern Nevada is thought to be linked to breccia tsunamiites up to 250 miles away (Morrow et al., 2005), implying that a meteor impact outside of the Permian Basin could cause tsunamiite deposits. A subaerially extensive, landslide generated tsunami is also disregarded because of the lack of terrigenous input observed in the interpreted tsunami deposit, with all sediments observed being sourced from the reef crest or forereef environments. Volcanism and seismic activities are impossible to disregard with 100% certainty. Ash bed deposits within the Rader Formation provide evidence that volcanism was present during the deposition of the Rader Formation (King, 1948; Lawson, 1989), though the proximity of this activity is unknown. Tectonic activity during the deposition of the Rader Formation points to the source of the ash beds being to the south, with volcanism related to the collision of Laurasia and Gandwana plates (personal communication of 2017 with Dr. Pigott). The lack of proximity to the

154

Delaware Basin makes it improbable that volcanism is responsible for the tsunami responsible for the tsunamiite observed in the Rader Formation.

As described above when discussing the cause of the debris flow observed in the Rader, it is impossible to discount an earthquake as a trigger for the debris flow or for a tsunami. Additionally it is possible that a small seismic event could trigger a massive subaqueous slide which could be primarily responsible for the tsunami event. This is possible as even a small earthquake can induce slumping of a subaqueous shelf and liquefaction of the sea bottom, causing a massive movement of sediment (Shiki et al., 2008).

The interpreted cause of the tsunami which resulted in the deposition of the tsunamiite is a large scale subaqueous slide observed in the mega conglomerate and mega breccia deposits. This is deducted through the observed relation between the Bull Head Turbidite, where the hummocky cross-stratification is observed, and the underlying Mega Conglomerate Unit. Examples of subaqueous induced tsunamiites include the 1958 Alaska tsunami, the Storegga Tsunami in north-eastern Scotland which was generated by one of the world's largest submarine slides, the second Storegga slide, which took place on the Norwegian continental slope (Shiki et al., 2008). Also, the Gloria Knolls Slide, the largest subaqueous slope failure near the Great Barrier Reef, was modeled to be able to generate a wave of ~90 ft. Additionally, the enclosed nature of the Delaware basin would make it possible for multiple oscillatory wave events to affect the observed hummocky cross-stratification deposits interpreted as tsunamiites.

Chapter 6: Implications and Future Work

6.1 Implications

Understanding platform failure deposits as seen in the Rader Formation has great value in hydrocarbon exploration and development. Many fields produce from debris flows. Two of the most notable are the Poza Rica Field in Mexico, which is a debris flow believed to be initiated by an asteroid impact (Enos, 1985). Another example is the Mescalaro Escarpe Field in New Mexico, which is a shelf slope carbonate debris deposit of the Bone Spring Formation (Saller, 1989). While the Rader Formation does not contain producible amounts of hydrocarbons, thin section analysis shows organics as well as oil staining present indicating that hydrocarbons where present at some time in the formation.

6.2 Future Work

Further investigations should be done into the hydrocarbons found within the Rader Formation. Investigating this could determine the source of the hydrocarbons. This could tell us whether the hydrocarbons where generated within the Rader deposits or if the hydrocarbons simply migrated through the Rader Deposits.

Additional work into other contemporaneous deposits would also shed considerable insight into the causal mechanism of the Rader debris flow. Understanding how extensive the Rader Formation is, is it a local or basin wide event? Determining the extent of the Rader Formation, as well as the mechanisms responsible for the deposits at alternative locations could aid in determining the trigger mechanism.

Correlating the Rader Formation into the subsurface would also be useful information. The current study only analyzed Rader Deposits seen in outcrop. This

encompassed deposits in the toe of slope to basin margin. Little is known of the Rader Deposits in the Basin. A correlation of the Rader from outcrop to sub surface would could shed light on the process sedimentology of the Rader Formation on the basin floor.

This study shows the presence of tsunamiites within the Delaware Basin. This deposit is thought to have been generated by the massive platform failure responsible for the deposition of the mega conglomerate and mega breccia observed in the middle Rader interval. This possibly indicates that many other tsunamis may have been generated by other platform failures, landslides, or massive subaqueous debris flows in the basin. In this context, new deposits may be observed or re-examined and similarly be discovered to be tsunamiites.

Chapter 7: Conclusions

The Rader Formation is a mixed carbonate and siliciclastic deposit. Its depositional history is marked by shelf instability. From the study of four outcrop locations using classical field methods, thin section analysis, XRF, GR, and LiDAR the following conclusions are drawn:

- Spicules, radiolarians, forams, bryozoans, corals, trilobites, echinoderm spines, fusulinids, and length slow chalcedony show deep to increasingly shallow allochem supply. Lack of ooids, pisolites, and fenestral fabrics indicate that the restricted marine back reef environments are not affected by platform failure. Coated grains observed in the mega breccia deposit indicate that the reef crest is the most proximal environment involved in the platform failure responsible for the debris flows found in the middle Rader interval.

- Water depth during Rader deposition was between 900 and 1500 ft throughout deposition of the Rader Formation.

- Differences in lithological makeup and lack of correlation observed in both geochemical proxy profiles and total gamma ray profiles indicate deposition of Rader sediment in different facies of an upper slope fan deposit. The proximal toe of slope Rader deposits were deposited in the channel margin of an upper slope fan deposit while the more distal medial slope margin Rader deposits were deposited in the channel axis of an upper slope fan deposit

- Grain flows and high density turbidite flows are the dominant mechanisms responsible for transporting skeletal and non-skeletal sediments deposits observed in the lower and upper Rader units. The mega breccia and mega

conglomerate deposits observed in the middle Rader unit were deposited by debris flows.

- While it is impossible to determine the cause of the catastrophic platform failure with 100% certainty, sea level fall and resulting sediment loading resulted in the platform collapse. The consequence of which is the mega breccia and mega conglomerate deposits. Several additional contributing factors such as seismic activity and pre-existing planes of weakness observed as submarine cement filled fractures in the Capitan Reef likely contributed to platform failure, but sea level fall and resulting increased pressure on the slope is interpreted to be the main contributing factor.

- Hummocky cross-stratification observed in the Bull Head Turbidite at the Creek Bed outcrop is interpreted to be a tsunamiite. Similar to the cause of the catastrophic platform failure, it is impossible to determine the cause of the tsunami with 100% certainty. However, because the hummocky cross-stratification directly overlies the mega conglomerate, it is interpreted that the tsunami is directly related to the debris flows that resulted from the platform failure. From this the most likely cause of the tsunami responsible for the tsunamiite is the large subaqueous debris flow which is a consequence of the catastrophic platform failure.

References

Adams, J.E., 1965, Stratigraphic-Tectonic Development of Delaware Basin: AAPG Bulletin, v. 49.11, p. 2140-2148.

Algeo, T.J., and H. Rowe, 2012, Paleoceangraphic applications of trace-metal concentration data: Chemical Geology, V. 324-325, p. 6-18.

Bagnold, R.A., 1968, Deposition in the process of hydraulic transport: Sedimentology, v. 10, p. 45-56.

Blakey, R.t., 2013, Paleogeography and Geologic Evolution of North America, Colorado Plaateau Geosystems, Inc. http://cpgeosystems.com/gloaltext2.html, accessed November 2016.

Brumsack, H.J., 2006, The trace metal content of recent organic carbon-rich sediments: Implications for Cretaceous black shale formation: Paleogeography, Paleoclimatology, Paleoecology, v. 232, p. 344-361.

Campbell, C.V. and Oaks Jr, R.Q., 1973. Estuarine sandstone filling tidal scours, Lower Cretaceous Fall River Formation, Wyoming. J. Sediment. Petrol., 43, 765– 778.

Crosby, C.B., 2015, Depositional History and High Resolution Sequence Stratigraphy of the Leonardian Bone Spring Formation, Northern Delaware Basin, Eddy and Lea Counties, New Mexico: Master's thesis, University of Oklahoma, p. 1-230.

Coleman, P.J. 1968, Tsunamis As Geological Agents: J. Geol. Soc., p. 267-273.

Cook, H.E., McDaniel, P.N, Mountjoy, E.W., and Pray, L.C., 1972, Allochthonous carbonate debris flows at Devonian bank ('reef') margins, Alberta, Canada; Bulletin of Canadian Petroleum Geology, v. 20, p. 439-497.

Cotter, E. and Graham, J.R., 1991. Coastal plain sedimentation in the late Devonian of southern Ireland; hummocky crossstratification in fluvial deposits? Sed. Geol., 72, 201–224.

Eyles, N. and Clark, B.M., 1986. Signifi- cance of hummocky and swaley crossstratification in late Pleistocene lacustrine sediments of the Ontario Basin, Canada. Geology, 14, 679–682.

Folk, R.L., and Pittman, S.J, 1971, Length-slow Chalcedony: A New Testament for Vanished Evaporites: Journal of Sedimentary Petrology, V. 41, p. 1045-1058.

Galley, J.E., 1958, Oil and Geology in the Permian Basin of Texas and New Mexico: North America: AAPG Special Volumes, p. 395-446.

Garrett, K.N., 2016, High Resolution Basin Modeling of the Permian Capitan Reef, New Mexico: New Insight from Integrated Outcrop LiDAR-XRF-SGR Analysis into Reef Architecture: Master's Thesis, University of Oklahoma, p. 1-79.

Gates, L.M., James, N.P. and Beauchamp, B., 2004. A glass ramp: shallow-water Permian spiculitic chert sedimentation, Sverdrup Basin, Arctic Canada. Sed. Geol., 168, 125–147.

Geisen, J.H., and P.A. Scholle, 1990, Regional Basinal sandstone depositional patterns during the Guadalupian (Late Permian), Delaware Basin, west Texas-New Mexico [abs]: AAPG Bulletin, v. 48, p. 221-225.

Giddens, E.L., 2016, Pleistocene Coral Reef Destruction in the Florida Keys: Paleotempestite Evidence from High Resolution LIDAR XRF Analysis of Windley Key Quarry, FL: Master's Thesis, University of Oklahoma, p. 1-189.

Hampton, M.A., 1975, The role of subaqueous debris flow in generating turbidity currents: Journal of Sedimentary Petrology, v. 42, no. 4, p. 775-793.

Haq, B.U., and S.R. Schutter, 2008, A Chronology of Paleozoic Sea-Level Changes: Science, v. 322, p. 64-68.

Harms, J.C., Southard, J.B., Spearing, D.R. and Walker, R.G. (1975) Depositional environments as interpreted from primary sedimentary structures and stratification sequences. SEPM, Short Course, v. 2, Dallas, 161 pp.

Harms, J.C. and Williamson, C.R., 1988, Deep-Water Density Current Deposits of Delaware Mountain Group (Permian), Delaware Basin, Texas and New Mexico: AAPG, v. 72, no. 3, p. 299-317.

Hill, C. A., 1996 Geology of the Delaware Basin, Guadalupe, Apache, and Glass Mountains, New Mexico and West Texas: SEPM Publication, no. 96-39.

Hill, C.A., 2000, Overview of the geologic history of Cave Development in the Guadalupe Mountains, New Mexico: Journal of Cave and Karst Studies, 62(2): 60-71.

Hills, J.m., 1984, Seimentation, Tectonism, and Hydrocarbon Generation in Delaware Basin, West Texas and Southeastern New Mexico: AAPG Bulletin, v. 68.3, p. 250-267.

Jones, B., and Ng, K.C., 1988, Anatomy and diagenesis of a Pleistocene carbonate breccia formed by the collapse of a seacliff, Cyman Brac, British West Indies: Canadian Petroleum Geology Bull., v. 36, p. 9-24.

King, P.B. Permian of West Texas and Southeastern New Mexico. Tulsa, OK: American Association of Petroleum Geologists, 1942. Print.

King, P.B., Geology of the Southern Guadalupe Mountains, Texas: Washington U.S. Govt. Off. 1948.

Koss, G.M., Carbonate Mass Flow – Turbidite Sequences of the Permian Delaware Basin, West Texas: Master's thesis, University of Wisconsin, Madison Wisconsin, 80 p.

Lawson, E.C., 1989, Subaquieous Gravity Flows and Associated Deposits in the Rader Member, Capitan Reef Complex (Permian), Delaware Mountains, West Texas: Master's thesis, University of Wisconsin, Madison Wisconsin, 120 p.

Lew C.L., Bragaryddub, S.B., and Pigott, J.D., 2013, Deeowater Basin Model for the Permian Basin: Delaware Basin Example, The International Petroleum Technology Conference in Beijing, China.

Lowe, D.R., 1982. Sediment Gravity Flows II: Depositional models with special reference to the deposits of high-density turbidity currents: Journal of Sedimentary Petrology v. 52, p. 279-297.

Madhavaraju, J. and Y.I. Lee, 2009, Geochemistry of the Dalmiapuram Formation of the Uttatur Group (Early Cretaceous), Cauvery basin, southeastern India: Implications on provenance and paleo-redox conditions: Revista Mexicana de Ciencias Geologicas, v. 26.2, p. 380-394.

Marjanac, T., 1985, Composition and origin of the megabed containing huge clasts: Flysch Formation, middle Dalmatia, Yugoslavia: International Association of Sedimentologists European Regional Meeting, 6th, Lleida, Spain, Abstracts, p. 270-273.

Meissner, F.F., 1972. Cyclic Sedimentation in Middle Permian Strata of the Permian Basin, West Texas and New Mexico: West Texas Geological Cociety Publication 72-60, p.203-232.

Monaco, P., 1992. Hummocky cross-stratified deposits and turbidites in some sequences of the Umbria-Marche area (central Italy) during the Toarcian. Sed. Geol., 77, 123–142.

Morrowm, J.R., Sandberg, C.A, and Harris, A.G., 2005, Late Devonian Alamo Impact, southern Nevada, USA: Evidence of size, marine site, and widespread effects: GSA Special Papers, v. 384, p. 259-280.

Morsilli, M., and Pomar, L., 2012, Internal waves vs. surface storm waves: a review on the origin of hummocky cross-stratification: Terra Nova, v. 00, no. 00, p. 1-10.

Mulder, T., P. Raxin, and J.C. Faugeres, 2009, Hummocky Cross-Stratification-Like Structures in Deep-Sea Turbidites: Upper Cretaceous Basque Basins (Western Pyrenees, France): Sedimentology, v. 56, p. 997-1015.

Mullins, H.T., Gardulski, A.E, Wise, S.W., Applegate, J., 1987. Middle Miocene oceanographic events in the Eastern Gulf of Mexico: implications for the seismic stratigraphic succession and Loop Current/Gulf Stream circulation. Geol. Soc. Am. Bull. 98, 702-713.

Multti, E., Ricci-Lucchi, G., Seguret, M., and Zanzucchi, G., 1984, Seismo-turbidites: A new group of resedimented deposits: Marine Geology, v. 55, p. 103-116.

Nance, H.S. and H.D. Rowe, 2015, Eustatic controls on stratigraphy, chemostratigraphy, and water mass evolution reserved in a Lower Permian mudrock succession, Delaware Basin, west Texas, USA: Interpretation p.11-25.

Nestell, M.K., Nestell, G.P., Wardlaw, B.R. & Sweatt, M.J., 2006, Integrated biostratigraphy of foraminifers, radiolarians and conodonts in shallow and deep water Middle Permian (Capitanian) deposits of the 'Rader slide', Guadalupe Mountains, West Texas: Stratigraphy, v. 3, p. 161-194.

Newell, N.D, J. K. Rigby, A. G. Fischer, A. J. Whiteman, J. E. Hickox, and J. S. Bradley. The Permian Reef Complex of the Guadalupe Mountains Region, Texas and New Mexico; a Study in Paleoecology. San Francisco: W.H. Freeman, 1953. Print.

Nicklen, B.L,. 2011, Establishing a Tephrochronologic Framework for the Middle Permian (Guadalupian) Type Area and Adjacent Portions of the Delaware Basin and Northwestern Shelf, West Texas and Southeastern New Mexico, USA: PhD Dissertation, University of Cincinnati, 119 p.

Fujiwara, O., and Kamataki, T., 2007, Identification of tsunami deposits considering the tsunami waveform: An example of subaqueous tsunami deposits in Holocene shallow bay on southern Boso Peninsula, Central Japan: Sedimentary Geology, v. 200, p. 295-313.

Oslegerm D.A., 1998, Sequence Architecture and Sea-Level Dynamics of Upper Permian Shelfal Facies, Guadalupe Mountains, Southern New Mexico: Journal of Sedimentary Research, no. 2, p. 327-346.

Osleger, D.A., and Tinker, S.W., 1999, Three-Dimensional Architecture of Upper Pemian High-Frequency Sequences, Yates-Capitan Shelf Margin, Permian Basin, U.S.A.: Societty for Sedimentary Geology Special Publication no. 63, p. 169-185.

Payne, M.W., 1976, Basinal Sandstone Facies, Delaware Basin, West Texas and Southeast New Mexico: AAPG Bulletin. Vol. 60, no. 4, p. 517-527.

Prave, A.R. and W.L Duke, 1990, Small-Scale Hummocky Cross-Stratification in Turbidites: a Form of Antidune Stratification?: Sedimentology, v. 37, p. 531-539.

Pe´rez, A., Villena, J. and Pardo, G., 1987. Presencia de estratificacio´n cruzada Hummocky en depo´sitos lacustres del Terciario de la Depresio´n del Ebro. Acta Geol. Hisp., 21–22, 27–33.

Pigott, John D., February 2017, Personal Communication.

Pigott, Kulwadee L., Pigott, John D., Engel, Michael H. Engel, and Philp, Richard P., 2007, High resolution chemical stratigraphy in carbonates: Oxfordian Smackover USA ramp proxy, in AAPG International Conference and Exhibition, November 18-21, 2007, Athens, Greece.

Parra-Galvis, Victor, John D. Pigott, and Kulwadee L. Pigott, 2009, Carbonate Turbidite Platform to Basin Floor Facies Tract of the Jamaican White Limestone, AAPG Denver 2009.

RIEGL Laser Instrument Systems, 2012, RIEGL Glossary.

RIEGL Laser Instrument Systems, 2013, RIEGL VZ-400 Technical Documentation and Users Instructions.

Rigby, J. K., 1958, Mass movements in Permian rocks of Trans-Pecos Texas: Journal of Sedimentary Petrology. vol. 28, no. 3, p. 298–315.

Rust, B.R. and Gibling, D.A., 1990. Threedimensional antidunes as HCS mimics in a fluvial sandstone: the Pennsylvanian South Bar Formation near Sydney, Nova Scotia. J. Sediment. Petrol., 60, 540–548.

Rodine, J.D. and Johnson, A.M., 1976, The ability of debris, heavily freighted with coarse clastic materials, to flow on gentle slopes: Sedimentology, v. 23, p. 213-234.

Sageman, B.B. and T.W. Lyons, 2004, Geochemistry of Fine-Grained Sediments and Sedimentary Rocks: Treatise on Geochemistry, v. 7, p. 115-158.

Sarg, J.F., 1988, Carbonate Sequence Stratigraphy: SEPM Special Publications, no. 42, p. 155-181.

Schieber, J., 1994. Evidence for episodic high energy events and shallow water
     deposition in the Chattanooga Shale, Devonian, central Tennessee, U.S.A. Sed.
     Geol., 93, 193–208.

Scholle, P.A., January 2017, Personal Communication.

Scholle, P.A., Ulmer-Scholle, D.S., Nestell, M.K., and Nestell, G.P., 2015,
     Guadalupian   age basinal facies in the western Delaware Mountain Group
     outcrop belt,   Guadalupe and Apache mountians: in Trentham, R.C. (ed.), West
     Texas   Geological Society Annual Fall Field Trip, October 9-11, 44 p.

Se´guret, M., Pouchkine, A.M., Gabaglia, G.R. and Bouchette, F., 2001. Storm deposits
     and storm-generated coarse carbonate breccias on a pelagic outer shelf (South-
     East Basin, France). Sedimentology, 48, 231–254.

Shiki, T., Y. Tsuji, T. Yamazaki, and K. Minoura. Tsunamiites. Amsterdam: Elsevier,
     2009. Print.

Silver, B.A. and R.G. Todd, 1969, Permian Cyclic Strata, Northern Midland and
     Delaware Basins, West Texas and Southeastern New Mexico: AAPG Bulletin,
     v. 53.11, p. 2223-2251.

Sinclair, T.D., 2007, The Generation and Continued Existence of Overpressure in the
     Delaware Basin, Texas: PhD Dissertation, University of Durham, p. 1-302.

Slatt, R. M. Stratigraphic Reservoir Characterixation for Petroleum Geologists,
     Geophysicists, and Engineers. 2nd ed. Vol. 61. Oxford: Elsevier, 2013. Print.

Smith, C.N., and A. Malicse, 2010, Rapid Handheld X-ray fluorescence (HHXRF)
     Analysis of Gas Shales: AAPG Search and Discovery Article #90108.

Spence, G.H. and M.E., Tucker, 1997, Genisis of Limestone Megabreccias and Their
     Significance in Carbonate Sequence Stratigraphic Models: A Review:
     Sedimentary Geology, v. 112, p. 163-193.

Thermo FIsher Scientific, 2010, User's Guide Version 7.1.

Tinker, S.W., 1998, Shelf-to-Basin Facies Distributions and Sequence Stratigraphy of a
     Steep-Rimmed Carbonate Margin: Capitan Depositional System, McKittrick
     Canyon, New Mexico and Texas: Journal of Sedimentary Research, v. 68, no.
     6, p. 1146-1174.

Treanton, J. A., 2014, Outcrop-derived Chemostratigraphy of the Woodford Shale,
     Murray County, Oklahoma: Master's thesis, University of Oklahoma, Norman,
     Oklahoma, 83 p.

Tribovillard, N., T.J. Algeo, F. Baudin, A. Riboulleau, 2006, Analysis of marine environmental conditions based on molybdenum-uranium covariation- Applications to Mesozoic Plaeoceanography: Chemical Geology, v. 324-325, p. 46-58.

Tribovillard, N., T. Lyons, A. Riboulleau, 2006, Trace metals as paleoredox and paleoproductivity proxies: An Update: Chemical Geology, v. 232, p. 12-32.

Weiss, R., 2008, Sediment Grains Moved by Passing Tsunami Waves: Tsunami Deposits in Deep Water: Marine Geology, v. 250, p. 251-257.

Turner B.W., J.A. Treanton, and R.M. Slatt, 2016, The use of chemostratigraphy to refine ambiguous sequence stratigraphic correlations in marine mudrocks. An example from the woodford shale, Oklahoma, USA: Journal of the Geological Society, online publication.

Yalcin, E., 2014, Delaware Basin Thermal Evolution from Constrained Vitrinite Reflectance: Tectonic Versus Flexural Subsidence: Master's Thesis, University of Oklahoma, Norman Oklahoma, 174 p.

Yang, B., Dalrymple, R.W. and Chun, S., 2006. The significance of hummocky cross-stratification (HCS) wavelengths; evidence from an open-coast tidal flat, South Korea. J. Sediment. Res., 76, 2–8.

Yang, K.M. and S.L. Dorobek, 1995, The Permian Basin of West Texas and New Mexico: Tectonic History of a "Composite" Foreland Basin and its Effects on Stratigraphic Development: SEPM Special Publication, v. 52, p. 149-174.